Study of the structure, particle morphology and optical properties of mixed metal oxides.

By

PULANE MOKOENA
(B.Sc Hons)

A dissertation presented in fulfilment of the requirements for the degree

MAGISTER SCIENTIAE

Department of Physics

Faculty of Natural and Agricultural Science

University of the Free State

RSA

Supervisor: Prof OM Ntwaeaborwa

Co-Supervisor: Prof RE Kroon

UNIVERSITY OF THE FREE STATE
UNIVERSITEIT VAN DIE VRYSTAAT
YUNIVESITHI YA FREISTATA

UFS UV

January 2017

Dedication

This Thesis is dedicated to the loving memory of my late mother Thenjiswa Evelyn Mokoena and brother Tshepo Alexius Motaung.

Acknowledgements

- I would firstly like to thank God for His love, favour, goodness, grace, will and purpose for my life. His purpose propelled me forward in the midst of incredibly difficult and trying times.
- I would also like to express my sincere gratitude to my supervisor *Prof. O.M. Ntwaeaborwa,* for always encouraging, supporting and guiding me throughout the study. The study could not have been a success without him. Thank you a lot.
- My co-supervisor Prof RE Kroon, thank you for your valuable input, helpful suggestions and support.
- To all the staff members of the Department of Physics UFS, technical staff and post-doctoral fellows thank you for your continual assistance, encouragement and support.
- To all staff members of the Department of Physics UFS (Qwa Qwa Campus) Dr KG Tshabalala, Mr SJ Motloung, Dr LF Koao and Miss Meiki Lebeko thank you for the encouragement, support and prayers throughout the study.
- To my fellow researchers thank you Miss Busisiwe Mabuea, Dr Ella Linganiso, Mr Simon Ogugua, Mr Emad Hasabeldaim, Miss Puseletso Mokoena, Dr Masechaba Tshabalala, Miss Mantwa Lephoto, Mr Mpho Mokoena, Mr Sefako Mofokeng and Mr Teboho Mokoena for your assistance and support.
- The South African National Research Foundation (NRF) and the University of the Free State are acknowledged for their financial support.
- To all my friends Itumeleng, Dora, Sibusiso, Nozuko, Tholakele, Nomvo, Motheo, Modiehi, Maphuti, Moipone and Bafokeng thank you for love, support and prayers everyday regarding my life and dreams. I love and appreciate you so much.
- I would like to thank my father, sister, nieces, nephew and extended family for their financial and emotional support, love, encouragement and prayers even through the difficult times you continued to be my pillars of strength and anchors always keeping me sane, humble and whole.
- To the love of my life, best friend and fiancé Thokozane Moses Sithole words cannot describe how thankful I am for all the love, support, encouragement and assistance you've not only shown me regarding my dreams, academics and goals but also my life in totality.

Abstract

The structure, morphology and optical properties of metal oxides (ZnO, MgO and SrO), their composites (MgO-ZnO, SrO-ZnO) and systems with different x molar concentration values (0.2, 0.4, 0.5, 0.6, 0.7, 0.8) of $Mg_xZn_{1-x}O$ and $Sr_xZn_{1-x}O$, were synthesized via solution combustion method at initial reaction temperature of 600 ˚C for 15 minutes. These properties of the synthesized nanostructures were investigated using X-ray diffraction (XRD), Scanning Electron Microscopy (SEM), High resolution transmission electron microscope (HR-TEM) and Photoluminescence (PL) spectroscopy.

The ZnO, MgO and SrO phosphors were successfully synthesized via solution combustion method and their crystallization was confirmed by XRD analysis. The ZnO powder crystallized in the hexagonal phase. The diffraction patterns of the ZnO samples became sharper and more intense when synthesis temperature was increased from 600 ˚C to 700 ˚C indicating improvement of crystallinity and an increase in crystallite sizes from 23.3 nm to 30.06 nm of the as-prepared undoped ZnO phosphor powder. The MgO powder had cubic crystal structure with Fm-3m space group and crystallized in rocksalt/sodium chloride (NaCl) type cubic structure and the SrO sample indicated the presence of three well-defined crystalline phases which are SrO, $Sr(OH)_2$ and $Sr(CO_3)_2$, with $Sr(OH)_2$ appearing as the most prominent phase.

With respect to the following systems: $Mg_xZn_{1-x}O$ and $Sr_xZn_{1-,x}O$ and their composites, their XRD patterns revealed the presence of two well-defined crystalline phases, namely MgO or SrO and ZnO, the most prominent phase being ZnO.

The SEM images of ZnO showed agglomeration of small particles and flower-like morphology. The HR-TEM images showed that the nanoparticles (NPs) were hexagonally shaped and aggregated into clusters. The SEM images of MgO showed spherical cube-like morphology with the appearance of closely-packed or attached particles in all the SEM micrographs. The HR-TEM images show that the NPs were cubic-spherically shaped and aggregated into clusters.

For the SrO sample small and coagulated particles of irregular shapes and different sizes were observed. Pores of different sizes were also observed from the solution combustion synthesis. This is due to the outgassing of the gaseous products, namely N_2 and CO_2, of this synthesis method. The HR-TEM images showed that the NPs were spherically shaped and aggregated into clusters. The selected area electron diffraction pattern confirmed the observation of a large number of nanoparticles and hence there were many spots within each ring.

In the case of the $Mg_xZn_{1-x}O$ system SEM observations revealed different kinds of particle morphologies such as pyramids clustered together to form flowers with spherical particles grouped together on the sides, triangles grouped together in the shape of a cauliflower, tetragonally shaped particles with some degree of faceting and for the $Sr_xZn_{1-x}O$ system, flower-like structures, oval-shaped particles and elongated rod-like structures.

The photoluminescence results of ZnO exhibits two characteristic peaks: one narrow in the ultraviolet (UV) region at 380 nm which comes from recombination of free excitons, and one broad in the visible region at 639 nm for ZnO synthesized at 600 ˚C and 626 nm for ZnO synthesized at 700 ˚C, which were attributed to electron mediated defect levels in the bandgap.

The MgO sample showed three PL emission peaks at approximately 419, 432 and 465 nm and a minute emission peak at 663 nm. The SrO PL spectrum exhibited UV and deep level emission peaks. In addition, there was a narrow peak in the UV region at 397 nm and a broad peak in the visible region at 750 nm.

With regards to the $Mg_xZn_{1-x}O$ system with x ranging from 0.2, 0.4, 0.5, 0.6 and 0.7, a red shift in the emission peaks from 602 to 610 nm was observed for the 0.2 and 0.4 molar concentrations while their luminescence intensity decreased. For a molar concentration 0.5 there was a blue shift in the emission peak from 610 to 551 nm together with luminescence quenching. From molar concentration 0.5 to 0.6 there was a blue shift in the emission peaks from 551 to 539 nm with a luminescence enhancement, but when the molar concentration was 0.7 there was a slight red shift in the emission peak located from 539 to 549 nm together with a luminescence enhancement. With regards to the MgO-ZnO composite sample there was only one broad emission peak at 559 nm in the visible region and luminescence intensity increased significantly.

For molar concentrations 0.2 and 0.4 there were emission peaks at 383, 540 and 760 nm. For molar concentration 0.5 there were emission peaks at 383, 514 and 760 nm. For molar concentration 0.6 there were emission peaks at 383 nm, minor humps at 413, 435 and 760 nm and a broad peak at 514 nm. For molar concentration 0.7 there were emission peaks at 383, 514 and 760 nm and for molar concentration 0.8 there were emission peaks at 383, 514 and 760 nm. The emission peak in the UV region (383 nm) was narrow and this was ascribed to recombination of free excitons, while the broad emission peaks at 514 and 540 nm were attributed to electron mediated defect levels in the bandgap.

Keywords: Metal oxides, solution combustion method, structure, morphology, luminescence.

Declaration

I (Pulane Mokoena) declare that the thesis hereby submitted by me for the Master's degree at the University of the Free State is my own independent work and has not previously been submitted by me at another university/faculty. I furthermore, cede copyright of the thesis in favour of the University of the Free State.

Signature:…….. Date:……

Acronyms

XRD—X-ray Diffraction

XPS- X-ray Photoelectron Spectroscopy

HR-TEM - High Resolution Transmission Electron Microscopy

SAED- Selected Area Electron Diffraction

SEM—Scanning Electron Microscopy

EDS—Energy Dispersive X-ray Spectroscopy

FTIR— Fourier Transform-Infrared Spectroscopy

PL—Photoluminescence

UV-Vis—Ultra Violet-Visible

eV— Electron Volts

JCPDS—Joint Committee on Powder Diffraction Standards

Table of contents

List of Figures

Chapter 1: Introduction

1.1. Overview

The quality of human life, economic and global stability largely depend on a readily and reliable supply of energy. The global current rate of energy consumption is approximately 4.1×10^{20} J/yr, which is equivalent to 13 trillion watts. The World Bank predicts that the demand for energy will double (to 30 trillion watts) by 2050 with an increase of the world population to 9 billion people accompanied by a rapid technological development and economic growth [1]. Provision of sustainable energy is essential for the global economic development and human well-being. More than 80% of our current energy production comes from carbon-based fossil fuels such as coal, oil, and natural gas [2]. Energy utilized mainly in the form of electricity and liquid fuels, which they used for domestic, commercial, industrial, and transportation sectors. Although these carbon-based fuels can supply energy for another century or maybe several hundred years [3], continuous reliance on them will cause severe problems to our economy and environment. Economic problems they predicted to arise from a steady increase of oil prices because of continuous demand but restricted supply. Environmental problems, such as global warming, they mainly caused by increase in man-made (anthropogenic) carbon dioxide in the atmosphere originating from burning of fossil fuels. The utilization of the green energy and hence solar energy has become the on-going topics and solution for both governments and scientific communities. The most cost-effective and the improvement of both power conversion efficiency and stability of fabricating solar cells is the solution to this current energy crisis predicament [3]. The substantial investments from both the scientific community and human race to this research field will certainly boost the usage, purchasing and manufacturing of energy materials as an alternative form of renewable energy [4].

1.2. Statement of the problem

The entire world is currently experiencing an energy crisis. The predicament is that the current energy production methods are not meeting the demands of our current life-styles, growing economies and technological advancements of our generation. Among the forms of green energies (e.g. hydropower, wind power, geothermal power and biomass) solar power is one of

the most sustainable energy due to its abundance and renewability. Using the photovoltaic (PV) effect, sunlight can be converted directly into electricity [4]. Currently the solar cell sector is dominated by silicon-based solar cell however the classical efficiency limit of silicon-based solar cells is currently estimated to be 29%, and detailed-balance calculations show that this number could be improved up to approximately 37% using spectral modification [4]. There are three spectral modification methods in place to be used namely downconversion (DC), photoluminescence (PL) and upconversion (UC). It is known that light with energy lower than the threshold of ~ 1.25 eV would be suited for UC, whereas light with energy higher than the threshold of ~ 1.25 eV would be better suited for DC applications for an ideal semiconductor with a threshold of ~ 1.35 eV. South Africa is known as a key international source and producer in the consumer and industry arenas of metals, alloys, and semiconductor products and one of the leading countries in nanotechnology [4].

1.3 Research Aim

To investigate the structural, morphological and optical properties of the solution combustion synthesized materials ZnO, MgO, SrO, Mg doped ZnO, MgO-ZnO composites, Sr doped ZnO and SrO-ZnO composites for photocatalytic studies with respect to solar cell applications.

1.4 Research objectives

- To investigate the luminescent properties of ZnO phosphor powder prepared by solution combustion method.
- To investigate the structural, morphological and optical properties of MgO synthesized by solution combustion method.
- To investigate the structural, morphological and optical properties of mixed phase SrO synthesized by solution combustion method.
- To investigate the impact of synthesis temperature on different structures, composites, morphologies and optical properties of Mg-doped ZnO.
- To investigate the impact of different molar concentrations of Sr doped ZnO samples on the structure, morphology and luminescent properties.

1.5 Thesis Layout

Chapter 2: Presents the literature review on a brief background of phosphors, luminescence and its processes, the application of the phosphors that were fabricated in this study and the mechanism of the semiconductors in photocatalysis.

Chapter 3: Presents a summary of the synthesis and experimental techniques that were used in this study.

Chapter 4: This chapter presents the luminescent properties of ZnO phosphor powder prepared by solution combustion method

Chapter 5: This chapter reports on the structural, morphological and optical studies of MgO synthesized by solution combustion method.

Chapter 6: This chapter reports on the solution combustion study of mixed phase SrO phosphor.

Chapter 7: This chapter reports on the impact of synthesis temperature on different structures, composites, morphologies and optical properties of Mg-doped ZnO samples.

Chapter 8: This chapter reports on the impact of different molar concentrations of Sr doped ZnO samples on the structure, morphology and luminescent properties.

Chapter 9: A summary of the thesis, concluding remarks and suggestion for possible future studies are presented.

References:

[1] Bent R.D., Orr L., Baker R., Energy: science, policy, and the pursuit of sustainability. Island Press: Washington, DC, 2002; p xviii, 257.

[2] van de Krol R.,Y.Q., Schoonman J, Solar hydrogen production with nanostructured metal oxides, J Mater Chem, 18 (2008) 2311-2320.

[3] Lewis N.S., Nocera D.G., Powering the planet: Chemical challenges in solar energy utilization, P Natl Acad Sci USA, 103 (2006) 15729-15735.

[4] Sharma G, Chawla P., Lochab S.P., Singh N., Chalcogenide Lett, 6 (2009), 705–712.

Chapter 2:
Literature Review

Introduction

This chapter presents a brief background of phosphors, luminescence and its processes, the application of the phosphors that were fabricated in this study and the mechanism of the semiconductors in photocatalysis.

2.1. Background of phosphor

A material can emit light either through incandescence, where all atoms radiate, or by luminescence, where only a small fraction of atoms, called emission centres or luminescence centres, emit light [1]. In inorganic phosphors, these inhomogeneities in the crystal structure are created usually by addition of a trace amount of dopants that are intentional impurities also called activators. The wavelength emitted by the emission centre is dependent on the atom itself, and on the surrounding crystal structure. An activator is an impurity ion which is added intentionally into the host material to give rise to a centre that can be excited to luminesce [1]. The impurity concentrations in general are relatively low because of the fact that at higher concentrations the efficiency of the luminescence process usually decreases due to concentration quenching effects. Most phosphors have a white body colour, which is an essential feature that prevents absorption of visible light by the phosphors [1]. Light emission from a phosphor is referred to as either fluorescence or phosphorescence. Light emission during the time when a substance is exposed to the exciting radiation is called fluorescence, while the after-glow if detectable by the human eye after the cessation of excitation is referred to as phosphorescence. However, in organic molecules, the two terms are distinguished by whether the transition to emit light is allowed or forbidden by spin selection rules. Light emission due to an allowed transition is called fluorescence, while that due to a forbidden transition is called phosphorescence [2].

Photoluminescence can be defined as the emission of light which is caused by the irradiation of a substance with other light. The term embraces both fluorescence and phosphorescence, which differ in the time after irradiating over with the luminescence occurs [3]. Fluorescence is a kind of luminescence, excited by irradiation of a substance with light. The light hitting a sample puts atoms, ions or molecules in the sample into excited states, from where they decay into lower-lying states which is their ground states, through spontaneous emission of fluorescence photons [4]. Phosphorescence is a kind of photoluminescence which lasts relatively long after excitation of the medium. The excitation energy is stored in metastable electronic states (often triplet states), exhibiting only forbidden transitions to lower states. The stored energy can be released only through relatively slow processes, which are often thermally activated [4]. Figure 2.1 illustrates the ground, singlet and triplet states transitions.

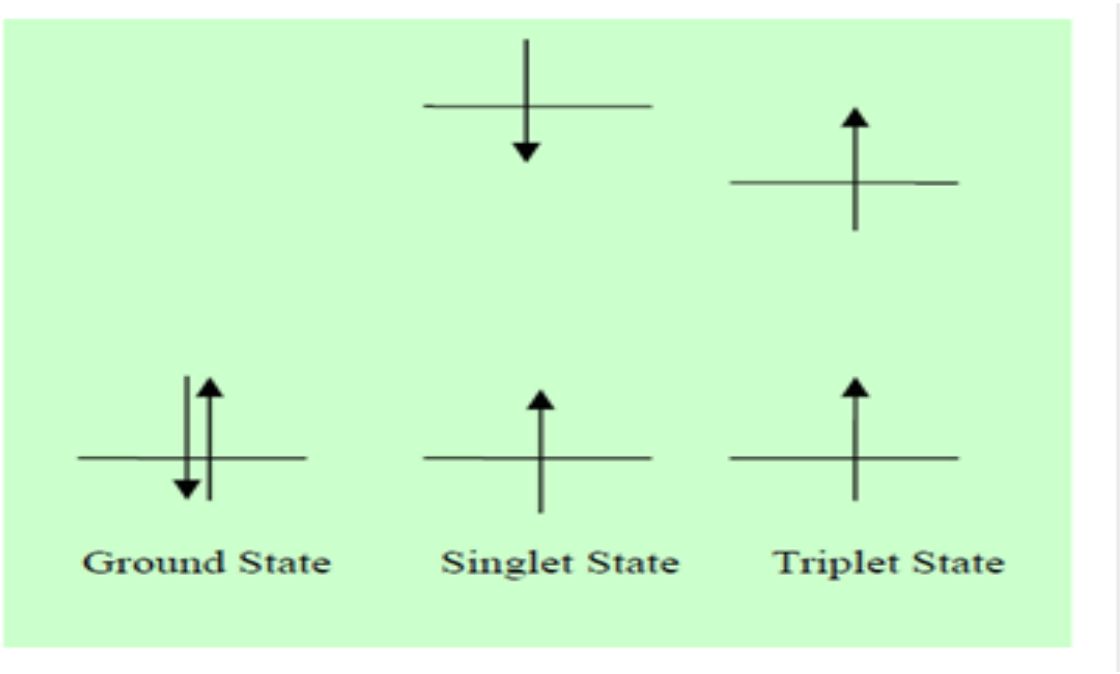

Figure 2.1: Electronic transitions, paired electrons in ground, singlet and triplet state [4].

2.1.1. Singlet and Triplet States

Electrons in molecular orbitals are paired, according to Pauli Exclusion Principle. When an electron absorbs enough energy it will be excited to a higher energy state; but will keep the orientation of its spin [5]. The molecular electronic state in which electrons are paired is called a singlet transition. On the other hand, the molecular electronic state in which the two electrons are unpaired is called a triplet state. The triplet state is achieved when an electron is transferred from a singlet energy level into a triplet energy level, by a process called intersystem crossing; accompanied by a flip in spin [5].

In a singlet state, the spins of the two electrons are paired and thus exhibit no magnetic field and called diamagnetic. Diamagnetic molecules, containing paired electron, are neither attracted nor repelled by a magnetic field. On the other hand, molecules in the triplet state have unpaired electrons and are thus paramagnetic which means that they are attracted to magnetic fields [5]. The terms singlet and triplet stems from the definition of multiplicity where:

$$\text{Multiplicity} = 2S + 1 \tag{2.1}$$

where, S is the total spin. The total spin for a singlet state is zero (-1/2, +1/2) since electrons are paired which gives a multiplicity of one (the term singlet state).

$$\text{Multiplicity} = (2 * 0) + 1 = 1 \tag{2.2}$$

In a triplet state, the total spin is one (the two electrons are unpaired) and the multiplicity is three:

$$\text{Multiplicity} = (2 * 1) + 1 = 3 \tag{2.3}$$

It should also be indicated that the probability of a singlet to triplet transition is much lower than a singlet to singlet transition. Therefore, the intensity of the emission from a triplet state to a singlet state is much lower than emission intensities from a singlet to a singlet state.

A complex is luminescent if it emits light upon absorption of a radiation. The absorption process, governed by quantum mechanical selection rules, occurs primarily between the ground state S0 and the singlet states S1, S2, etc. Superimposed on each of the electronic levels is a set of sublevels associated with the vibrational and rotational energy of the molecule. The principal fluorescence emission is generally induced by the transition from the lowest excited singlet state S1 to the ground state, irrespective of the initial state excited. This can be ascribed to the rapid nonradiative process of internal conversion between higher excited states S2, S3,..., etc. and the lowest excited state S1 [5].

Nonradiative processes can also be observed in intersystem crossing from the singlet manifold to the triplet manifold and vice versa. These singlet–triplet transitions, albeit forbidden by quantum mechanics, will still occur but progress at significantly slower time scales than singlet–singlet transitions [5]. The radiative decay from the excited triplet state back to a singlet state is known as phosphorescence. For a given molecule, the probability of nonradiative energy losses is much higher in the triplet state than in the singlet state because of the substantially longer lifetime of the triplet state. Phosphorescent molecules have the ability to store light energy and release it gradually [5].

Figure 2.2 is the Jablonski energy level diagram showing principal luminescence processes in an organic molecule (left: singlet manifold; right: triplet manifold). The full and dotted arrows represent radiative and non-radiative processes. [5].

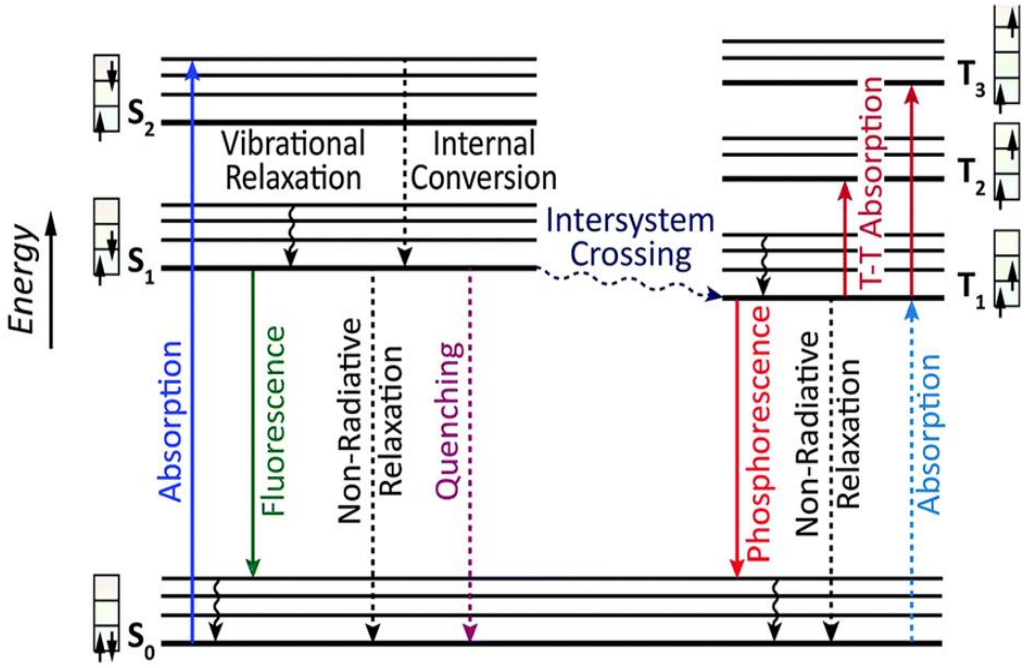

Figure 2.2: Schematic representation of Jablonski energy level diagram showing different luminescence processes and their transitions[5].

2.2. Luminescence

Luminescence is the process of emission of light from phosphor materials, when excited by certain external energy, and then the excitation energy is given off as light [6]. It is divided into two types, namely fluorescence and phosphorescence. Fluorescence is emission of light by material whilst is still subjected to the excitation source, and the luminescence stops immediately after the excitation source has been removed. Phosphorescence is the emission of light from material exposed to radiation and persisting as an afterglow after the exciting radiation has been removed [6]. There are different types of luminescence such as cathodoluminescence, electroluminescence, photoluminescence and thermoluminescence [6].

2.2.1. Photoluminescence

Photoluminescence is a process in which a substance absorbs photons and then re-radiates photons [7]. It can be further described as an excitation to a higher energy state and then a return to lower energy state accompanied by the emission of a photon. The period between absorption and emission is typically extremely short, in order of 10 nanoseconds. The electron is excited from the valance band to conduction band and is then when returning the energy is given off in a form of light from high energy level to the valance band [7]. Incorporation of dopants in the host material may cause change in host transition if the luminescence is emitted by dopants. The emission can be from different transition levels of dopants as well. The optical emission associated with photoluminescence is generally into two types: intrinsic and extrinsic [7].

2.2.2 Intrinsic photoluminescence

The intrinsic luminescence is native to host materials and involves band-to-band recombination of electron-hole pairs. It is also associated with lattice defects (anion vacancies) within the minerals. This type of luminescence is referred to as a defect center. Band-to-band emission results from the recombination of an electron in the conduction band with a hole in the valence band. This can generally only be observed in pure crystals at relatively low temperatures since band-to-band luminescence is quenched at high temperatures and samples must be cooled when one wants to observe it. An exception is ZnO, for which the band-to-band luminescence can be observed even at room temperature because of its large exciton binding energy [8]. There are several factors that may influence intrinsic photoluminescence such as: non-stoichiometry which is a state of material (semiconductor) not having exactly the correct elemental proportion, and structural imperfection owing to poor ordering, radiation damage, or shock damage [9].

2.2.3 Extrinsic photoluminescence

Extrinsic photoluminescence is divided into two categories, namely localized and delocalized luminescence. In localized luminescence the excitation and emission processes are confined in a localized luminescence center, the host lattice does not contribute to luminescence process [9]. Delocalized luminescence, the excited electrons and holes of the host lattice participate in the luminescence process. The intrinsic and extrinsic photoluminescence processes are illustrated in Figure 2.3.

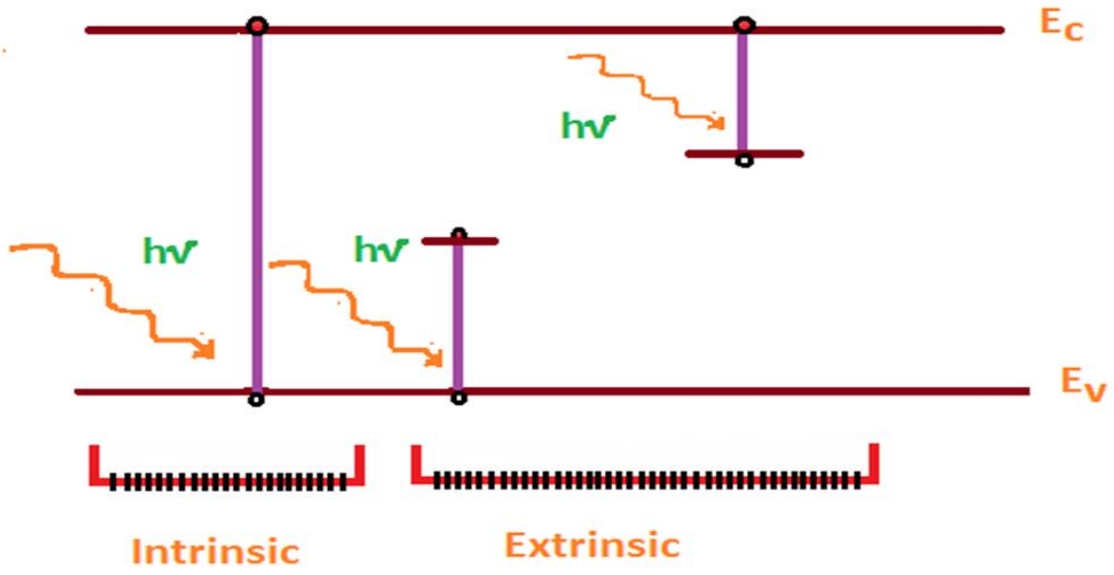

Figure 2.3: An illustration of intrinsic and extrinsic photoluminescence [10].

2.2.4 Quenching of Luminescence

Quenching of luminescence is a process which decreases the luminescent intensity of a substance. Luminescence quenching can be caused by variety of processes, such as addition of impurities to the phosphor, when the concentration of the luminescent substance is increased, when the luminescent substance is heated, or when the substance is exposed to infrared radiation or an electric field. The luminescence quenching reported in this study is due to increased concentration of the luminescence substances [11].

2.3 Application of phosphors

Applications of the phosphors synthesized in this study are catalysts, sensors, photoelectron devices, medicine, refractory materials, heating apparatus and infrared optics, adsorption, synthesis of refractory ceramics, water purification, optoelectronics, microelectronics, additives in heavy fuel oil, paint, gas separation, bactericides, insulator in industrial cables, crucibles and photonic devices [12]. For the purpose of this study the phosphors fabricated can be used for photocatalysis purposes, in the fabrication of solar cells. Figure 2.4 is an illustration depicting phosphors under UV excitation.

Figure 2.4: An illustration of phosphors under UV excitation. [12].

2.3.1. Mechanism of semiconductors in photocatalysis

When a semiconductor nanoparticle is irradiated by the light of energy higher or equal to the band gap energy, an electron from the VB is excited to the CB with simultaneous generation of a hole (h+) in the VB [13]. Then the defects benefit the efficient separation of the generated (e-/h+) pairs. The photo generated electrons reacted with O_2 or oxygen species to produce super oxide anion radicals (O^{2-}) whereas the photo generate holes react with water molecules to generate the hydroxyl radicals (OH) [13]. Both radicals are oxidizing species in the photocatalytic oxidation processes. During the photocatalytic process the hydroxyl is recognized to be the most powerful oxidizing species which can attack organic pollutants which are near the surface of the photocatalyst and can turn them into water and CO_2. High charge separation rate is beneficial to form hydroxyl radical. It can be concluded that more active defect sites may provide much help to improve products photocatalytic properties [13].

Considering the fact that photocatalytic reactions mainly occur on the catalyst surface, increasing the surface area, increasing defects, and decreasing of band gap were the previously employed methods to increase the photocatalytic reaction rate [13]. Figure 2.5 is an illustration of semiconductors in the photocatalytic mechanism.

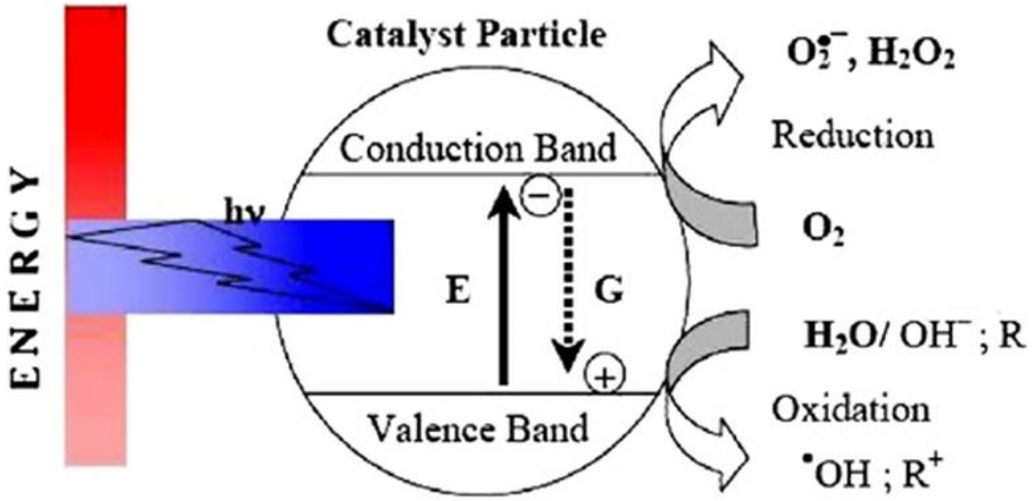

Figure 2.5: Mechanism of semiconductor photocatalysis [14].

2.3.2. ZnO and its photocatalytic characteristics

This study was mainly centered on altering and improving the photocatalytic hence optical properties of zinc oxide (ZnO). ZnO has a high surface reactivity owing to a large number of native defect sites arising from oxygen nonstoichiometry, therefore it has emerged to be an efficient photocatalyst material compared to other metal oxides [15-17]. ZnO exhibits

comparatively higher reaction and mineralization rates [18] and can generate hydroxyl ions more efficiently than titanium oxide (TiO_2) [19]. ZnO has been often considered as a valid alternative to TiO_2 because of its good optoelectronic, catalytic and photochemical properties along with its low cost. Due to the position of the valence band of ZnO, the photo generated holes have strong enough oxidizing power to decompose most organic compounds [20].

Surface area and surface defects play an important role in the photocatalytic activity of metal-oxide nanostructures, as the contaminant molecules need to be adsorbed on to the photocatalytic surface for the redox reactions to occur. The higher the effective surface area, the higher will be the adsorption of target molecules leading to better photocatalytic activity [21].

Doping of metal oxides with metals and / or transition metals creates quasi-stable energy states within the band gap (surface defects) [21], thereby affecting the optical and electronic properties [22]. Increased electron trapping due to higher defect sites leads to enhancement in the photocatalytic efficiency. This increase in photocatalytic efficiency is possible provided the electron-hole pair recombination rate is lower than the rate of electron transfer to adsorbed molecules. Photocatalytic activity comparable to doped ZnO was also observed with engineered defects in ZnO crystals achieved by fast crystallization during synthesis of the nanoparticles [23].

With regards to this study Mg^{2+} and Sr^{2+} were selected as dopant cations to enhance and improve the photocatalytic behavior and efficiency of ZnO. The crystalline structures of hexagonal wurtzite ZnO, cubic MgO and SrO are depicted in figure 2.6 (a-c). These pure and doped materials have been extensively studied in the chapters that follow.

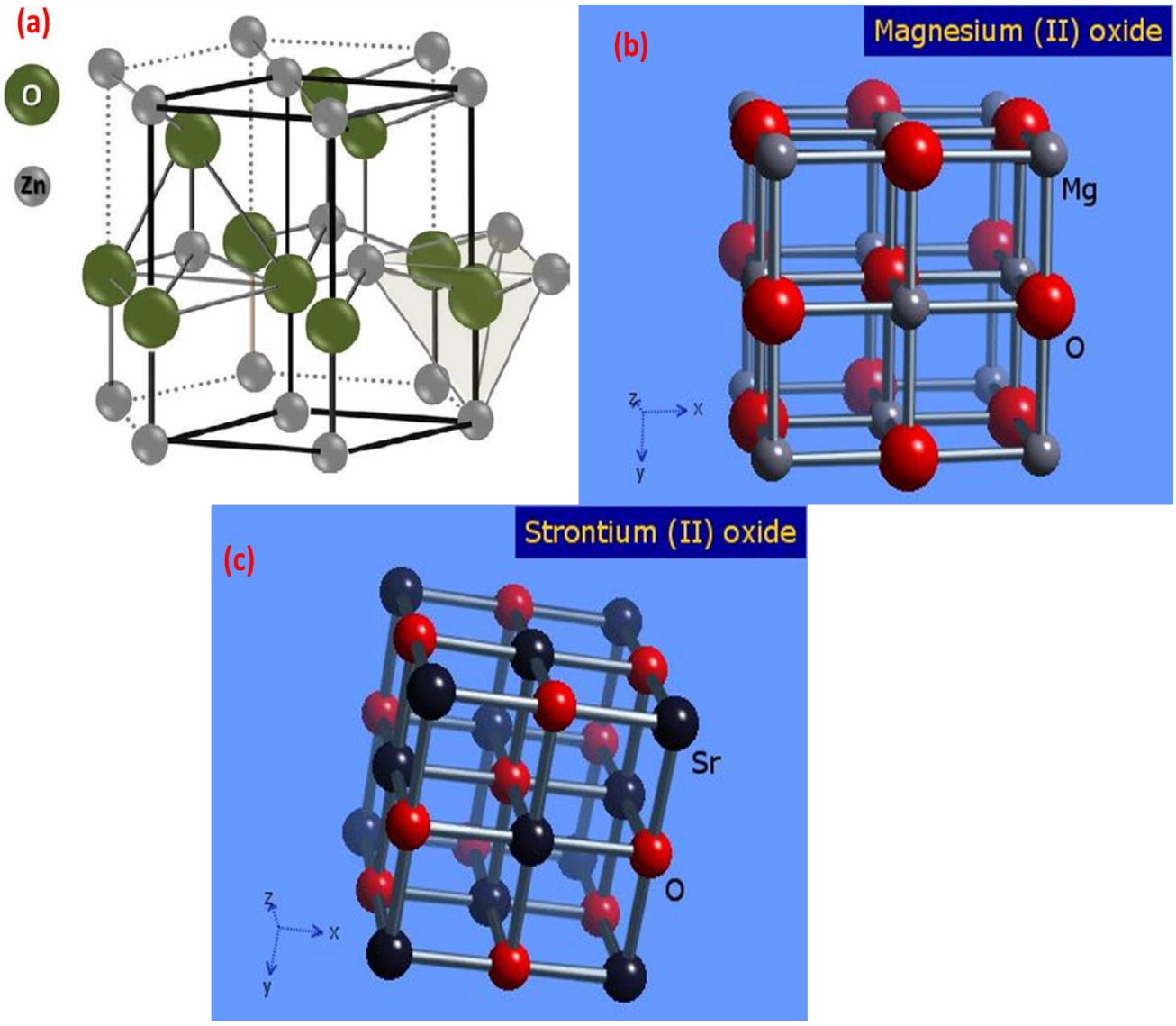

Figure 2.6 (a-c) : The crystalline structure of a hexagonal wurtzite ZnO [23], cubic MgO [24] and of cubic SrO [25].

References:

[1] Ronda C.R., Luminescence from Theory to Applications, Willy-VCH, Germany, (2008) pp 3

[2] Yamamoto, H. Fundamentals of luminescence. CRC Press: New York, Chap. 2, (2007).

[3] Lephoto M.A. MSc Thesis, University of the Free State, South Africa, 2011.

[4] http://www.rp-photonics.com/photoluminescence.html [Accessed Sep 2016]

[5] Sithole T.M. MSc Thesis, University of the Free State, South Africa 2015.

[6]http://shodhganga.inflibnet.ac.in/bitstream/10603/6157/8/08_chapter%201.pdf [Accessed December 2013]

[7] http://en.wikipedia.org/wiki/Photoluminescence [Accessed December 2016]

[8] Vij D.R., Luminescence of Solids, Plenum Press, New York (1998), 95-102.

[9] Mothudi B.M., Swart H.C., Ntwaeaborwa O.M., Ph. D dissertation, University of the Free State, South Africa, 2009

[10] http://swissen.in/photoluminescence.php [Accessed December 2016]

[11]http://encyclopedia2.thefreedictionary.com/Quenching+of+Luminescence[Accessed December 2016]

[12] http://nanomaterialstore.com/nano-phosphor.php [Accessed December 2016]

[13] Danli, Jian-Feng Huang, Li-Yun Cao, Microwave hydrothermal synthesis of Sr doped ZnO Crystallites with enhanced photocatalytic properties. Ceramics International 40 (2014) 2647-2653.

[14] Matsuoka M.; Kitano, Takeuchi M., Tsujimaru M., Anpo K., Thomas M.J.M., Photocatalysis for new energy production Recent advances in photocatalytic water splitting reactions for hydrogen production. Catalysis Today 2007 122 51–61.

[15] Ali, A. M.; Emanuelsson, E. A. C.; Patterson, D. A. Appl. Catal. B, 97, doi: 10.1016 /j.apcatb.2010.03.037 (2010), 168–181.

[16] Pardeshi, S. K.; Patil, A. B. J. Mol. Catal. A: Chem. doi:10.1016 /j.molcata. 2009.03.023, (2009) 308, 32–40.

[17] Qamar M.; Muneer M. Desalination 2009, 249, doi:10.1016 /j.desal.01.022 (2009), 535–540.

[18] Poulios, I.; Makri, D.; Prohaska, X. Global NEST, 1, (1999), 55–62.

[19] Carraway, E. R.; Hoffman, A. J.; Hoffmann, M. R. Environ. Sci. Technol., 28, doi:10.1021/es00054a007 (1994) 786–793.

[20] Miyauchi M., Nakajima A., Watanabe T., Hashimoto K., Photocatalysis and photo induced hydrophilicity of various metal oxide thin films, Chem. Mater. 14, (2002) 2812–2816.

[21] Wang R.; Xin J. H.; Yang Y.; Liu H.; Xu L.; Hu, doi:10.1016/j.apsusc.2003.12.012 , J. Appl. Surf. Sci., 227, (2004) 312–317.

[22] Baruah S.; RafiqueR. F.; Dutta, doi:10.1142 /S17932920080 0126X , J. NANO, 3, (2008) 399–407.

[23] http://www.edn.com/Home/PrintView?contentItemId=4391796 [Accessed November 2016]

[24] https://www.webelements.com/compounds/magnesium/magnesium_oxide.html [Accessed November 2016]

[25] https://www.webelements.com/compounds/strontium/strontium_oxide.html [Accessed November 2016]

Chapter 3: Synthesis method and Research Techniques

3.1. Background

The Science of Nanomaterials is proving to be one of the most attractive and promising fields for technological development in this century. In scientific literature several terms related to nanoscience can be found of which they are worth highlighting: nanoparticles, nanocrystals, nanofibers, nanotubes and nanocomposites. In fact, all these are related to nanostructured materials which have well defined optical, structural and luminescent features [1].

The physical and chemical properties of these materials at the nanometer scale (usually set in the range of 1–100 nm) are of immense interest and increasing importance for future technological applications especially in the context of solid state lighting and photocatalysis. Nanostructured materials often exhibit different properties when compared to other materials. The relationship between particle size, luminescence and structural properties has been known since the nineteenth century, when Faraday showed that the colour of colloidal Au particles can be modified depending on their size. However, despite the long history of their discovery, the interest in nanostructured materials has only increased significantly in the last 15 years [2].

The research activities related to this area were driven by the ability to control material properties like absorption, morphology and luminescence by controlling the size of the particles. The ability to synthesize crystallites at the nanometer scale with precisely controlled size and composition, and to assemble them into large structures with unusual properties and functions will revolutionize all segments of material manufacturing for industrial applications [3].

Combustion synthesis method is a complex sequence of chemical reactions between a fuel and an oxidant accompanied by the production of heat or both heat and light in the form of either a glow or flame. For combustion to occur, fuel and oxidizer are required as reactants, i.e., the substances present before the reaction can take place. When the mixture of fuel and oxidizer is ignited, combustion takes place. During the combustion process, large volume of gases evolve giving rise to agglomeration thus leading to the formation of fine powders with nanostructures. Release of heat during the combustion reaction depends on the fuel-oxidant stoichiometry in the precursor composition. For the combustion synthesis of oxides, metal

nitrates are used as oxidizer, and fuels used are hydrazine-based compounds, citric acid, or urea [3].

Table 3.1: Tabulated advantages and disadvantages of solution combustion synthesis method

Advantages	Disadvantages
❖ Low cost and low temperature processing when compared to traditional solid state reaction. ❖ Better control of stoichiometry. ❖ Crystalline size of the final oxide products produced by this method is invariably in the nanometer range. ❖ Exothermic reaction makes product almost instantaneously ❖ Possibility of multicomponent oxides with single phase and high surface area. ❖ Large number of gas evolved during combustion results in a porous product in which the agglomerates formed are so weak that they can be easily crushed and ground into a fine powder [4].	❖ Contamination due to carbonaceous residue, particle agglomeration, poor control on particle morphology. ❖ Understanding of combustion behaviour is needed to perform the controlled combustion in order to get final products with desired properties [4].

3.1.1. Solution Combustion synthesis

Solution combustion synthesis (SCS) is a synthesis method for the preparation of highly pure and homogeneous powders, it is especially interesting for obtaining nanocrystalline powders such as ceramic oxides. SCS makes use of salts, such as nitrates, metal sulphates and carbonates, as oxidants and, reducing reagents, fuels such as glycine, sucrose, urea, or other water soluble carbohydrates. Nitrate acts as an oxidizer for the fuel during the combustion reaction. The powder can be a pyrolysed product of a single phase, but usually it is a combination of metal oxides and in some cases it requires subsequent heat treatment to form single-phase products, which are usually the result required in this process [4].

SCS is a method based on the principle that once a reaction is initiated under heating, an exothermic reaction occurs. This becomes self-sustaining within a certain time interval, resulting in a powder as final product. The exothermic reaction begins at the ignition temperature and generates a certain amount of heat that is manifested in the maximum temperature or temperature of combustion. Advantages of SCS are given in Table 3.1.

There are several parameters influencing the reaction such as the type of fuel, fuel-oxidizer ratio, use of excess oxidizer, ignition temperature, and amount of water contained in the precursor mixture. The characteristics of the powders obtained as products, such as crystallite size, surface area, nature of agglomeration (strong and weak) are governed mainly by the enthalpy and flame temperature generated during combustion. This is dependent on the nature of the fuel and the kind of fuel-oxidizer used in the reaction [5].

The rapid generation of a large volume of gases during combustion dissipates the heat from the process and limits the temperature rise, reducing the possibility of premature sintering between the primary particles. The generation of gases also assists in the limiting of inter-particle contact, resulting in a more powdery product. The main parameters of combustion that have been widely investigated in this thesis are: type of flame, temperature, generated gases, fuel-oxidant ratio and chemical composition of the precursor reagents [5].

3.1.2. Flame types

SCS in general under controlled conditions generates a peculiar kind of burning or smoldering type flame, depending on the employed fuel and oxidizer-fuel ratio. The burning flame can endure for seconds or even minutes, while the smoldering flame does not rise or is extinguished in a few seconds. The type of flame in the combustion plays an important role in controlling the particle size of as-synthesized powders [5].

In any combustion process the mixture of the reactants (fuel and oxidizer) may be hypergolic (ignition by contact) or the ignition may be controlled by an external source. These conditions are crucial for generating the flame. There is a dependence on the type of flames, linked to the fuel used, as can be seen in the use of urea, which acts more reactive leading to the formation of flame glow, than a solution in the presence of glycine, characterized by smoldering. The reactivity of the combustion reaction is dependent on the ligand groups of the molecules of the fuel and the compositional ratio of fuel and oxidant [5].

3.1.3. Characteristic Temperatures

During the combustion synthesis reaction, there are four important temperatures that can affect the reaction process and final product properties:
Initial temperature (T_o): is the average temperature of the reagent solution before the reaction is ignited;
Ignition temperature **(T_{ig}):** represents the point at which the combustion reaction is dynamically activated without an additional supply of external heat;
Adiabatic flame temperature (T_{ad}): is the maximum combustion temperature achieved under adiabatic conditions;

Maximum flame temperature (T_m): is the maximum temperature reached in the actual configuration, i.e., under conditions that are not adiabatic [6].

3.1.4. Gas Generation

It is a well-established fact that in combustion synthesis the powder morphology, particle size and surface area are directly related to the amount of gases that escapes during combustion. The gases break large clusters and create pores between particles. In fact the clusters are disintegrated in conditions of high production of combustion gases and in these conditions more heat is released from the system hindering particle growth. The difference in particle size using different fuels depends on the number of moles of gaseous products released during combustion [6].

3.1.5. Fuel-Oxidant Ratio

A fuel is a substance capable of burning the CH bonds (electrons acceptor). An oxidant is a substance that helps in burning, providing oxygen (electrons donor). Only when the oxidizer and fuel are intimately mixed in an appropriate proportion, an exothermic chemical reaction is initiated and generated substantial heat to decompose the precursors into the desired ceramic oxide products [6].

The ratio of fuel to oxidizer is considered as one of the most important parameters in determining the properties of powders synthesized by combustion. Product properties such as crystallite size, surface area, morphology, phase, degree and nature of agglomeration, are generally controlled by adjusting the fuel-oxidant ratio. The fuel-oxidant ratio determines the influence of gases on the morphology of the particles. The pore size depends on the fuel-oxidant ratio, because the greater the amount of fuel, the larger the pore size of the particles [6].

3.1.6. Chemical Composition of Precursor Chemicals

The solubility of the fuel, amount of water and type of fuel used are critical. Excellent product homogeneity is achieved by the appropriate stoichiometric amount of chemical precursors mixed. That happens when oxidants and fuels are completely dissolved in water forming a homogeneous solution. The fuel also serves as complexing agent limiting the precipitation of individual precursor components prior to ignition [6].

3.1.7. Fuels

Urea (NH_2CONH_2) is an attractive fuel for the formation of powders with crystallite sizes in the submicron/nanosized range. It acts as a good complexing agent for metal ions because it contains two amino groups located at the extremes of its chemical structure. The chemical activity of the ligand-NH_2 promotes more vigorous combustion reactions among various fuels studied [6].

3.1.8. Oxidants

Nitrates are chosen as metal precursors because they are fundamental to the combustion method for providing the metal ion and great water solubility allowing a greater homogenization [6]. Figure 3.1 is a schematic diagram of the solution combustion synthesis method.

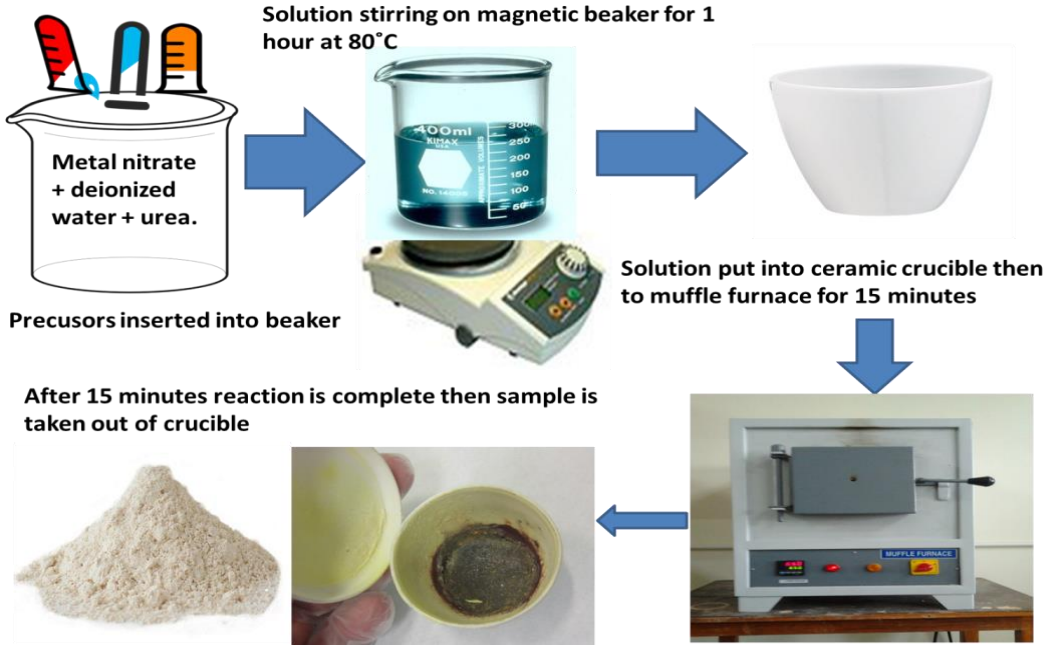

Figure 3.1: Graphical representation for preparation of phosphors using solution combustion synthesis method

3.2. Characterization Techniques

3.2.1 Overview

This section of this chapter gives a brief description of the theory of different research characterization techniques used in this study to characterize the phosphor materials. The

characterization techniques are x-ray diffraction (XRD), x-ray photoelectron spectroscopy (XPS), Fourier Transform Infrared Spectroscopy (FTIR), scanning electron microscopy (SEM), high resolution transmission electron microscopy (HR-TEM), selected area electron diffraction (SAED), UV-Vis spectrophotometry (UV-Vis) and photoluminescence (PL) spectroscopy.

3.2.2 Introduction to Diffraction

Materials are made of atoms. Knowledge of how atoms are arranged into crystal structures and microstructures is the foundation on which we build our understanding of the synthesis, structure and properties of materials [7].

In a diffraction experiment, an incident wave is directed into a material and a detector is typically moved about to record the directions and intensities of the outgoing diffracted waves. "Coherent scattering" preserves the precision of wave periodicity [7]. Constructive or destructive interference then occurs along different directions as scattered waves are emitted by atoms of different types and positions [8]. There is a profound geometrical relationship between the directions of waves that interfere constructively, which comprise the "diffraction pattern," and the crystal structure of the material. The diffraction pattern is a spectrum of real space periodicities in a material [8].

Atomic periodicities with long repeat distances cause diffraction at small angles, while short repeat distances (as from small interplanar spacings) cause diffraction at high angles. Much more information about a material is contained in its diffraction pattern [9]. Crystals with precise periodicities over long distances have sharp and clear diffraction peaks. Crystals with defects (such as impurities, dislocations, planar faults, internal strains, or small precipitates) are less precisely periodic in their atomic arrangements, but they still have distinct diffraction peaks. Diffraction experiments are also used to study the structure of amorphous materials [9].

3.3. X-RAY DIFFRACTION (XRD)

X- ray diffraction is a versatile analytical technique for examining the crystalline structure of solid materials, which include ceramics, metals, electronic materials, organics and polymers. It is also used for identification of phases, determination of crystallite size, lattice constants, and degree of crystallinity in a mixture of amorphous and crystalline materials [10]. It can provide valuable information about the crystalline phase and average crystallite size. The crystal size measured by this technique is smaller than the measurement limit of the optical or electronic microscope [10].

The materials may be powders, multilayer thin films, fibres, sheets or irregular shapes, depending on the desired measurements [11]. The x-ray diffractometer falls broadly into two classes: single crystal and powder. The powder diffractometer is routinely used for phase

identification and quantitative phase analysis. The x-ray diffractometer consists of three basic elements: an X-ray tube, a sample holder, and an X-ray detector [11]. The X-rays are produced in a cathode ray tube by heating a filament to produce electrons. When the voltage is applied, the electrons will accelerate towards the target material. When electrons have sufficient energy to dislodge the inner shell electrons of the target material, characteristic X-ray spectra will be produced [12]. These X–ray spectra consist of several components, and the most common are Kα and Kβ. The target materials that are usually used are Cu, Fe, Mo and Cr. Each of these has specific characteristic wavelengths [12].

In order to generate the required monochromatic X-rays needed for diffraction, a filter such as a foil or crystal monochrometers is usually used. Copper is the most commonly used target material for single-crystal diffraction, with Cu Kα radiation = 1.5418Å [13]. The resulting X-rays are collimated and directed onto the sample. As the sample and detector are rotated, the intensity of the reflected X-rays is recorded [13]. When the geometry of the incident X-rays impinging on the sample satisfies the Bragg Equation, constructive interference occurs and characteristic diffraction peaks of the sample will be observed [13]. Figure 3.2 illustrates the diffractometer used in this study, which was the D8 Advance AXS GmbH X-ray diffractometer. The XRD patterns were recorded in the 2θ range of 10°-80° at a scan speed of 0.02° s^{-1}, accelerating voltage of 40 kV and current of 40 mA. A continuous scan mode with coupled 2θ scan type was used.

Figure 3.2: The D8 Advance AXS GmbH X-ray diffractometer

3.3.1. Formation of Bragg's diffraction:

In a crystalline material, the incident X-ray beam that diffracts from various planes of atoms at a certain angle (2θ) can interfere constructively resulting in an increased intensity of the reflected beam [14]. This intensity is displayed by a peak in the XRD plot, which is associated with d-spacing values of the corresponding structure [14].

The X-rays are generated in a cathode ray tube by heating a filament to produce electrons, which are then accelerated towards a target by applying a voltage [15]. When the electrons have sufficient energy to dislodge inner shell electrons of the target material, characteristic X-ray spectra are produced. The interaction of incident rays with the sample produces constructive interference when the conditions satisfy Bragg's Law as expressed in equation 3.1:

$$n\lambda = 2dSin\theta \tag{3.1}$$

where λ is the wavelength of the incident X-rays, d is the distance between lattice planes, θ is the angle of incidence with lattice plane [15]. This law relates the wavelength of electromagnetic radiation to the diffraction angle and lattice spacing in a crystalline sample as shown in figure 3.3. The figure shows the x-rays waves incident on the parallel planes of atoms in the crystal, with each plane reflecting at a very small fraction in the radiation [15]. The diffracted beams are formed when the reflections from the parallel planes of atoms interfere constructively [15].

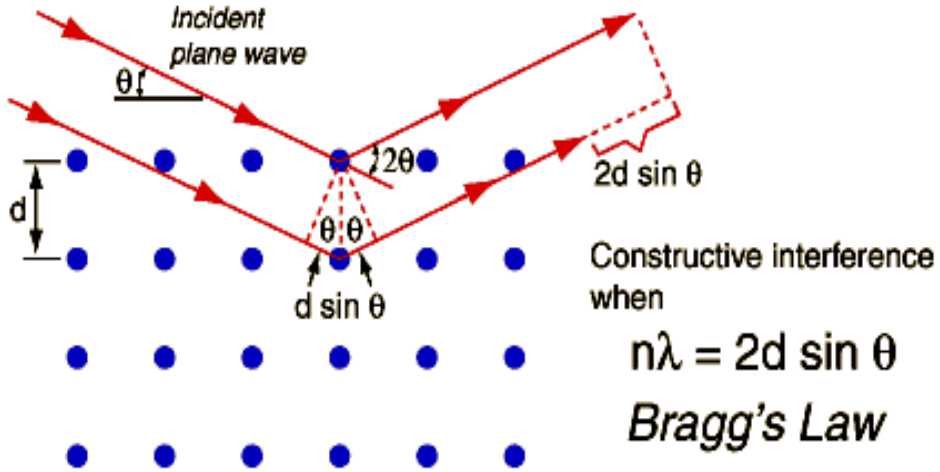

Figure 3.3: Schematic of the reflection of x-rays by crystal planes [16].

By scanning the sample through a range of 2θ angles when the detector is rotated at double angular velocity, all possible diffraction directions of the lattice should be attained due to the random orientation of the powdered material [17]. The recorded spectrum consists of several components, the most common being K_α and K_β. The specific wavelengths are characteristics

of the target material such as copper (Cu), iron (Fe), molybdenum (Mo), and chromium (Cr). Copper is the most common target material for single-crystal and powder diffraction, with CuK_α radiation = 1.5418Å [17]. The X-rays are collimated and directed onto the sample. As the sample and detector are rotated, the intensity of the reflected X-rays is recorded. The crystalline phases are determined from the diffraction patterns. The width of the diffraction lines correlates with the sizes of crystallites [17]. As the crystallite sizes decrease, the line width is broadened due to loss of range order relative to the bulk. The average crystallite size, *D*, can be estimated from the broadened peaks by using Scherrer equation:

$$D = \frac{0.9\lambda}{\beta Cos\theta} \tag{3.2}$$

where β is the full width at half maximum of a diffraction line located at an angle θ, and while λ is the X-ray Diffraction wavelength [17].

3.4. X-ray Photoelectron Spectroscopy

XPS is a quantitative spectroscopic technique that measures the elemental composition, empirical formula, chemical state and electronic state of the elements that exist within a material [18]. It is routinely used to measure organic and inorganic compounds, metal alloys, semiconductors, polymers, catalysts, glasses, ceramics, paints, papers, inks, woods, bio-materials and many others [18]. The sample is irradiated with low-energy (~1.5 keV) X-rays while simultaneously measuring the kinetic energy and number of electrons that escape from the top 1 to 10 nm of the material being analyzed. Figure 3.4 shows the schematic diagram of XPS technique. X-ray excitation ejects electrons from the core level of the atoms, which will be accelerated to the detector via the cylindrical mirror analyzer as shown in the figure 3.4 [18].

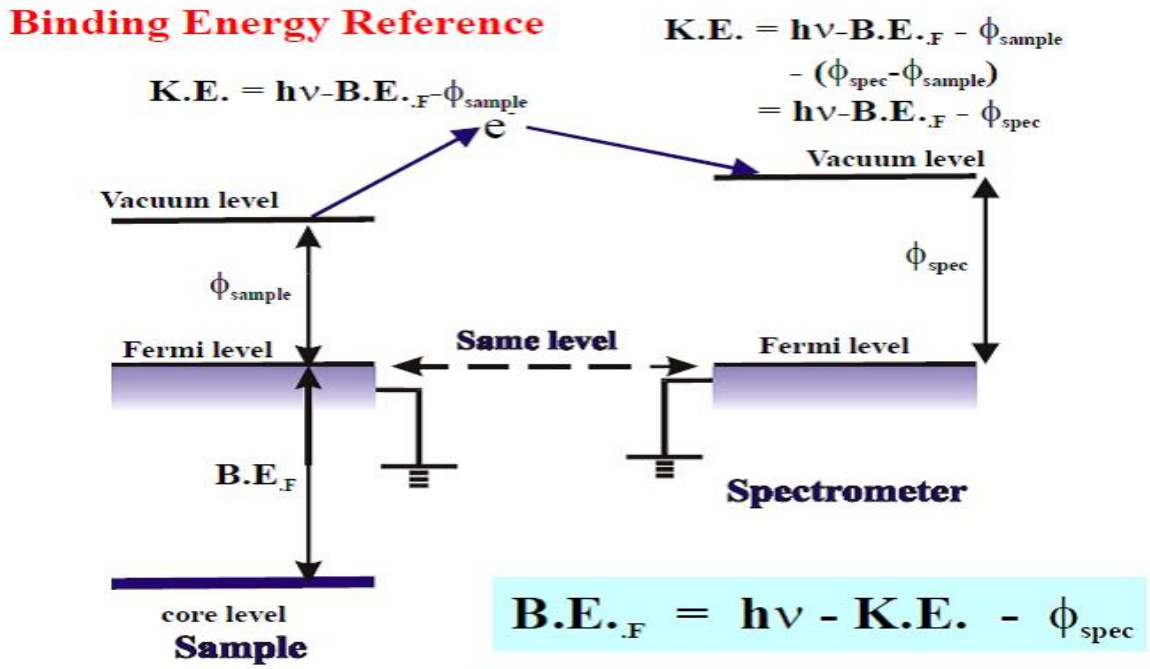

Figure 3.4: Schematic diagram of the XPS technique [19].

The energy spectrum of the emitted photoelectron is determined by means of a high-resolution electron spectrometer [20]. The kinetic energy (K.E.) of the emitted photoelectron is related to the x-ray energy of an atomic binding energy (B.E.) by Einstein's equation for photoelectric effect:

$$B.E. = h\upsilon - K.E. - \phi_{spec} \ , \tag{3.3}$$

where hυ is the energy of the primary x-ray photons, K.E. is the kinetic energy of the electron measured by the instrument and ϕ_{spec} is the work function of the spectrometer [20]. Each element produces a characteristic set of XPS peaks at characteristic binding energy values that directly identify each element that exists on the surface of the material being analyzed. These characteristics peaks correspond to the electron configuration of the electron within the atoms, e.g., 1s, 2s, 2p, 3s, 3p, 3d etc [20]. The number of detected electrons in each of the characteristic peak is directly related to the amount of element within the irradiated area. The sample analysis is conducted in an ultra-high vacuum (UHV) chamber, because electron counting detectors in XPS instruments are few meters away from the material irradiated with X-rays [20].

XPS surveys are done with 100 μm, 25 W, and 15 kV x-ray monochromatic beam. Depth profiling are done with 2 kV, 2 μA, and 1×1 mm raster – Ar ion gun, with a sputter rate of about 170 Å/min . Figure 3.5 shows the Versa Probe II Scanning XPS Microprobe used during the measurements [20].

Figure 3.5: PHI 5000 Versa Probe II Scanning XPS Microprobe [20].

3.5 Fourier Transform Infrared Spectroscopy (FTIR)

The original infrared instruments were of the dispersive type. These instruments separated the individual frequencies of energy emitted from the infrared source. This was accomplished by the use of a prism or grating. An infrared prism works exactly the same as a visible prism which separates visible light into its colours (frequencies) [21]. A grating is a more modern dispersive element which better separates the frequencies of infrared energy. The detector measures the amount of energy at each frequency which has passed through the sample. This results in a spectrum which is a plot of intensity vs frequency [21].

Fourier Transform Infrared (FT-IR) spectrometry was developed in order to overcome the limitations encountered with dispersive instruments. The main difficulty was that it's a slow scanning process. A method for measuring all of the infrared frequencies simultaneously, rather than individually was needed [21].

A solution was developed which employed a very simple optical device called an interferometer. The interferometer produces a unique type of signal which has all of the infrared frequencies "encoded" into it. The signal can be measured very quickly usually on the order of one second or so. Thus the time element per sample is reduced to a matter of a few seconds rather than several minutes [21].

An infrared spectrum represents a fingerprint of a sample with absorption peaks which correspond to the frequencies of vibrations between the bonds of the atoms making up the material. Each different material is a unique combination of atoms, no two compounds produce the exact same infrared spectrum [21].

Fourier transform infrared spectroscopy is preferred over dispersive or filter methods of infrared spectral analysis for several reasons:

- It is a non-destructive technique
- It provides a precise measurement method which requires no external calibration
- It can increase speed, collecting a scan every second
- It can increase sensitivity- one second scans can be co-added together to ratio out random noise.
- It has greater optical throughout
- It is mechanically simple with only one moving part

3.5.1. How does the interferometer work?

The beam emitted from the source passes through an aperture and controls the amount of energy on the sample. The beam then enters the interferometer, which produce a signal that has spectral encoding into it. The beam is split into two by the beam splitter upon entering the interferometer. One beam reflects off a flat mirror which is fixed in place while the other beam

reflects off a flat mirror which allows this mirror to move very short distance away from the beamsplitter.

The laser beam incident to the interferometer is used for wave calibration, mirror position control and to collect data of the spectrometer. The beam enters the sample where it is transmitted through the sample surface [21]. Then the detector measures the beam intensity. There needs to be a relative scale for the absorption intensity, a background spectrum must also be measured. This is normally a measurement with no sample in the beam [21]. This can be compared to the measurement with the sample in the beam to determine the percent transmittance. This technique results in a spectrum which has all of the instrumental characteristics removed. Thus, all spectral features which are present are strictly due to the sample. A single background measurement can be used for many sample measurements because this spectrum is characteristic of the instrument itself [21]. Figure 3.6 depicts a simplified layout of the FTIR spectrometer [22].

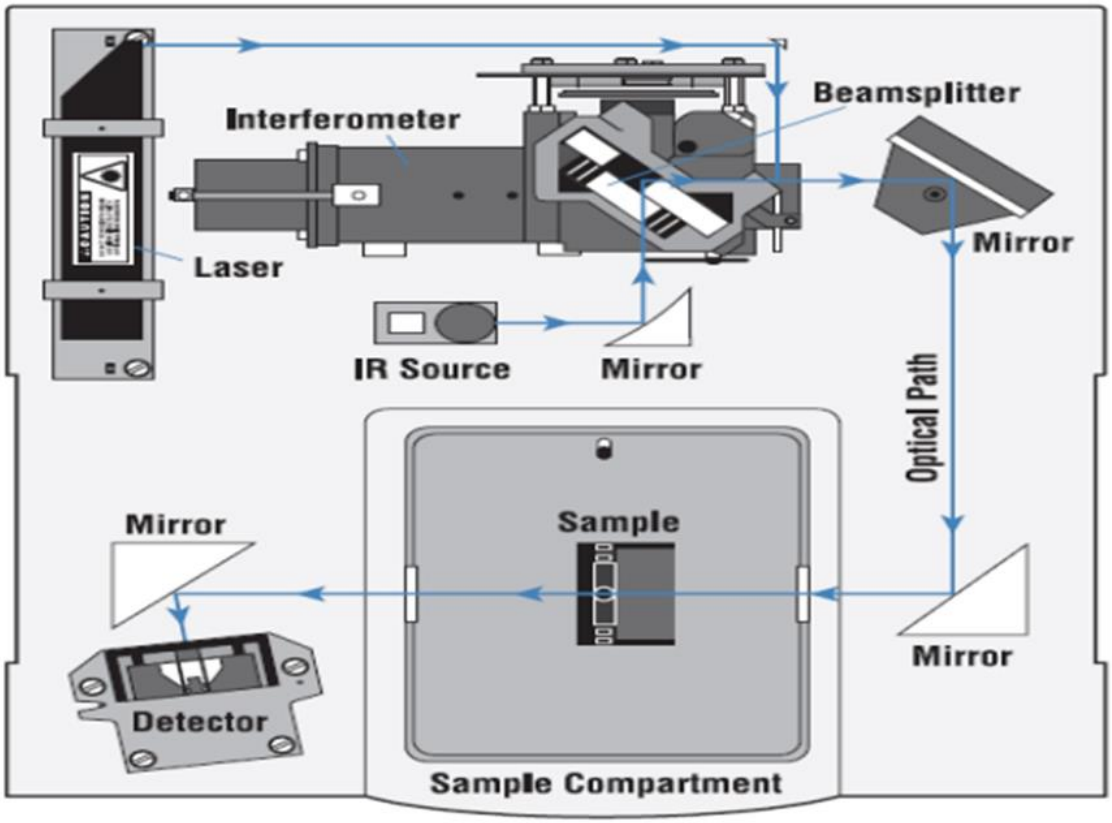

Figure 3.6: A simplified layout FTIR spectrometer [22].

3.6. Transmission Electron Microscopy

HR-TEM is a microscopy technique in which a beam of electrons is transmitted through a very thin sample and it interacts with it as it passes through. Images are formed as a result of the interaction of the electrons and the sample as the electrons are transmitted through the sample [23]. The images are magnified and focused onto imaging devices or detected by sensor such as CCD camera. HR-TEM has the capability to directly image atoms in crystalline samples at resolutions close to 0.1 nm, smaller than interatomic distance. An electron beam can also be focused to a diameter smaller than ~0.3 nm, allowing quantitative analysis from a single nanocrystal. This type of analysis is important for characterizing materials at a length scale from atoms to hundreds of nanometers [23]. It is used to measure the particle size, shape, crystallinity and interparticle interactions. Figure 3.7 below shows the schematic outline of HR-TEM. It consists of four parts namely: electron source, electromagnetic lenses, sample holder and imaging system. The HR-TEM used in this study was JEOL ARM200F transmission electron microscope at the national centre for microscopy at Nelson Mandela Metropolitan University.

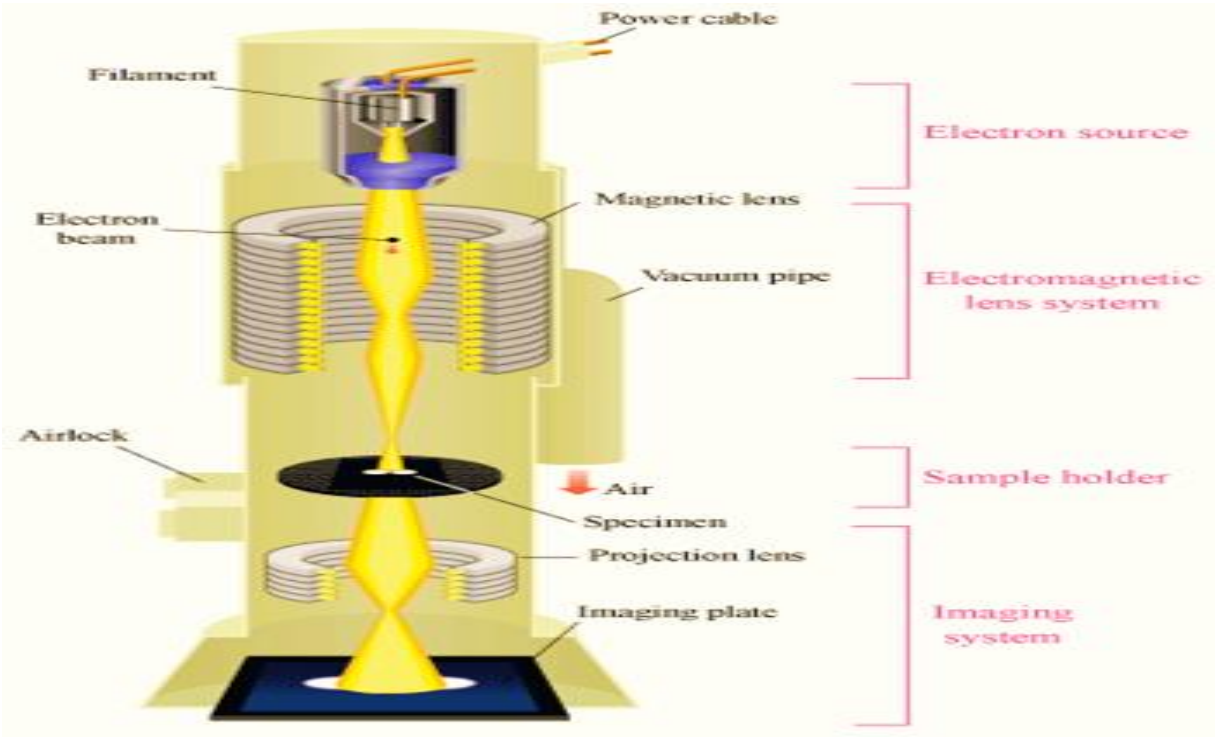

Figure 3.7: Schematic outline of HR-TEM [23].

The electron beam produced in the electron source passes through multiple electromagnetic lenses [24]. It further passes through the solenoids (tubes with coil wrapped around the electron beam) down the column to the specimen then makes a contact with the screen where electrons are converted to light and form an image. The image can be manipulated by adjusting the voltage of the gun to accelerate or decrease the speed of electrons as well as changing the

electromagnetic wavelength via the solenoids [24]. The coil focus image onto a screen or photographic plate. Figure 3.8 shows high-resolution transmission electron microscope ARM 200F.

Figure 3.8: The JEOL JEM-ARM200F HR-TEM [24].

3.7. Scanning Electron Microscopy (SEM)

Scanning electron microscope (SEM) is a microscopy technique uses a focused beam of high-energy electrons to generate a variety of signals at the surface of solid specimens. The signals that derive from electron-sample interactions reveal information about the sample including external morphology (texture), chemical composition, and crystalline structure and orientation of materials making up the sample [25].

In most applications data is collected over a selected area of the surface of the sample and a 2-dimensional image is generated that displays spatial variations in these properties. Areas ranging from approximately 1 cm to 5 microns in width can be imaged in a scanning mode

using conventional SEM techniques (magnification ranging from 20X to approximately 30,000X, spatial resolution of 50 to 100 nm) [25].

The SEM is also capable of performing analyses of selected point locations on the sample; this approach is especially useful in qualitatively or semi-quantitatively determining chemical compositions (using EDS), crystalline structure, and crystal orientations.

3.7.1 Fundamental Principles:

Accelerated electrons in a SEM carry significant amounts of kinetic energy, and this energy is dissipated as a variety of signals produced by electron-sample interactions when the incident electrons are decelerated in the solid sample [25].

These signals include secondary electrons (that produce SEM images), backscattered electrons (BSE), diffracted backscattered electrons (EBSD that are used to determine crystal structures and orientations of minerals), photons (characteristic X-rays that are used for elemental analysis and continuum X-rays), visible light (cathodoluminescence–CL), and heat [25].

Secondary electrons and backscattered electrons are commonly used for imaging samples. Secondary electrons are most valuable for showing morphology and topography on samples, while backscattered electrons are most valuable for illustrating contrasts in composition in multiphase samples (i.e. for rapid phase discrimination). X-ray generation is produced by inelastic collisions of the incident electrons with electrons in discrete orbitals (shells) of atoms in the sample. As the excited electrons return to lower energy states, they yield X-rays that are of a fixed wavelength (that is related to the difference in energy levels of electrons in different shells for a given element) [25].

Thus, characteristic X-rays are produced for each element in a mineral that is "excited" by an electron beam. SEM analysis is considered to be "non-destructive"; that is, x-rays generated by electron interactions do not lead to volume loss of the sample, so it is possible to analyse the same material repeatedly [25].

3.7.2 How does the instrumentation work?

Electrons are produced at the top of the column, accelerated down and passed through a combination of lenses and apertures to produce a focused beam of electrons which hits the surface of the sample. The sample is mounted on a stage in the chamber area and, unless the microscope is designed to operate at low vacuums, both the column and the chamber are evacuated by a combination of pumps. The level of the vacuum will depend on the design of the microscope [26].

Essential components of all SEMs include the following: Electron Source ("Gun"), Electron Lenses, Sample Stage, Detectors for all signals of interest, Data output devices, infrastructure requirements: Power Supply, Vacuum System, Cooling system, Vibration-free floor, Room free of ambient magnetic and electric fields, SEMs always have at least one detector (usually a secondary electron detector), and most have additional detectors [26].

The SEM is routinely used to generate high-resolution images of shapes of objects (SEI) and to show spatial variations in chemical compositions:

- acquiring elemental maps or spot chemical analyses using EDS,
- discrimination of phases based on mean atomic number (commonly related to relative density) using BSE,
- compositional maps based on differences in trace element "activators" (typically transition metal and Rare Earth elements) using CL [26].

3.7.3 Strengths

There is arguably no other instrument with the breadth of applications in the study of solid materials that compares with the SEM. The SEM is critical in all fields that require characterization of solid materials. Most SEM's are comparatively easy to operate, with user-friendly "intuitive" interfaces. Many applications require minimal sample preparation. For many applications, data acquisition is rapid (less than 5 minutes/image for SEI, BSE, spot EDS analyses.) Modern SEMs generate data in digital formats, which are highly portable [26].

3.7.4 Limitations

Samples must be solid and they must fit into the microscope chamber. Maximum size in horizontal dimensions is usually on the order of 10 cm, vertical dimensions are generally much more limited and rarely exceed 40 mm. For most instruments samples must be stable in a vacuum on the order of 10^{-5} - 10^{-6} torr. Samples likely to outgas at low pressures (rocks saturated with hydrocarbons, "wet" samples such as coal, organic materials or swelling clays, and samples likely to decrepitate at low pressure) are unsuitable for examination in conventional SEM's [26].

However, "low vacuum" and "environmental" SEMs also exist, and many of these types of samples can be successfully examined in these specialized instruments. EDS detectors on SEM's cannot detect very light elements (H, He, and Li), and many instruments cannot detect elements with atomic numbers less than 11 (Na). Most SEMs use a solid state x-ray detector (EDS), and while these detectors are very fast and easy to utilize, they have relatively poor energy resolution and sensitivity to elements present in low abundances when compared to wavelength dispersive x-ray detectors (WDS) on most electron probe micro analyzers (EPMA). An electrically conductive coating must be applied to electrically insulating samples for study

in conventional SEM's, unless the instrument is capable of operation in a low vacuum mode [26].Figure 3.9 is a schematic diagram of FE-SEM.

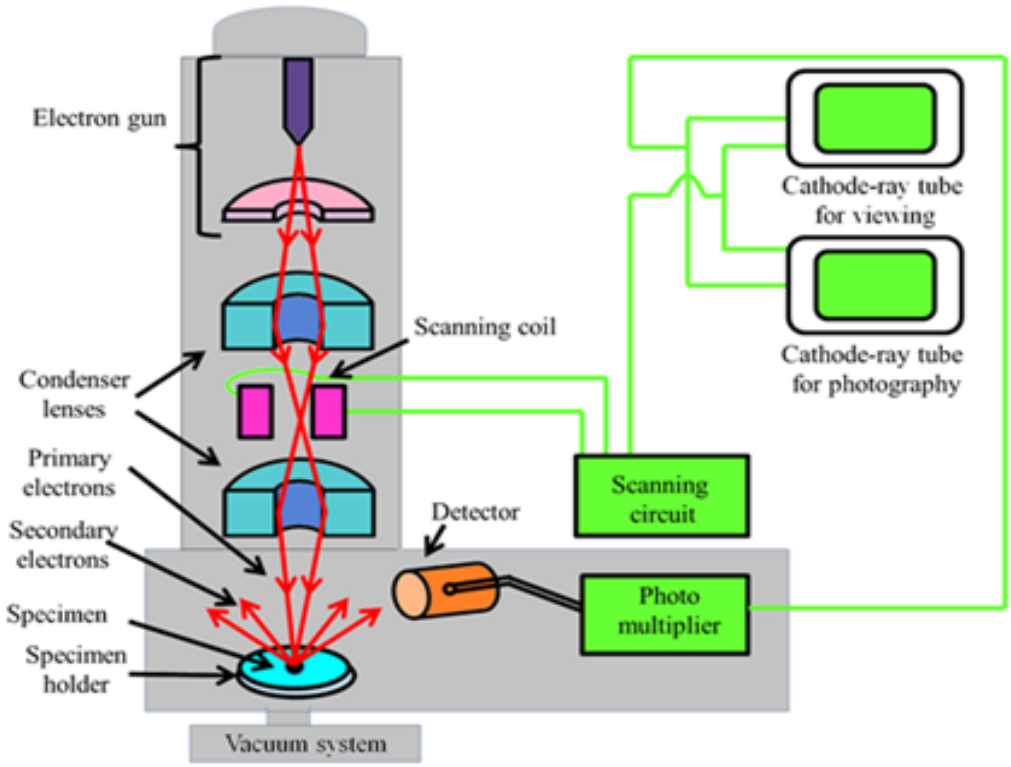

Figure 3.9: Schematic presentation of the field emission scanning electron microscopy [26].

Figure 3.10: A typical SEM instrument, showing the electron column, sample chamber, EDS detector, electronics console, and visual display monitors.

3.7.5. Energy dispersive x-rays spectroscopy

Energy Dispersive X-Ray Spectroscopy (EDS) is a chemical microanalysis technique used in conjunction with scanning electron microscopy (SEM) [27]. The EDS technique detects x-rays emitted from the sample during bombardment by an electron beam to characterize the elemental composition of the analyzed volume. Features or phases as small as 1 μm or less can be analysed [27].

When the sample is bombarded by the SEM's electron beam, electrons are ejected from the atoms comprising the sample's surface [27]. The resulting electron vacancies are filled by electrons from a higher state, and an x-ray is emitted to balance the energy difference between the two electrons' states. The x-ray energy is characteristic of the element from which it was emitted [27].

The EDS x-ray detector measures the relative abundance of emitted x-rays versus their energy. The detector is typically a lithium-drifted silicon, solid-state device. When an incident x-ray strikes the detector, it creates a charge pulse that is proportional to the energy of the x-ray. The charge pulse is converted to a voltage pulse (which remains proportional to the x-ray energy) by a charge-sensitive preamplifier [27]. The signal is then sent to a multichannel analyzer where the pulses are sorted by voltage. The energy, as determined from the voltage measurement, for each incident x-ray is sent to a computer for display and further data evaluation. The spectrum of x-ray energy versus counts is evaluated to determine the elemental composition of the sampled volume [27]. Figure 3.11 is a schematic illustration of x-rays emitted from an atom.

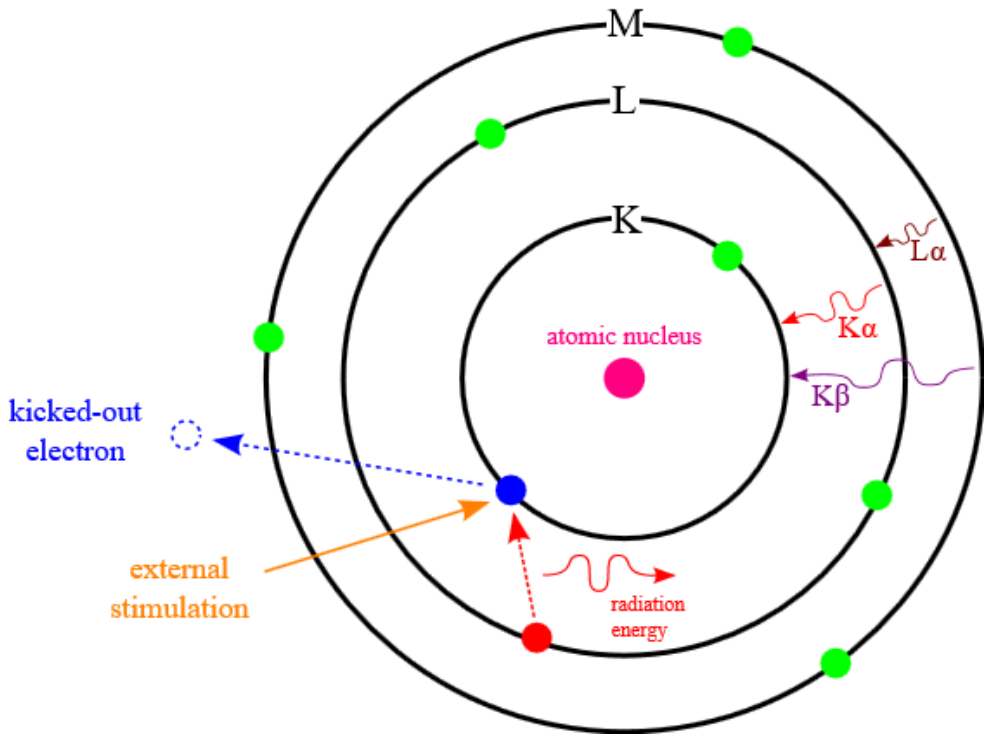

Figure 3.11: Illustration of emitted characteristic x-rays in an atom [27].

3.8. UV-Vis spectrophotometry (UV)

UV-Vis spectrophotometry is a technique that involves absorption and/or reflectance of light (radiation) in the ultraviolet-visible spectral region. It measures the intensity *(I)* of light passing through a sample, and compares it to the original intensity (I_0) of light before it passes through the sample [27]. The ratio I/I_0 is called the transmittance, and is expressed as a percentage (%T). The absorbance (A) is related to the transmittance by the following equation:

$$A = -\log\left(\frac{\%T}{100}\right) \tag{3.4}$$

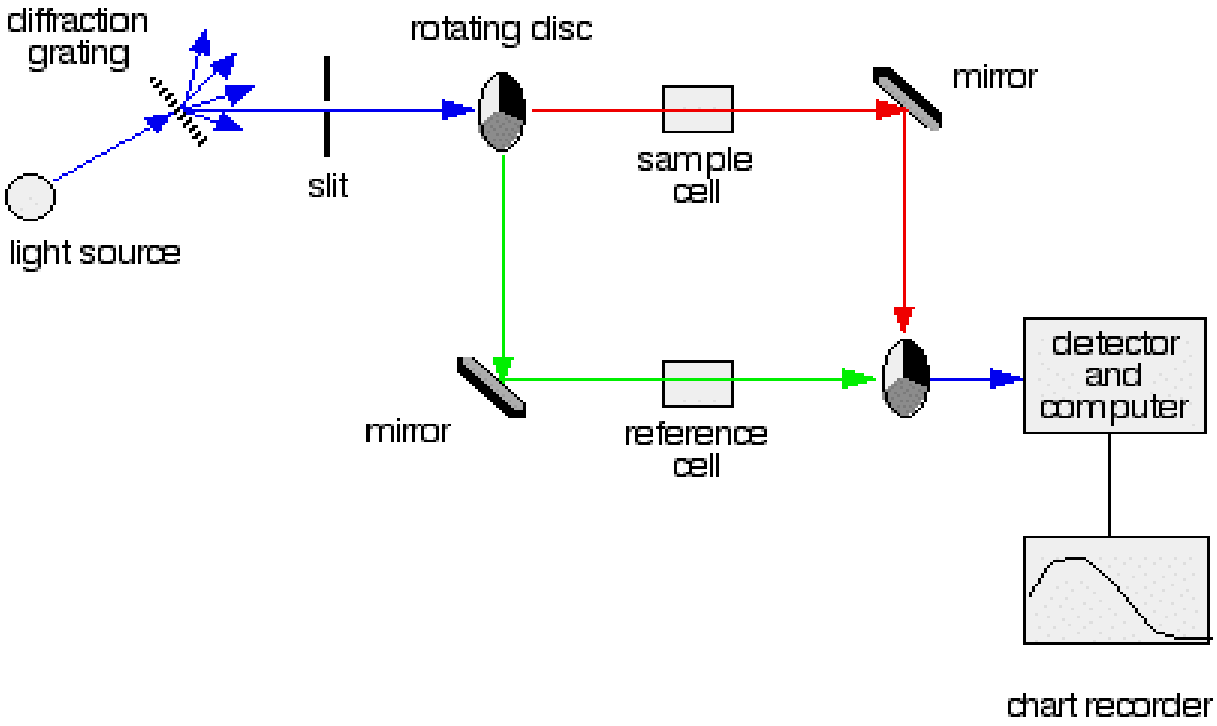

Figure 3.12: Schematic of the UV-Visible spectrophotometer [27].

In UV-Vis spectrophotometry the light beam provided by the light source passes through the diffraction grating and the slits [27]. The radiation is separated according to its frequency wavelength by a diffraction grating followed by a narrow slit. The slit ensures that the radiation is of a narrow waveband that is monochromatic [27]. Detection of the radiation passing through the sample or reference cell can be achieved by either a photomultiplier or a photodiode [27]. Single photodiode detectors and photomultiplier tubes are used with scanning monochromator, which filter the light so that only the light of a single wavelength reaches the detector at one time [27]. The scanning monochromator moves the diffraction grating to step-through each wavelength so that its intensity may be measured as a function of wavelength [27].

Figure 3.12 is a schematic representation of the UV-Vis spectrophotometer, equipped with two source lamps: Deuterium (from about 10 nm to 330 nm) and Tungsten lamps (300 nm to wavelength greater than 3000 nm) [28]. The lamps are used to irradiate the sample, with the Deuterium used from 200 nm up to 319 and then shift to Tungsten up to 1000 nm. Upon irradiating of the sample, the source beam is split into two beams. One beam is directed to the sample and the other is sent to the detector as a reference [28].

The sample is positioned inside an integrating sphere that collects the diffusely scattered light by the sample. Some of the incident light is absorbed by the sample [28]. The collected light eventually falls onto the detector, which subtracts the collected light from the source light to determine the amount that has been absorbed [28]. The detectors used in this system are the PbS and PMT measuring the near infrared region, and Ultraviolet and visible region, respectively. This technique allows determination of the absorbance characteristics of materials [28].

The absorption data from the UV-Vis spectrophotometer in this context was used to determine the band gap energy (E_g) of the material [28]. The band gap energy is determined by using Tauc's relation. The band gap indicates the difference in energy between the top of the valence band filled with electrons and the bottom of the conduction band devoid of electrons [28]. The following relational expression proposed by Tauc, Davis, and Mott is used.

$$(h\nu\alpha) = A\left(h\nu - E_g\right)^{\frac{1}{n}} \tag{3.5}$$

where h: Planck's constant, ν: frequency of vibration, α: absorption coefficient, A: proportional constant, and E_g band gap energy. The value of the exponent n denotes the nature of the sample transition [28].

For direct allowed transition n= $\frac{1}{2}$

For direct forbidden transition n = $\frac{3}{2}$

For indirect allowed transition n = 2

For indirect forbidden transition n = 3

Since the materials analyzed in this study have an indirect allowed transition, n= 2 was used. When $(h\nu\alpha)^{\frac{1}{n}} = 0$, this means that

$$E_g = h\upsilon \tag{3.6}$$

E_g is estimated by extrapolating a tangent line through the plot of $(h\upsilon\alpha)^{\frac{1}{n}}$ against $h\upsilon$. Figure 3.13 below shows the Perkin Elmer Lambda 950 UV-VIS spectrometer used during the absorption measurements [28].

Figure 3.13: Perkin Elmer Lamb 950 UV-VIS Spectrometer

3.9 Photoluminescence spectroscopy

3.9.1 Photoluminescence

Photoluminescence can be described as an excitation of valence band electrons to a higher energy state which is the conduction band and then a return to lower energy state valence band accompanied by the emission of a photon [29]. The period between absorption and emission is typically extremely short, in order of 10 nanoseconds. The optical emission associated with photoluminescence is generally divided into two types: intrinsic and extrinsic.

The shape of the emission spectrum is affected by the thermal distribution of the electrons and holes within their bands [29]. The photoluminescence emission in materials, i.e. in inorganic insulators and semiconductors is classified in terms of the nature of the electronic transitions producing it is either intrinsic or extrinsic photoluminescence. In this study the classification of the electronic transitions in photoluminescence are due to intrinsic luminescence effects the nature of this effect is discussed in the below sections [29].

3.9.2 Intrinsic photoluminescence

Intrinsic photoluminescence is a kind of luminescence that may arise due to the presence of a variety of defects in a crystal structure. This type of luminescence does not involve impurity atoms. There are three kinds of intrinsic photoluminescence namely: band to band, excitons and cross luminescence. In general there are several factors that may influence intrinsic photoluminescence such as: Non stoichiometry - a state of a material (semiconductor) not having exactly the correct elemental proportion. Structural imperfections – owing to poor ordering, radiation damage, or shock damage [29].

3.9.3 Photoluminescence: Helium-Cadmium laser

The Helium-Cadmium (He-Cd) laser is one of a range of gas lasers using helium in conjunction with a metal which vaporizes at a relatively low temperature. A typical construction for the He-Cd laser is in the form of a tube, terminated by two Brewster's angle windows, with two laser mirrors mounted separately from the tube [30]. The tube filled with helium also has a reservoir containing the Cd and a heater to vaporize the metal. The reservoir is raised to a high enough temperature (~ 250 ^{o}C) to produce the desired vapour of Cd atoms in the tube. He-Cd lasers can give output powers of 50-100 mW and it can produce a high quality beam at 442 nm (violet-blue) and/or 325 nm (UV) depending on the optics. In this study a 325 nm He-Cd laser was used to investigate the photoluminescent properties of the phosphors [30].

The monochromator consists of diffraction gratings which serve as an engine of the entire optical measurement system and it is used to differentiate between emissions at different photon wavelengths. Eventually, the light from the sample is sent to the detector:
photomultiplier tube (PMT) in the visible region [30]. Figure 3.14 depicts a schematic diagram of PL system with He-Cd laser of a fixed excitation wavelength of 325 nm.

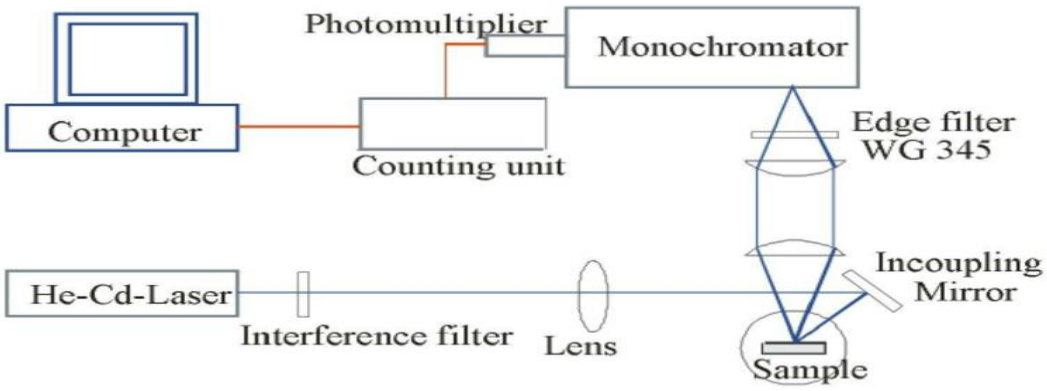

Figure 3.14 : Schematic diagram of the PL system with He-Cd laser with a fixed wavelength of 325 nm [30].

Figure 3.15 : A typical PL laser system with an excitation wavelength of 325 nm.

References:

[1] Patil K.C., Mimani T.: Solution combustion synthesis of nanoscale oxides and their composites Mater. Phys. Mech. 4, 134–137 (2001)

[2] Kopp A. Alves et al., *Novel Synthesis and Characterization of Nanostructured Materials*,Engineering Materials, DOI: 10.1007/978-3-642-41275-2_2.

[3] Hwang C.C. , Wu T.Y, *Journal of material science*, 2004, 39, 6111-6115.

[4] Aruna S.T., Mukasyan A.S., Current Opinion in Solid State and Materials Science 12 (2008) 44–50

[5] Zhang Y., H. C. Shin H.C., Dong J., Liu M., *Solid State Ionics*. 171(2004)25-31

[6] http://shodhganga.inflibnet.ac.in/bitstream/10603/5252/9/09_chapter%202.pdf/ [accessed October 2016]

[7]http://www.hyperphysics.phy-astr.gsu.edu/hbase/phyopt/diffracon.html [Accessed October 2016]

[8] http://www.olympusmicro.com/primer/lightandcolor/diffraction.html/ [Accessed October 2016]

[9] http://www.launc.tased.edu.au/online/sciences/physics/diffrac.html/ [Accessed October 2016]

[10] http://serc.carleton.edu/research_education/geochemsheets/techniques/XRD.html [Accessed October 2016]

[11] http://pdx.edu/~pmoeck/phy381/Topic5a-XRD.pdf [Accessed October 2016]

[12] http://en.wikipedia.org/wiki/Bragg's_law/ [Accessed October 2016]

[13] http://www.eserc.stonybrook.edu/ProjectJava/Bragg/ [Accessed October 2016]

[14] www.eserc.stonybrook.edu/ProjectJava/Bragg/ [Accessed October 2016]

[15] https://www.bruker.com/.../x-ray-diffraction-and.../x-ray-diffraction.htm...[Accessed November 2016]

[16] Pulker H., Paesold G., Ritter E.: Appl. Opt. 15, 2986 (1976).

[17] Rodriguez L., Matoušek J.: Ceramics-Silikáty 47, 28 (2003).

[18] http://en.wikipedia.org/wiki/X-ray_photoelectron_spectroscopy/ [accessed February 2016]

[19] Sezen H., Suzer S., *Thin Solid Films*, 534 (2013), 1-11

[20] http://www.phi.com/surface-analysis-products/versaprobe/overview.html/ [accessed November 2016]

[21] http://www.wcaslab.com/tech/tech2.htm [Accessed November 2016]

[22] http://www.wcaslab.com/tech/tech2.htm [Accessed November 2016]

[23] http://www.hk-phy.org/atomic_world/tem/tem02_e.html [accessed October 2016]

[24] http://le-csss.asu.edu/ARM200F [accessed October 2016]

[25] http://serc.carleton.edu/research_education/geochemsheets/techniques/SEM.html [Accessed October 2016]

[26] http://www.nanoscience.com/products/sem/technology-overview/ [Accessed October 2016]

[27] http://www.mee-inc.com/hamm/energy-dispersive-x-ray-spectroscopyeds/ [Accessed October 2016]

[28] Blasse G., Grabmair B.C., Luminescent materials, Springer-Verlag,(1994)

[29] Gilliland G.D., *Mate. Sci. Eng*, 1997, R18, 99-400

[30] Lephoto M.A., Ntwaeaborwa O.M., Mothudi B.M, Swart H.C., Luminescent properties of combustion synthesized $BaAl_2O_4:Eu^{2+}$ and $(Ba_{1-x}Sr_x)Al_2O_4:Eu^{2+}$ phosphor co-doped with different rare earth ions, MSc Thesis, (2011), University of the Free State, Bloemfontein, South Africa.

Chapter 4: Luminescent properties of ZnO phosphor powders prepared by solution combustion method

4.1. Introduction

Nanosized particles of semiconductors materials have gained much more interest in recent years due to their desirable properties and applications in different areas such as catalysts [1], sensors [2], photoelectron devices [3,4] which are highly functional and effective devices [5]. These nanomaterials have novel electronic, structural and thermal properties which are of high scientific interest in basic and applied fields [5].

Zinc oxide (ZnO) is one of the most widely used wide-band gap semiconducting phosphor materials, which show excellent luminescent properties under either high energy electron beam or ultraviolet (UV) photon excitation. It has a bulk band gap of 3.37 eV and large exciton binding energy of 60 meV at room temperature. ZnO is also known for its high chemical stability and n-type conductivity [6-9].

ZnO has unique physical and chemical properties such as high chemical stability, high electrochemical coupling coefficient, broad range of radiation absorption and high photostability that makes it a versatile multifunctional material [10,11]. In material science ZnO is classified as a semiconductor in group II-VI whose covalence is on the boundary between ionic and covalent semiconductors [12,13].

The piezo and pyroelectric properties of ZnO suggest that it can be used as a sensor, converter, energy generator and photocatalyst in hydrogen production. [13,14]. The hardness of ZnO is 4.5 and of a diamond is 10 on the Mohs scale, Its rigidity is 0.15 eV, which is much smaller than that of graphite which is 1.17 eV. The piezoelectric constant is size-dependent (the smaller the particles the larger the piezoelectric constant) but that of bulk ZnO is 9.93 pm/V. These characteristics make ZnO an important material in the ceramics industry while its low toxicity

and biocompatibility make it a material of interest for biomedicine and in pro-ecological systems [15-18].

In addition, ZnO is a well suited semiconductor material with a variety of applications in the development of UV optoelectronics because of its large excitation binding energy and versatile band gap [19]

ZnO nanomaterials have received considerable attention for applications in short-wavelength light emitters, field emitters, luminescence devices, ultraviolet (UV) laser technology [20], solar cells [21], photocatalysts [22] and superhydrophobic materials [23-26].

Most forms of undoped ZnO at room temperature show n-type character. The question is the origin of this n-type character and the associated donor states, which are mostly centred around two doubly occupied contenders, namely the oxygen vacancy (V_O) states and interstitial Zn (Zn_i) related defects [27]. Understanding the origin of these defects is vital not for not only tailoring ZnO for varied applications but also to gain a basic insight into the physics of doping ZnO. The current understanding about the likely origin of the n-type nature of ZnO is as follows: complexes of the deep level (V_O) and the shallower (Zn_i) states formed by their hybridization may be responsible for the formation of effective donor states, rather than the isolated (Zn_i) and (V_O) defect states themselves [27]. However, these hybridized states may be effective donors only if they energetically lay either close to the conduction band (CB) minima, with ionization energies comparable to room temperature or within the conduction band themselves [27].

The exciton recombination is the primary channel of photoluminescence (PL) in ZnO, where the exciton binding energy is larger than the thermal energy. Electrons excited into the conduction band (CB) from the valence band (VB) undergo relaxation to the conduction band minimum (CBM), which if followed by radiative electron-hole (e-h) recombination result in the detected PL emission [27]. The momentum and energy relaxation path to the CBM is thus strongly correlated to the band structure of the system.

The typical PL emission spectrum of ZnO shows the characteristic near-band-edge (NBE) emission in the UV, along with green-orange emission in the visible range. Due to intrinsic defect state present within the band gap [27]. The related states lying below the CBM have been shown to give rise to violet-blue emissions that are seldom detected in the PL spectra of ZnO, except in Zn rich conditions and for excitation energies close to, or just less than, the band-gap energy (Eg). The green-orange emissions have been attributed to transitions to and from ionized Vo states, which effectively manifest at surfaces interfaces and grain boundaries [27].

This chapter reports on the preparation, structure, morphology, reflectance and hence absorption behaviour, bandgap and photoluminescence properties of the solution combustion synthesized ZnO. Solution combustion synthesis involves the redox reaction between an oxidising reagent that usually comprises of desired metal salts and reducing reagent - (organic compound acting as fuel) [28]. Previous studies used various fuels such as urea, glycine and citric acid to produce ZnO nanoparticles using solution combustion synthesis method resulting

in various particle morphologies, and luminescent properties [28,29], among other things. Various particle morphology of ZnO nanoparticles makes them suitable for different applications. For example, ZnO nanoparticles with high surface area enhance photocatalytic ability in the visible light region.

The un-doped ZnO samples were prepared using solution combustion method at 600 ˚C and 700 ˚C using urea as a fuel.

4.2. Experimental

4.2.1 Preparation of ZnO

Zinc nitrate tetrahydrate and urea were used as starting materials. The materials were mixed stiochiometrically according to the following reaction equation:

$$3Zn(NO_3)_2\,(H_2O)_4 + 5CH_4N_2O \rightarrow 3ZnO + 22H_2O + 5CO_2\uparrow + 8N_2\uparrow \qquad (4.1)$$

In a typical synthesis preparation, 0.2 g urea, 0.5225 g of zinc nitrate tetrahydrate and 2 mL of deionized water were mixed together and stirred for 60 minutes at approximately 80˚C to achieve a homogenous solution. The solution, in a crucible, was transferred to a furnace which was pre-set to a temperature of either 600 ˚C and 700 ˚C ± 15, for 15 minutes. During the solution combustion reaction water evaporated, N_2 and CO_2 gases were liberated and an orange ZnO powder was formed. As previously discussed in chapter 3 urea acts as a good complexing agent for metal ions because of two reasons: it contains two amino groups located at the extremes of its chemical structure and it is water soluble so ZnO doping by urea (nitrogen) for these reasons is highly unlikely. No flame was observed during the combustion reaction and this could be due to the fact that the precusors did not react exothermically by themselves so excess energy in the form of heat was required for the synthesis reaction to occur. The schematic illustration of the synthesis procedure is presented in figure 4.1.

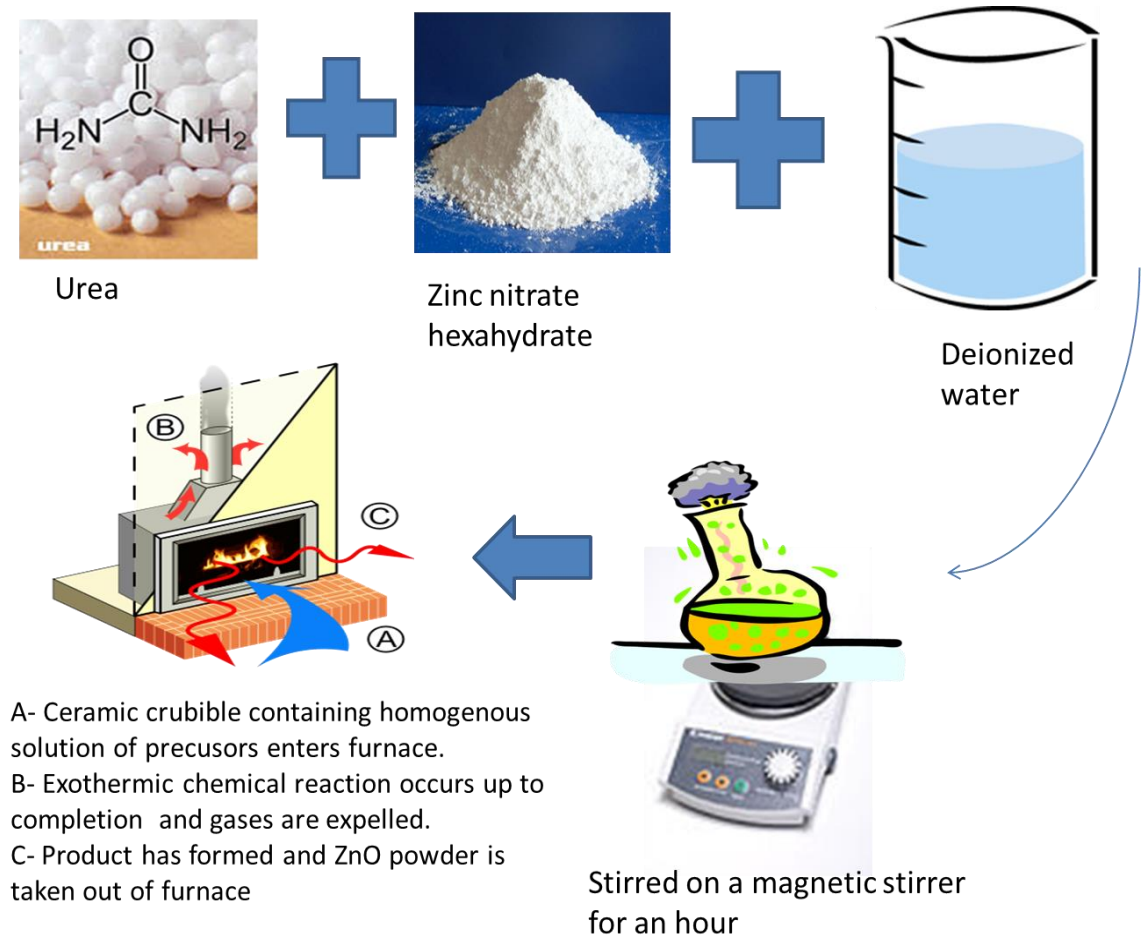

Figure 4.1: Graphical representation for preparation of ZnO using solution combustion synthesis method.

4.2.2. Characterization

The structural properties of the ZnO powder were analysed using a Bruker D8 Advance powder diffractometer with a Cu-Kα radiation wavelength of 1.54 Å. The particle morphology and elemental composition of the materials was analysed using Jeol JSM-7800F field emission scanning electron microscope (FE-SEM) coupled with energy dispersive spectrometer (EDS). Particle morphology and crystalline structure were further examined using JEOL ARM200F HR-TEM. The photoluminescence data was recorded at room temperature using a He-Cd laser at an excitation wavelength of 325 nm.

4.3. Results and Discussion

4.3.1. Structural Studies

4.3.2. XRD Results

Figure 4.2 shows the XRD pattern of the as-prepared ZnO powder synthesized at 600˚C and 700˚C. These XRD patterns are consistent with the standard hexagonal structure of ZnO referenced in JCPDS Card Number 89-1397. The diffraction patterns become sharper and more intense when the synthesis temperature was increased from 600˚C to 700˚C indicating improvement of crystallinity and an increase in crystallite sizes from 23.3 nm to 30.06nm confirmed by the Scherrer equation

$$D = \frac{K\lambda}{\beta \cos\theta} \qquad (4.2)$$

where D is the mean size of the ordered (crystalline) domains, which may be smaller or equal to the grain size. K is a dimensionless shape factor, with a value close to unity. The shape factor has a typical value of about 0.9 but varies with the actual shape of the crystallite. λ is the X-ray wavelength; β is the line broadening at half the maximum intensity (FWHM), after subtracting the instrumental line broadening, in radians, this quantity is also sometimes denoted as $\Delta(2\theta)$ and θ is the Bragg angle [30].

As shown in tables 4.1 and 4.2, all the diffraction peaks were used to calculate the crystallite size then the average value was taken.

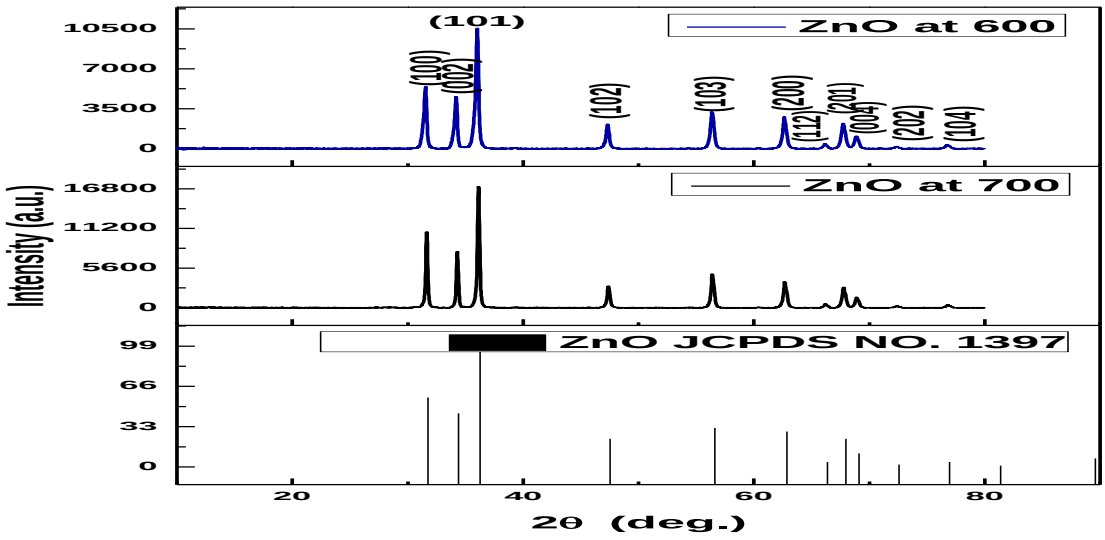

Figure 4.2: XRD patterns of as-prepared un-doped ZnO synthesized at 600 ˚C and 700 ˚C powders and matching JCPDS Card No 89-1397 .

Table 4.1: Calculation of crystallite size for the as-prepared ZnO sample synthesized at 600˚C.

Planes (hkl)	Peak position	2θ	θ	β(deg)	β (rad)	D
100	1	31.515	15.758	0.344	0.00642	24.0
002	2	34.170	17.085	0.323	0.00685	25.7
101	3	36.010	18.005	0.339	0.00621	24.6
102	4	47.320	23.660	0.342	0.00600	25.4
110	5	56.390	28.195	0.391	0.00711	23.060
103	6	62.660	31.330	0.417	0.00858	19.7
200	7	66.179	33.090	33.090	0.00736	25.02
112	8	67.760	33.880	33.880	0.00814	21.5
201	9	68.900	34.450	34.450	0.00869	21.5
004	10	76.790	38.395	38.395	0.00877	22.9
					Average=	23.3

Table 4.2: Calculation of crystallite size for the as-prepared ZnO sample synthesized at 700˚C.

Planes (hkl)	Peak position	2θ	θ	β (deg)	β (rad)	D
100	1	31.650	15.825	0.215	0.00447	38.4
002	2	34.310	17.155	0.213	0.00411	39.010
101	3	31.140	15.570	0.240	0.00435	34.3
102	4	47.400	23.700	0.301	0.00549	28.8
110	5	56.420	28.210	0.335	0.00647	26.9
103	6	62.700	31.350	0.379	0.00723	24.6
200	7	67.800	33.900	0.395	0.00746	24.2
112	8	68.930	34.465	0.398	0.00790	24.2
					Average=	30.06

4.3.3. SEM and EDS results

Scanning electron microscopy (SEM) analysis was performed to evaluate the fine-scaled topographical features of the samples. SEM micrographs at different magnifications for the as-prepared ZnO sample synthesized at 600˚C are depicted in figure 4.5 (a-d).

We observe morphology that consists of coalescence (attachment of particles) and agglomeration. The coalescence of smaller particles similar in shape and size is observed as triangular-shaped particles attaching and forming flower/bud-like structures. In the case of intraparticle diffusion, particles which are different in shape and size attach and form larger triangular incrusted with smaller spherical particle structures. This is what is observed in figure 4.5. (a-d), flower/bud like shaped particles attach to smaller spherical shapes in order to form

triangular and incrusted with smaller spherical particles. Also tiny black holes are observed on the flower/bud like shaped particles that eventually form triangular particles, this is due to the outgassing of nitrogen and oxygen present in solution combustion method. The proposed mechanism of nucleation and growth is shown in figure 4.4.

The EDS spectrum of the as-prepared ZnO sample is shown in figure 4.6. In this EDS spectra all elements present in the sample were observed, the carbon peak can be attributed to the carbon tape on which the sample was mounted. The weight percentage of the elements present in the sample observed on the surface are as follows: for zinc it's 73.45%, oxygen it's 16.53% and lastly for carbon it's 10%. This is in good correlation with respect to what is expected for the calculated theoretical values for zinc (75.43%) and O (19.65%) .

4.3.3.1. Mechanism of formation and crystal structure of ZnO:

There are many mechanisms of nucleation and growth in solution. Nucleation is the process whereby nuclei (seeds) act as templates for crystal growth. This can be used to describe the nucleation of many chemical syntheses. However, the formation of porous solids does not always follow the classical pathways of crystallization in solution [32]. Homogeneous nucleation occurs when nuclei form uniformly throughout the parent phase, whereas, heterogeneous nucleation forms at structural inhomogeneities (container surfaces, impurities, grain boundaries, dislocations). In liquid phase, heterogeneous nucleation occurs much easier, since a stable nucleating surface is already present this is what was observed in this study.

A single rapid nucleation would favour particle growth with uniform size and shape, whereas in the case of a slower nucleation rate, reactants are unevenly depleted from solution leading to variations in the growth rate for seeds formed at different reaction stages [32]. This is observed in this study with particles having different shapes, sizes and hence different structures (joint shapes).

The first step in the proposed mechanism of nucleation and growth is the LaMer mechanism which is illustrated in a graph in figure 4.3. The conceptual separation of nucleation and growth is divided into two stages: Stage (I) involves a rapid increase in the concentration of free particles in solution while stage (II) the particles undergoes "burst nucleation" which significantly reduces the concentration of free particles in solution. The rate of this nucleation is described as "effectively infinite" and after this point (III) there is almost no nucleation occurring due to the low concentration of particles. Following nucleation, growth occurs under the control of the diffusion of the particles through the solution [32].

In the second step of the proposed nucleation and growth mechanism two possible processes take place simultaneous. Nanoparticles (NPs) follow either Oswald ripening or Digestive ripening nucleation and growth route, depending on the surface energy of the particles within the solution [32].

Ostwald ripening, the second step in the proposed mechanism of growth is caused by the change in solubility of NPs dependent on their size. Due to the high solubility and the surface energy of smaller particles within solution, smaller particles re-dissolve and in turn allow larger particles to grow even more [32]. Digestive ripening is effectively the inverse of Ostwald ripening. Within this case, smaller particles grow at the expense of the larger ones. This process of formation is controlled once again by the surface energy of the particle within solution where the larger particle re-dissolves and in turn smaller particles grow [32].

The final stage in the proposed growth mechanism is intraparticle ripening, this is the diffusion of NPs along the surface to change the shape of the particle with time. This means that the surface energy of the particle is almost equal to the bulk solution, and in this case there would be no net diffusion [32]. In this case the high energy facets dissolve and the low one will grow leading to an apparent intraparticle diffusion [32].

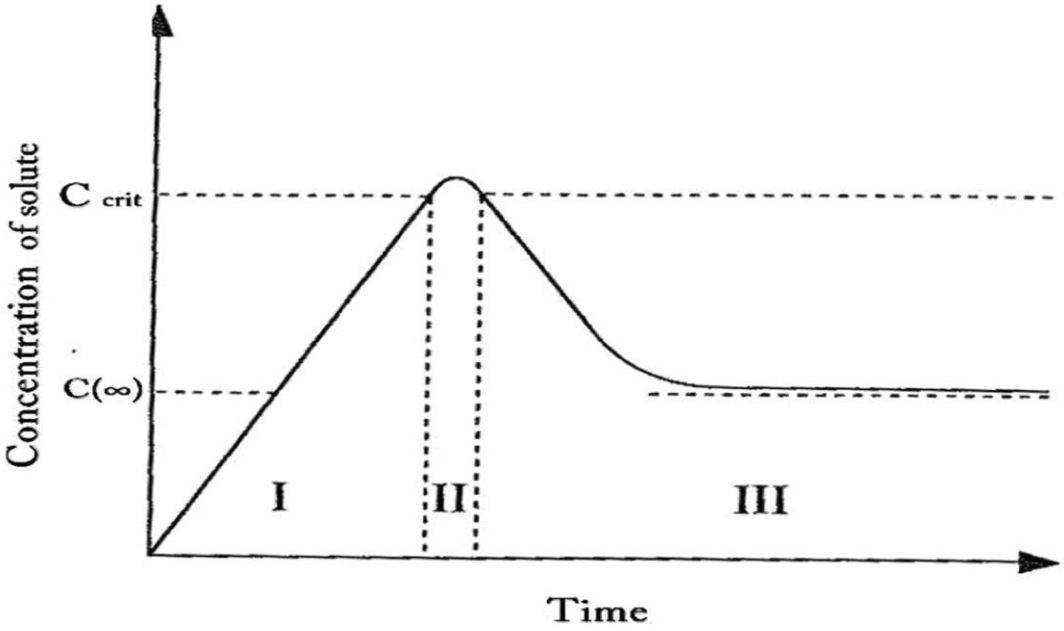

Figure 4.3: LaMer diagram illustrating LaMer nucleation and growth mechanism.

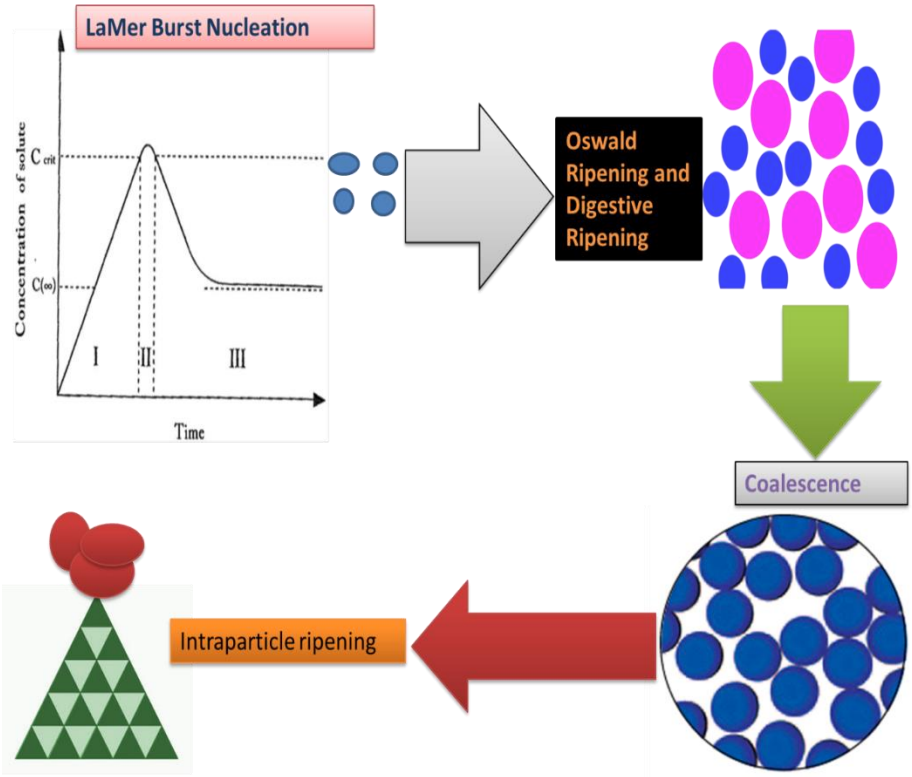

Figure 4.4: Mechanism of nucleation and growth in ZnO nanoparticles.

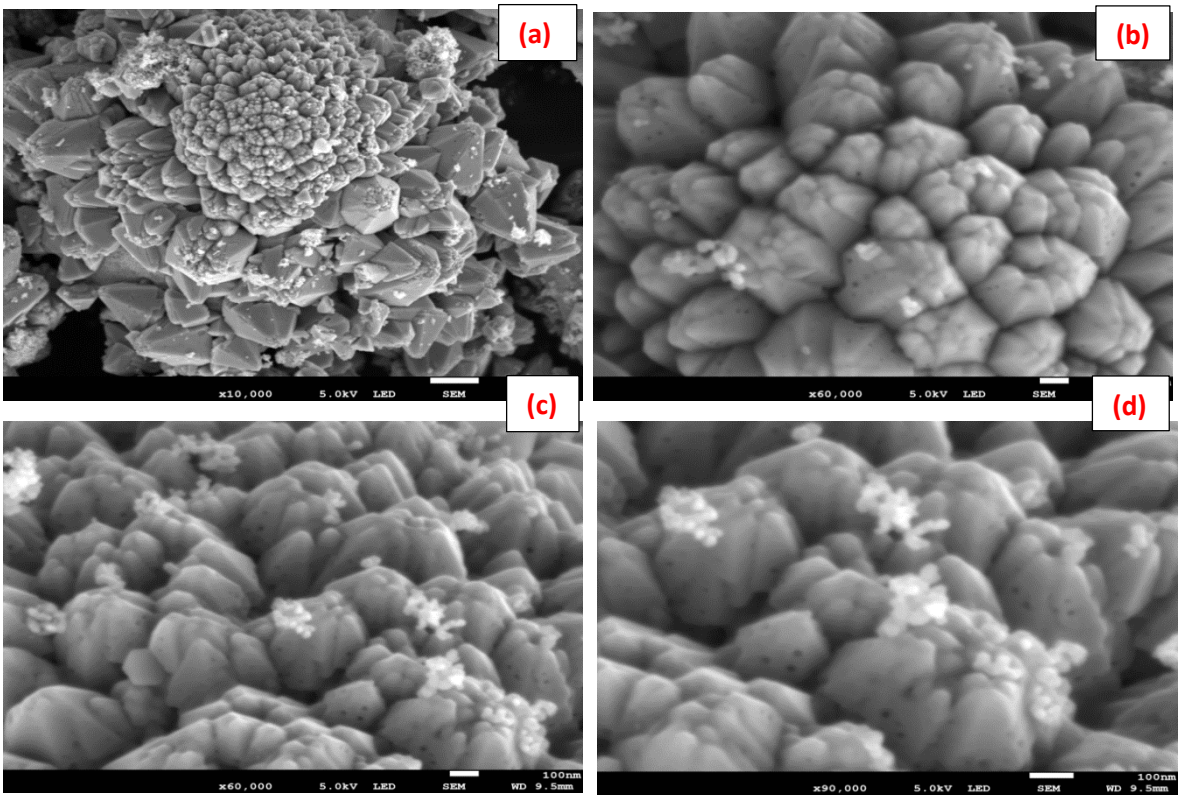

Figure 4.5 (a-d): shows the SEM images of as-prepared un-doped ZnO .

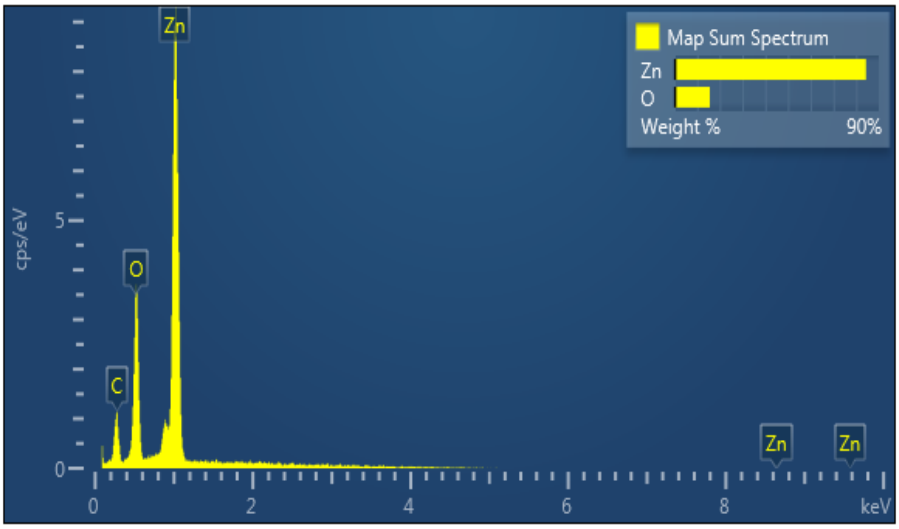

Figure 4.6 : The EDS spectra of as-prepared un-doped ZnO.

4.3.4. HR-TEM results

Figure 4.8 illustrates the HR-TEM micrographs of ZnO NPs obtained from solution combustion synthesis at a synthesis temperature of 600˚C. The HR-TEM images show that the ZnO NPs are hexagonally shaped and aggregated into clusters. At high synthesis temperatures such as 600˚C many neighbouring particles are prone to fuse together to form larger particles. The average size of the synthesized ZnO nanoparticles obtained from the Scherrer's formula is 23 nm and from HR-TEM micrographs is 28.8 nm. The average particle size was calculated by measuring the diameter of all the observable particles, obtaining the average and calculating the radius. The XRD and HR-TEM particle are in good correlation with each other.

The d-spacing of lattice planes (d_{hkl}) can be determined using Bragg's formula:

$$d_{hkl} = \frac{n\lambda}{2\sin\theta} \tag{4.3}$$

For a hexagonal crystal structure (such as ZnO) the interplanar spacing are given by the following equation:

$$\frac{1}{d^2} = \frac{4}{3}\left(\frac{h^2+hk+k^2}{a^2}\right) + \frac{l^2}{c^2} \tag{4.4}$$

The geometry of the electron diffraction experiment is shown in figure 4.3. The distance *R* of a diffraction spot from the direct beam spot on the diffraction pattern varies inversely with the planes *d* that generate the spot [31] .

Bragg's law for small angle approximation is denoted by:

$$\lambda = 2d\theta \tag{4.5}$$

From the diagram, again for small angles,

$$\frac{R}{L} = 2\theta \tag{4.6}$$

Therefore

$$\frac{R}{L} = \frac{\lambda}{d} \text{ or } R = \lambda L \times \frac{1}{d} \tag{4.7}$$

Many microscopes capture diffraction patterns with a scale bar of inverse length. They simply take $\lambda L = 1$ so that $R = 1/d$ and the inverse interplanar spacing can be measured using the marker directly on the image.

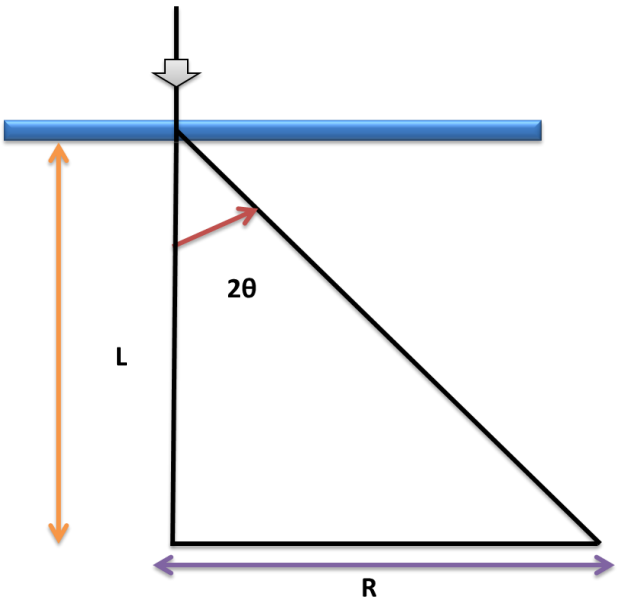

Figure 4.7: Illustration of electron diffraction with respect to HR-TEM micrographs.

Table 4.3 represents the calculations of the distance *R* of a diffraction spot from the direct beam spot using equation (4.7) where $\lambda L = 1$. With regards to the data from the Table 4.3: a PDF (80-0075) x-ray file for ZnO was obatained and from it the expected d-spacings were calculated. Then the value 1/d (converted to nm first) was calculated as to obtain the expected ring radii. Using the scale bar on the SAED image, rings were plotted with diameters double these radii, centres and the rings. The match for ZnO was good despite there being few spots. From this, it can be deduced that the XRD and SAED results for the ZnO sample are in good correspondence.

Table 4.3: Illustrations of calculation of ring diameters for ZnO.

ZnO Hkl	d(A)	R(nm^{-1})	2R(nm^{-1})
100	2.8179	3.55	7.10
002	2.6049	3.84	7.68
101	2.4786	4.03	8.07
102	1.9128	5.23	10.46
110	1.6269	6.15	12.29
103	1.4784	6.76	13.53
200	1.4089	7.10	14.20
112	1.3799	7.25	14.49
201	1.3601	7.35	14.70
004	1.3024	7.68	15.36
202	1.2393	8.07	16.14
104	1.1822	8.46	16.92
203	1.0941	9.14	18.28

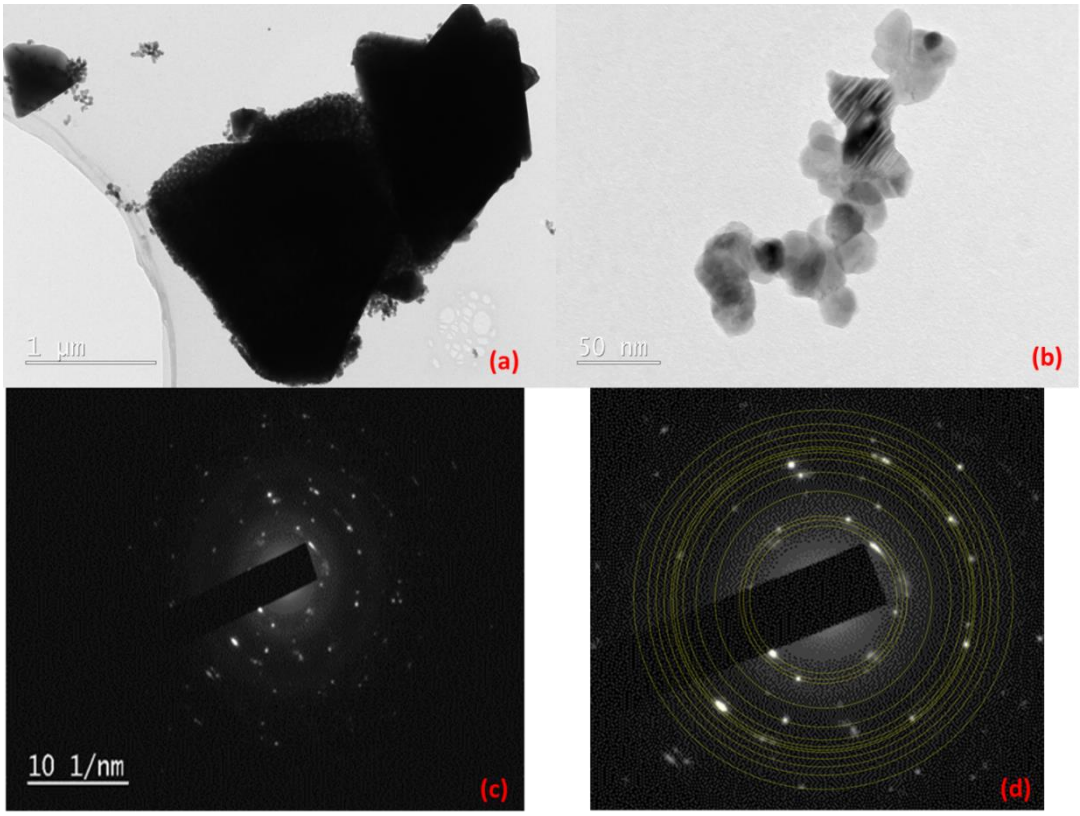

Figure 4.8 (a-d): HR-TEM micrographs (a-b) and SAED pattern (c and d) of as-prepared undoped ZnO synthesized at 600˚C.

4.4 Optical studies results:

4.4.1. Photoluminescence results:

Figure 4.9 (a) are the photoluminescence spectra of ZnO nanoparticles synthesized at 600 ˚C and 700 ˚C. The excitation used was from the He-Cd laser source with the wavelength of 325 nm. The PL spectrum exhibits the UV near band to band emission (BBE) and deep level emission (DLE) [33]. The narrow peak in the UV region in both samples was at 380 nm and is associated with recombination of free excitons. The broad peaks in the visible region at 639 nm for ZnO synthesized at 600˚C and 626 nm for ZnO synthesized at 700˚C are attributed to electron mediated defect levels in the bandgap. There is a peak shift in these two samples to the blue region, this is due to increase of defect density in the bandgap when the synthesis temperature was increased to 700˚C.

The PL intensity of the BBE peak has increased with an increase in the synthesis temperature from 600 ˚C to 700 ˚C due to an improvement in the crystallinity and concentration of surface states. The DLE has decreased with an increase in the synthesis temperature from 600 ˚C to 700 ˚C.

The DLE peak is due to the defect levels in the bandgap of ZnO. Generally ZnO has six kinds of defects such as oxygen vacancies (Vo), oxygen interstitials (O_i), oxygen antisites (ZnO), zinc vacancies (V_{Zn}), zinc interstitials (Zn_i) and zinc antisites (O_{Zn}) [33]. The intensities of different kind of defects are attributed to different kind of colour emission from ZnO [33].

Figure 4.9 (b) shows that decovoluted PL spectrum for the ZnO sample prepared at 600˚C. There are 3 peaks at ~ 583, 645 and 720 nm. The yellow band near 583 nm (2.1 eV) is associated with deep level transitions from the CB to O_i or Zn_i to Oi [34]. The electronic transitions from O_i to the VB and from Zn_i to O_i are both possible origins of the emission peaks at 645 nm and 720 nm [34].

Figure 4.9 (c) illustrates the deconvoluted peaks of the 626 nm broad emission peak of the ZnO sample synthesized at 700˚C. The peaks are at ~ 565, 626 and 697 nm. As discussed above there is a peak shift to the blue region of the broad peak of 639 nm to 626 nm, with an increase in synthesis temperature from 600˚C to 700˚C. Therefore there would also be a shift to the blue region resulting in the following peaks approximately at 565, 626 and 697 nm as well. The green emission at 565 nm is associated with the transition from CB to V_o^{+2}- Zn_i^{-2} band [34].

The electronic transitions from O_i to the VB and from Zn_i to O_i are both possible origins of the emission peaks at 626 nm and 697 nm [34].

Since different luminescent behaviour and electronic transitions are observed with increase on synthesis temperatures with the samples, figure 4.10. (a) and (b) are the proposed mechanisms of electron transitions for the ZnO samples prepared at 600˚C and 700˚C. These transitions on the energy diagrams have been explained above.

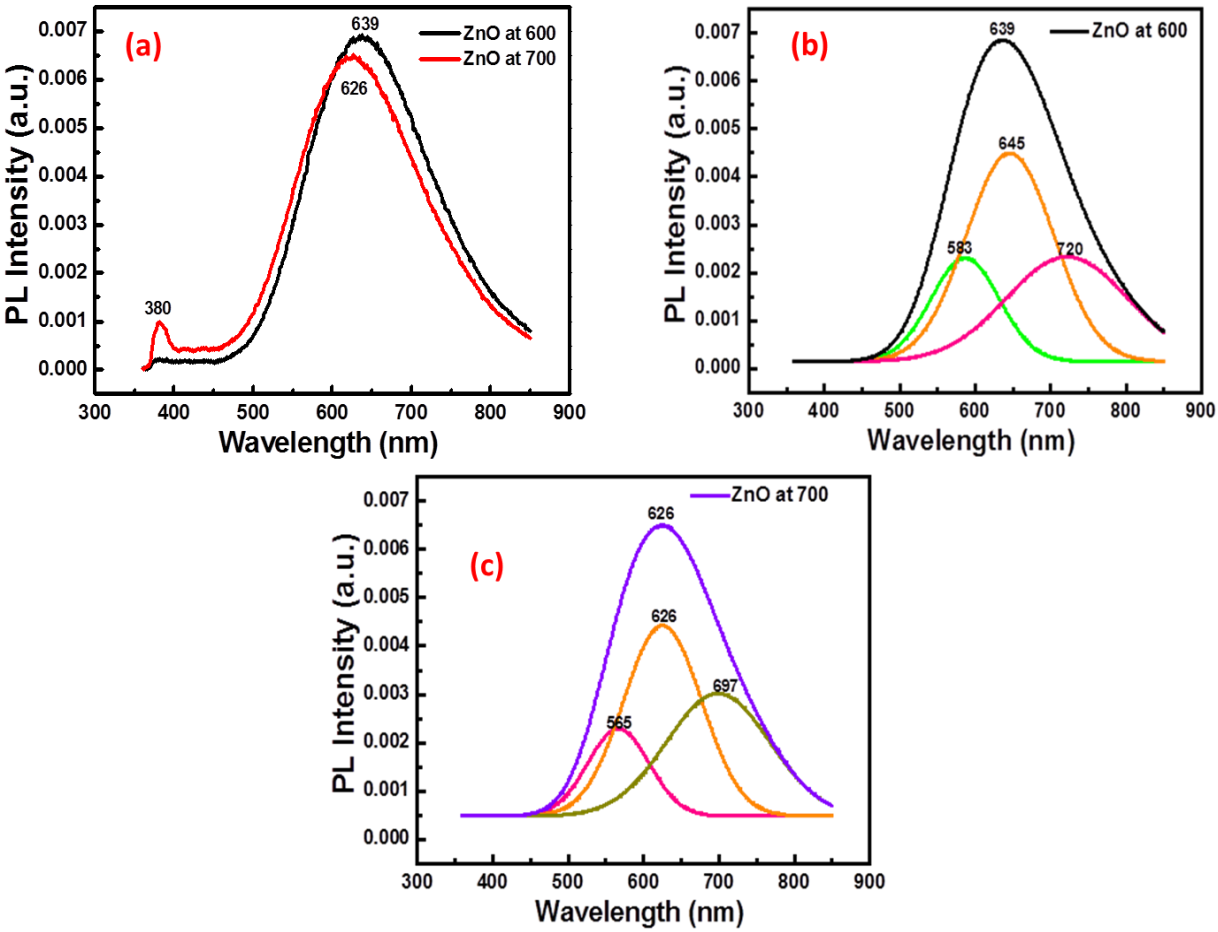

Figure 4.9. (a-b): Photoluminescence spectra of as-prepared un-doped ZnO sample synthesized at 600˚C, it's deconvoluted spectra and the deconvoluted spectra of the sample synthesized at 700˚C.

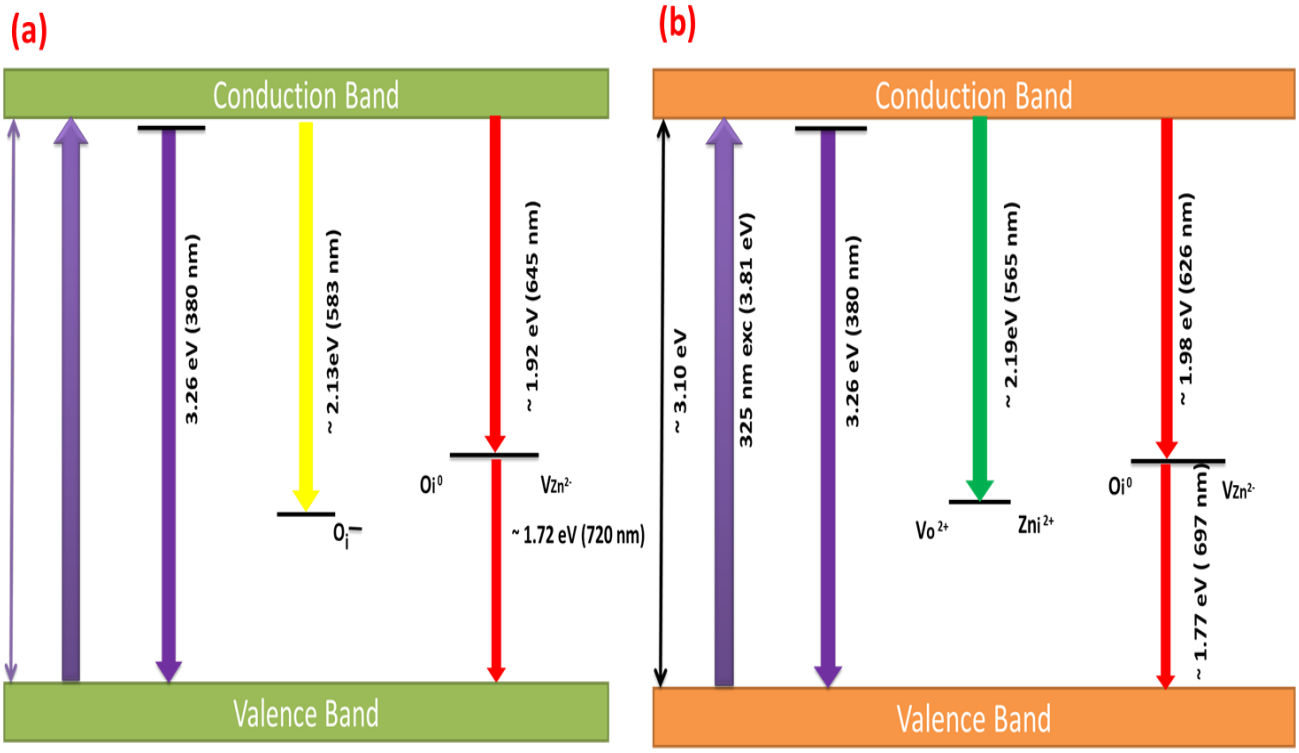

Figure 4.10. (a-b): Energy diagram of as-prepared undoped ZnO sample synthesized at 600˚C and 700˚C.

4.5. Conclusion

ZnO phosphors were successfully synthesized via solution combustion synthesis method and their crystallization was confirmed by XRD analysis. The ZnO powder crystallized in the hexagonal phase. The diffraction patterns became sharper and more intense with increasing synthesis temperature from 600˚C to 700˚C indicating improvement of crystallinity and an increase in crystallite sizes from 23.3 nm to 30.06 nm of the as-prepared undoped ZnO phosphor powder.

The SEM images show agglomeration of small particles and flower-like morphology, and all the elements present in the phosphors were confirmed by EDS. The HR-TEM images show that the ZnO NPs are hexagonally shaped and aggregated into clusters.

With respect to the photoluminescence results the un-doped ZnO has two characteristic peaks. A narrow one in the UV region at 380 nm results from recombination of free excitons, while broad peaks in the visible region at 639 nm for ZnO synthesized at 600˚C and 626 nm for ZnO synthesized at 700˚C sample are attributed to defects within the bandgap.

In conclusion as the synthesis temperature was increased from 600˚C to 700˚C there was an improvement of crystallinity and an increase in crystallite sizes. With respect to the PL results the broad visible region PL emission peak shifted to the blue region from 693 to 626 nm.

References:

[1] Joshi SS, Patil PR, Naimase M.S, Bakare PP: Role of ligands in the formation,

phase stabilization, structural and magnetic properties of α-Fe2O3 nanoparticles. J. Nanopart. Res. 5, 635–643 (2006)

[2] Cheng, XL, Zhao, H, Huo, LH, Gao, S, Zhao, JG: ZnO nanoparticulate thin

film: preparation, characterization and gas-sensing properties. Sens. Actuators B. 102, 248 252 (2004)

[3] Lee, SY, Shim, ES, Kang, HS, Pang, SS: Fabrication of ZnO thin film diode

using laser annealing. Thin Solid Films. 437, 31–34 (2005)

[4] Wang, ZL, Kong, XY, Ding, Y, Gao, P, Hughes, WL: Semiconducting and

piezoelectric oxide nanostructures induced by polar surfaces. Adv. Funct. Mater. 14, 943–956 (2004)

[5] Huang, YH, Zang, Y, Liu, L, Fan, SS, Wei, Y, He, J: Controlled synthesis and field emission properties of ZnO nanostructures with different morphologies. J. Nanosci. Nanotechnol. 6, 787–790 (2006)

[6] Bhargava RN, Chhabra V, Som T, Ekimov A, Taskar N (2002) Phys Stat Sol (b) 229:897

[7] Kawasaki M, Ohtomo A, Ohkubo I, Koinuma H, Tang ZK, Yu P, Wong GKL, Zhang BP, Segawa Y (1998) Mater Sci Eng B 56:239

[8] Bagnall DM, Chen YF, Shen MY, Zhu Z, Yao GT (1998) J Cryst Growth 184/185:605

[9] Li ZL, Xin GC, Jing ZJ, Tao HJ (2005) Chin Phys Lett 22:122

[10] Segets, D.; Gradl, J.; Taylor, R.K.; Vassilev, V.; Peukert, W. Analysis of optical absorbance spectra for the determination of ZnO nanoparticle size distribution, solubility, and surface energy. *ACS Nano* **2009**, *3*, 1703–1710. [11] Lou, X. Development of ZnO series ceramic semiconductor gas sensors. *J. Sens. Trans. Technol.* **1991**, *3*, 1–5.

[12] Bacaksiz, E.; Parlak, M.; Tomakin, M.; Özcelik, A.; Karakiz, M.; Altunbas, M. The effect of zinc nitrate, zinc acetate and zinc chloride precursors on investigation of structural and optical properties of ZnO thin films. *J. Alloy. Compd.* **2008**, *466*, 447–450.

[13] Wang, J.; Cao, J.; Fang, B.; Lu, P.; Deng, S.; Wang, H. Synthesis and characterization of multipod, flower-like, and shuttle-like ZnO frameworks in ionic liquids. *Mater. Lett.* **2005**, *59*, 1405–1408.

[14] Wang, Z.L. Splendid one-dimensional nanostructures of zinc oxide: A new nanomaterial family for nanotechnology. *ACS Nano* **2008**, *2*, 1987–1992.

[15] Chaari, M.; Matoussi, A. Electrical conduction and dielectric studies of ZnO pellets. *Phys. B Condens. Matter* **2012**, *407*, 3441–3447.

[16] Özgür, Ü.; Alivov, Y.I.; Liu, C.; Teke, A.; Reshchikov, M.A.; Doğan, S.; Avrutin, V.; Cho, S.J.; Morkoç, H. A comprehensive review of ZnO materials and devices. *J. Appl. Phys.* **2005**, *98*, doi:10.1063/1.1992666.

[17] Bhattacharyya, S.; Gedanken, A. A template-free, sonochemical route to porous ZnO nano-disks. *Microporous Mesoporous Mater.* **2007**, *110*, 553–559.

[18] Ludi, B.; Niederberger, M. Zinc oxide nanoparticles: Chemical mechanism and classical and non-classical crystallization. *Dalton Trans*. **2013**, *42*, 12554–12568.

[19] Shukla S.K., Agorku E.S., Mittal H., Mishra A.K., Synthesis, characterization and photoluminescence properties of Ce^{+3} doped ZnO nanophosphors,Chemical papers 68 (2) 217-222 (2014).

[20] Banerjee, D.; Lao, J.Y.; Wang, D.Z.; Huang, J.Y.; Ren, Z.F.; Steeves, D.; Kimball, B.; Sennett, M. Large-quantity free-standing ZnO nanowires. *Appl. Phys. Lett.* **2003**, *83*, 2061–2063.

[21] Hahn, Y.B. Zinc oxide nanostructures and their applications. *Korean J. Chem. Eng*. **2011**, *28*, 1797–1813.

[22] Frade, T.; Melo, Jorge, M.E.; Gomes, A. One-dimensional ZnO nanostructured films: Effect of oxide nanoparticles. *Mater. Lett.* **2012**, *82*, 13–15.

[23] Wahab, R.; Ansari, S.G.; Kim, Y.S.; Seo, H.K.; Shin, H.S. Room temperature synthesis of needle-shaped ZnO nanorods via sonochemical method. *Appl. Surf. Sci.* **2007**, *253*, 7622–7626.

[24] Kong, X.; Ding, Y.; Yang, R.; Wang, Z.L. Single-crystal nanorings formed by epitaxial self-coiling of polar-nanobelts. *Science* **2004**, *303*, 1348–1351.

[25] Pan, Z.W.; Dai, Z.R.; Wang, Z.L. Nanobelts of semiconducting oxides. *Science* **2001**, *291*, 1947–1949.

[26] Wu, J.J.; Liu, S.C.; Wu, C.T.; Chen, K.H.; Chenm, L.C. Heterostructures of ZnO–Zn coaxial nanocables and ZnO nanotubes. *Appl. Phys. Lett.* **2002**, *81*, 1312–1314.

[27] Bandopadhay K., Mitra J., *RSC **Adv**.,* 2015,5, 23540–23547

[28] Kumar V R, Kavitha V T, Wariar P R S, Nair S U K and Koshy J 2011 *J. Physics & Chem. Solids* **72** 290

[29] Sousa V C, Segadaes A M, Morelli M R and Kiminami R H G A 1999 *Itnl. J. Inorganic Mat.* **1** 235

[30] Monshi A, Foroughi MA, Modified Scherrer Equation to Estimate More Accurately Nano-Crystallite Size Using XRD, World Journal of Nano Science and Engineering, 2012, 2, 154-160.

[31] http://www.matter.org.uk/diffraction/electron/ratio_technique.htm [Accessed September 2016]

[32] Nguyen T. K. , Thanh N. Maclean, Mahiddine S., Mechanisms of Nucleation and Growth of Nanoparticles in Solution, Chem. Rev. 2014, 114, 7610−7630.

[33] Kumar V., Ntwaeaborwa O.M. , Coetsee E. , Swart H.C., Role of deposition time on the properties of ZnO:Tb3+ thin films prepared by pulsed laser deposition, Journal of Colloid and Interface Science, 474 (2016), 129–136.

[34] Epie E.N., Chu W.K. , Ionoluminescence study of Zn− and O− implanted ZnO crystals: An additional perspective, Applied Surface Science 371 (2016) 28–34.

Chapter 5: The structural, morphological and optical studies of MgO synthesized by solution combustion method.

5.1. Introduction

Magnesium (Mg) is a IIA group element with atomic number 12 and oxygen (O) is a VIA group element with atomic number 8. The compound magnesium oxide (MgO) has boiling and melting points of 3600ºC and 2852ºC [1]. It is a unique solid because of its highly ionic character, simple stoichiometry and crystal structure, and it can be prepared in widely variable particle shapes and sizes [2]. MgO is a very suitable material for insulation applications because of its low heat capacity and high melting point [3].

It has been documented that the shape and size of nanocrystalline MgO particles endow them with high specific surface and reactivity, because of the high concentration of edge/corner sites and structural defects on their surface [4]. Magnesium oxide is a wide band gap insulator with bandgap of 7.7 eV, it has cubic crystal structure with Fm-3m space group. It is an insulator which crystallizes in the rocksalt/sodium chloride (NaCl) type cubic structure. Like MgO, many binary oxides such as CaO, SrO, BaO, NiO, and CoO also crystallize in rocksalt structure [5].

The magnesium ions occupy octahedral sites within the anion closed packed structure. It's ionic constituents comprise of a relatively small number of electrons [6,7]. Due to its simple crystal structure and perfect iconicity MgO appears to form outstanding building blocks for the construction of functional nanostructures and to serve as a suitable model compound for the investigation of surface reactivity on oxides [6,7].

MgO has many industrial applications, for example in medicine, refractory materials, heating apparatus and infrared optics, catalysis, adsorption, synthesis of refractory ceramics, water purification, optoelectronics, microelectronics, additive in heavy fuel oil, paint, gas separation,

bactericides, insulator in industrial cables, crucibles, oxide barriers in spin tunneling devices as well as a substrate in superconducting and ferroelectric films [8]. Metal oxides such as MgO are extremely important technological materials for use in catalysis, catalyst support, electronic and photonic devices [8].

MgO can be prepared by different synthesis methods such as solution combustion [9], hydrothermal [10], Sol-Gel [11], Solvothermal [12], Microwave Assisted Sol-Gel [13], Co-precipitation [14] and green synthesis [15]. Among the available chemical methods solution combustion synthesis (SCS) has been a versatile, simple and rapid process which allows effective synthesis for wide range of nano-sized materials [16]. Depending on the type of the precursors as well as the conditions used for the process, the SCS may occur as either volume or layer-by-layer propagating combustion modes [16].

This chapter reports on the preparation of the MgO samples synthesised 600˚C using solution combustion synthesis and urea as a fuel. The structure, morphology, reflectance and hence absorption behaviour, bandgap and photoluminescence properties are investigated.

5.2. Experimental:

5.2.1 Preparation of MgO

Magnesium nitrate hexahydrate and urea were used as starting materials. The materials were mixed stiochiometrically according to the following chemical reaction equation:

$$3Mg(NO_3)_2\,(H_2O)_6 + 5CH_4N_2O \rightarrow 3MgO + 28H_2O + 5CO_2 \uparrow + 8N_2 \uparrow \qquad (5.1)$$

In a typical preparation of 0.5 g of urea, 1.281 g of magnesium nitrate hexahydrate and 3 mL of deionized water were mixed together, and stirred for 30 minutes at approximately 80˚C to achieve a homogenous solution. The solution kept in a crucible was transferred to a furnace which was pre-set to a synthesis temperature of 600˚C ± 15, for 15 minutes. A white powder formed after the reaction was complete. A typical flame in combustion synthesis technique was not observed. Depicted in figure 5.1 is a schematic representation of this synthesis method.

5.2.2 Characterization

The structural properties of the MgO powder were analysed using a Bruker D8 Advance powder diffractometer with a Cu-Kα radiation wavelength of 1.54 Å and a Nicolet 6700 Fourier transform infrared (FTIR) spectroscope. The morphology and elemental composition of the materials was analysed using a Jeol JSM-7800F field emission scanning electron microscope (FE-SEM) coupled with Oxford Aztec 350 X-Max80 energy-dispersive X-ray spectroscopy (EDS). In addition, a JEOL ARM200F transmission electron microscope was used for particle morphology and crystalline structure analysis. The diffuse reflectance data was recorded using ultraviolet visible (UV–vis) spectrometer by a Perkin Elmer Lambda 950 UV–vis. The

photoluminescence data was recorded at room temperature using a 325 nm He-Cd laser as excitation source.

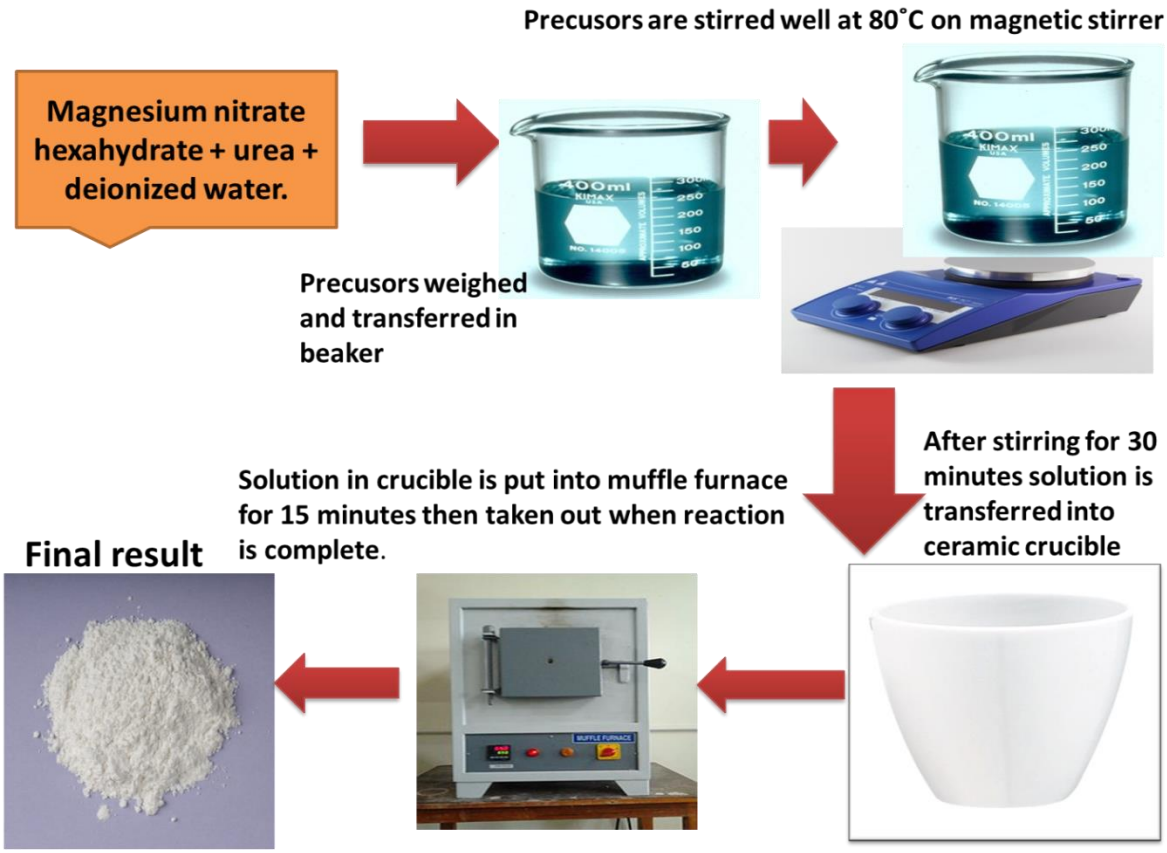

Figure 5.1. Graphical representation for preparation of MgO using solution combustion synthesis method.

5.3. Results and Discussion

5.3.1. Structural Studies

5.3.1.1. XRD Results

Figure 5.2 shows the XRD pattern of MgO powder synthesized at 600˚C. The patterns are consistent with the cubic structure of MgO referenced in JCPDS Card Number 45-0946. The crystal sizes were estimated by using the Scherrer equation (equation 5.2). The XRD diffraction peaks are sharp and intense indicating good crystallinity as a results of the high synthesis temperature for this sample.

$$D = \frac{K\lambda}{\beta \cos\theta} \qquad (5.2)$$

where D is the mean size of the ordered (crystalline) domains, which may be smaller or equal to the grain size. K is a dimensionless shape factor, with a value close to unity. The shape factor

has a typical value of about 0.9, but varies with the actual shape of the crystallite, λ is the X-ray wavelength. β is the line broadening at half the maximum intensity (FWHM), after subtracting the instrumental line broadening, in radians. This quantity is also sometimes denoted as $\Delta(2\theta)$;θ is the Bragg angle.

The total number of peaks were used to calculate the crystallite size then the average value was taken. The average crystallite size for MgO synthesized at 600˚C was 23.3 nm.

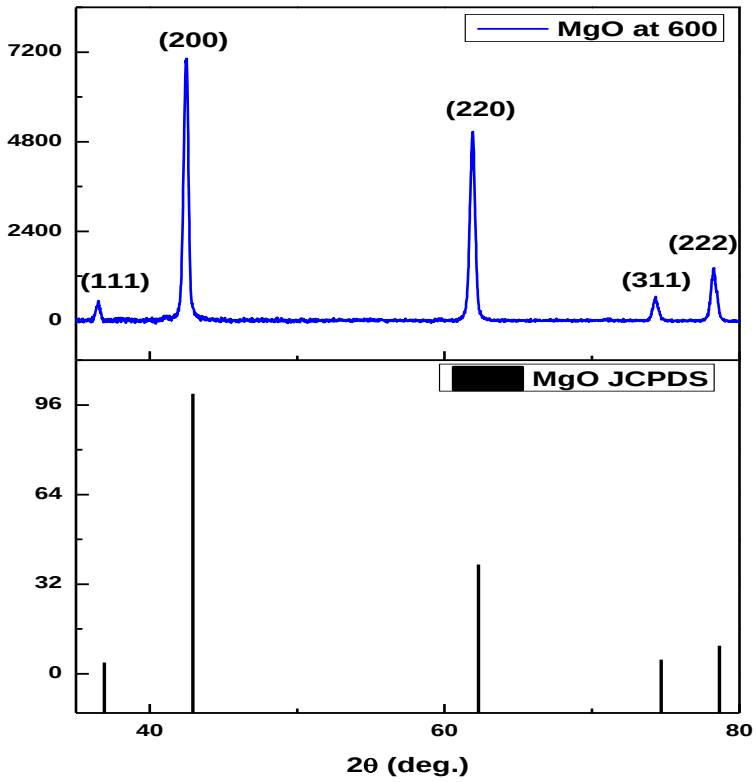

Figure 5.2: XRD patterns of as-prepared un-doped MgO powder synthesized at 600˚C and matching JCPDS Card No. 45-0946.

Table 5.1: Calculation of crystallite size for the as-prepared undoped MgO sample synthesized at 600˚C.

MgO analysis				
2θ	**Θ**	**β(deg)**	**β(rad)**	**D**
36.55	18.275	0.32255	0.005630	25.9
42.48	21.240	0.38334	0.006691	22.2
61.8	30.900	0.42253	0.007375	21.9
74.4	37.200	0.42632	0.007441	23.4
78.35	39.175	0.45586	0.007956	23.05

5.3.1.2 FTIR Results

The FT-IR spectrum for the MgO powder is depicted in figure 5.3. The stretching vibration mode of Mg-O is located at 617 cm $^{-1}$ as a broad band. There is a narrow band at 1381 cm $^{-1}$ and is attributed to the bending vibration of absorbed water molecule and surface hydroxyl group (-OH). A broad band located at 2366 cm $^{-1}$ is due to O-H stretching vibration of absorbed water molecule and surface hydroxyl group. This is due to the aerial adsorptions of water molecules onto the MgO surface coming from the atmospheric moisture [17].

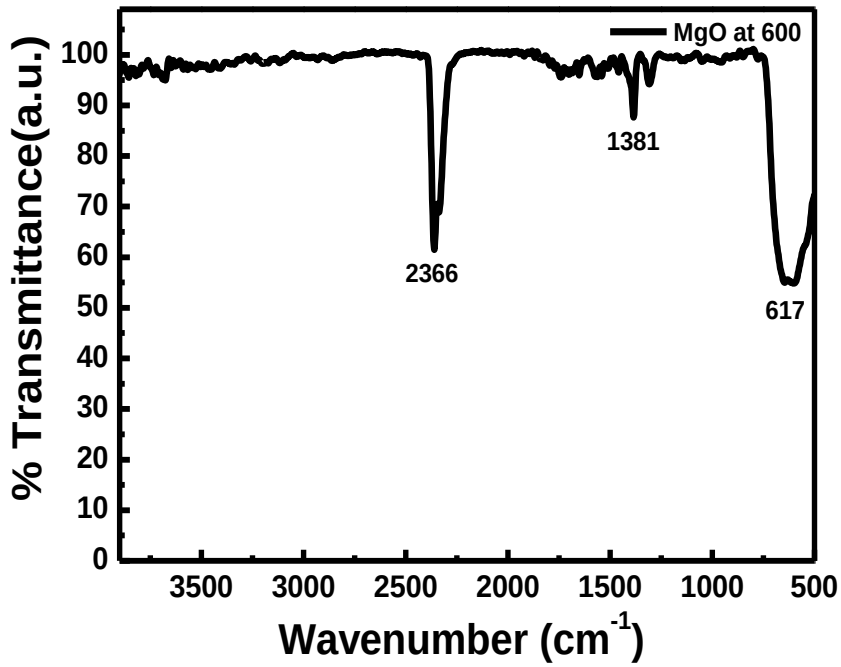

Figure 5.3: The FTIR spectra of as-prepared undoped MgO sample synthesized at 600˚C.

5.3.2. SEM Results:

5.3.2.1. Particle Morphological and Chemical Composition characteristics

High resolution scanning electron microscopy (SEM) analysis was performed to evaluate the fine-scaled topological features of MgO powder sample. The SEM micrographs at different magnifications are depicted in figure 5.4. It was observed that the microstructure possess uniform shape but slightly different particle sizes, without any significant change in homogeneity. Spherical cube-like morphology is observed with appearance of closely-packed or attached particles in all the SEM micrographs.

The EDS spectra is shown in figure 5.5. In the EDS spectra all elements present in the MgO sample were observed i.e. the magnesium and oxygen peaks. The carbon peak can be attributed to the carbon tape on which the sample was mounted. The weight percentage of the elements present in the sample observed on the surface are as follows: for magnesium it is 60.00%, oxygen it is 37.78% and lastly for carbon it's 2.22%. These results are in good correlation to the calculated theoretical values, which are Mg 60.30 % and oxygen 39.70%.

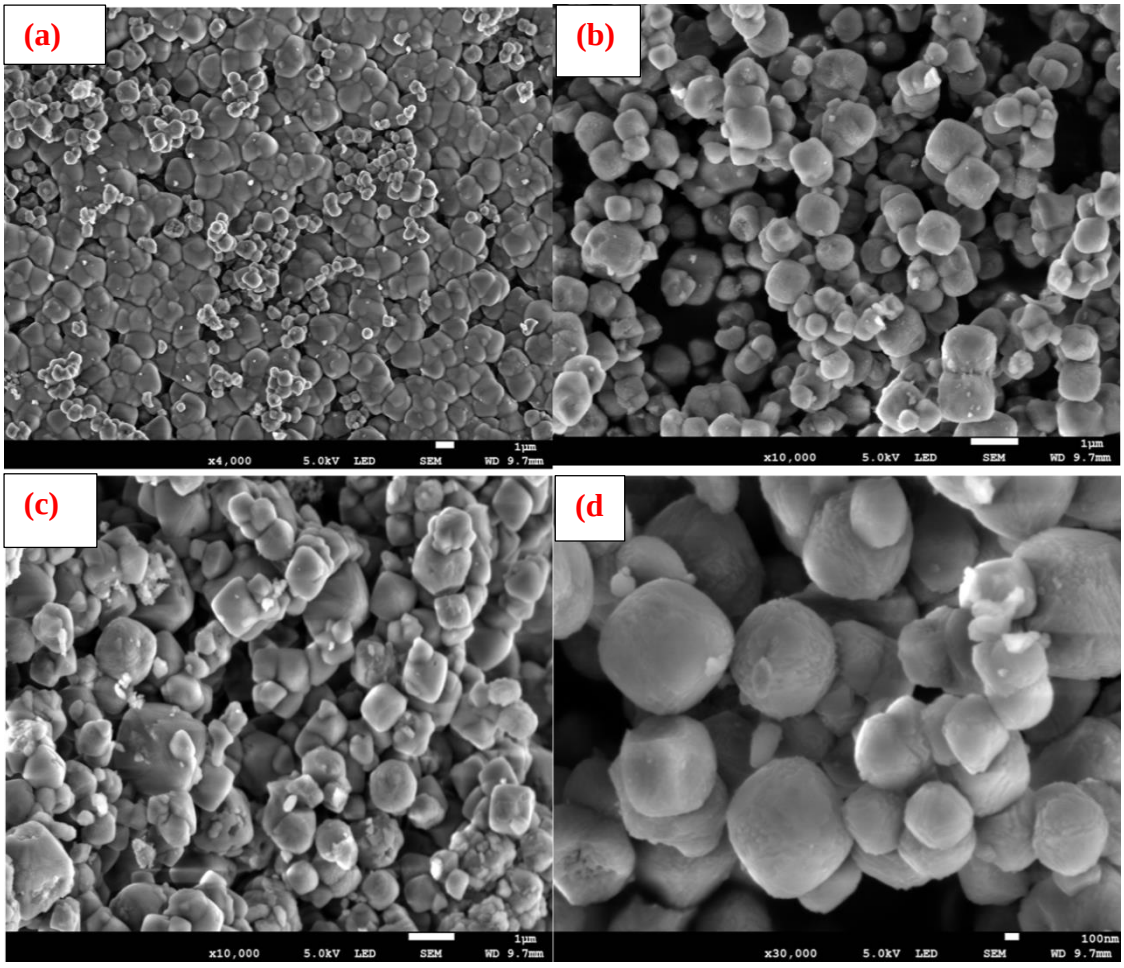

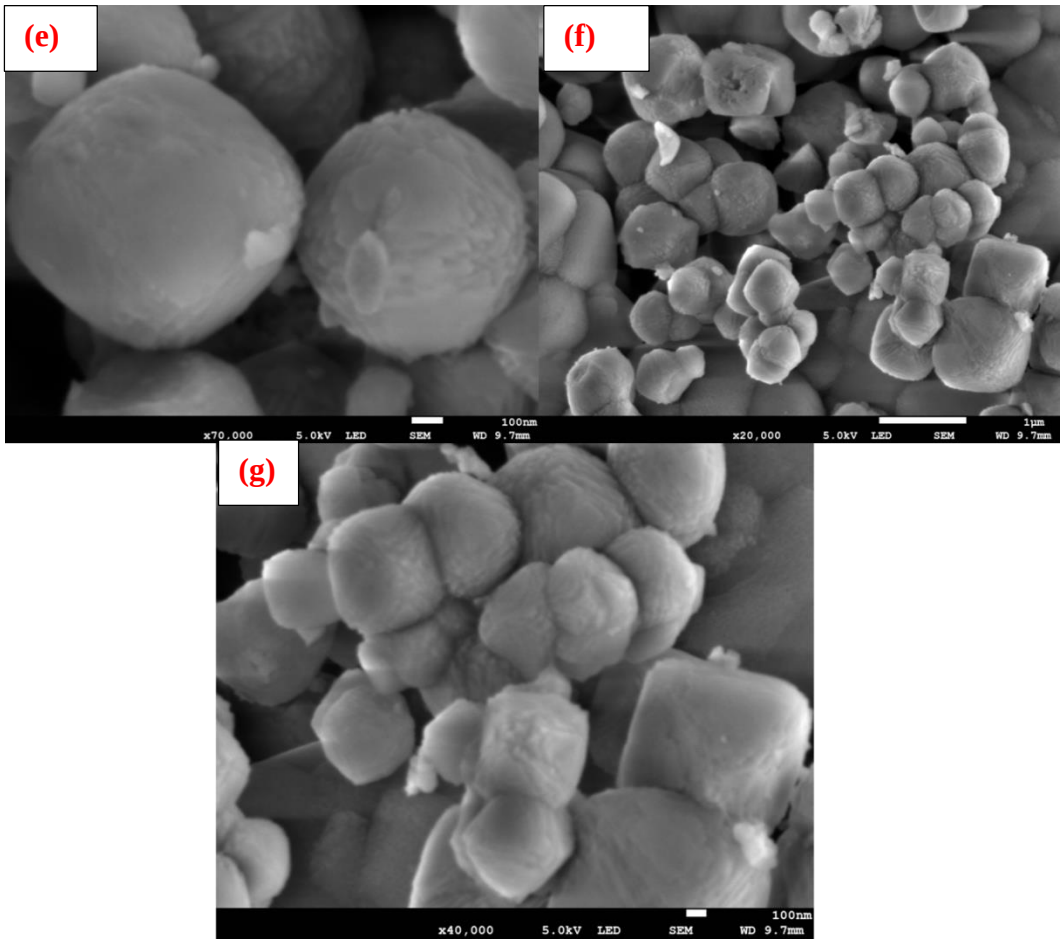

Figure 5.4 (a-g): SEM images of as-prepared undoped MgO sample synthesized at 600˚C.

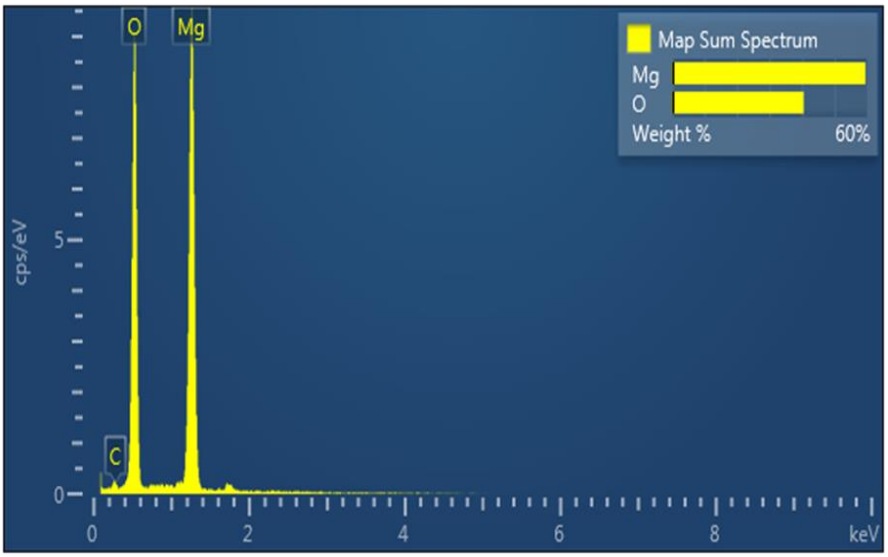

Figure 5.5: The EDS spectra of as-prepared undoped MgO sample synthesized at 600˚C.

5.3.2.2. Particle Formation Mechanism:

In this synthesis system a complex MgO is formed during the decomposition of $Mg(NO_3)_2(H_2O)_6$ by a complexing agent urea. The consequent reaction in the formation of MgO is as follows

$$Mg\,(NO_3)_2 \bullet 6H_2O \xrightarrow{\text{Dissolution}} MgO\,(NO_3)_2 + 6H_2O \qquad (5.3)$$

The water molecule binding sites are significantly very stable even at room temperature but in this case the dissolution occurred at a temperature of 80˚C. The formation of magnesium oxide nanocrystals from magnesium nitrate hexahydrate involves three steps, (a) dissolution, (b) decomposition of precusors, and (c) formation of cubic-spherical structured MgO. This process is depicted in figure 5.6.

In dissolution the solid powder of magnesium nitrate hexahydrate undergoes solvation to release magnesium nitrate, given by Eq. 5.2. The magnesium nitrate reacts with the fuel and complexing agent urea to form MgO as elaborated in Eq. 5.1. This chemical reaction produces the six fold coordinated MgO cubic structure when temperature of 600˚C is reached inside the furnace in accordance with Eq. 5.1. The obtained MgO has rocksalt (NaCl, B1) type structure. The high ionic interaction between Mg^{2+} ($1s^2 2s^2 2p^6$) and O^{2-} ($1s^2 2s^2 2p^6$) provides its high thermal stability [18]. The strong attraction between two oppositely charged ions and the formation of divalent cation of magnesium and divalent
anion of oxygen leads to the formation of MgO [18].

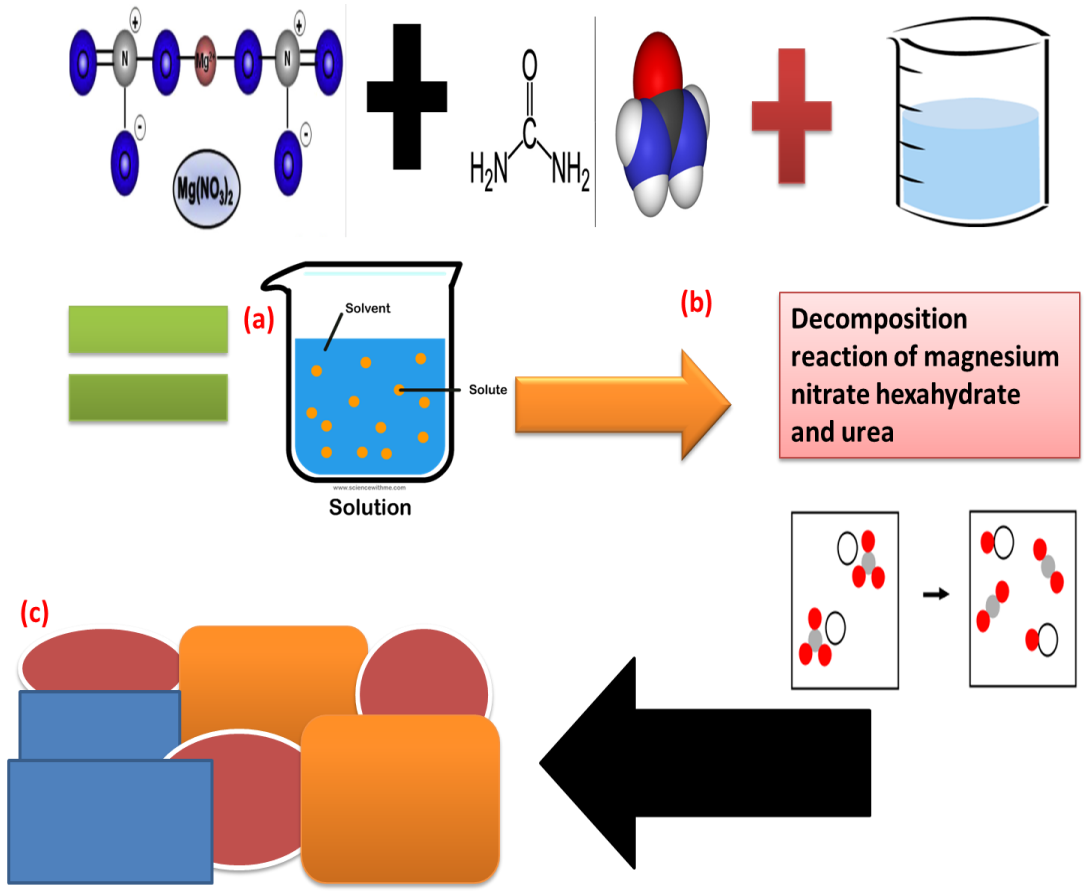

Figure 5.6: Schematic diagram of possible formation of the MgO nanoparticles.

5.3.2.2. HR-TEM Results:

The HR-TEM micrograph and SAED pattern of MgO NPs are depicted in figure 5.7 (a & b). These were obtained from solution combustion synthesis of one as-prepared undoped MgO sample, at a synthesis temperature of 600˚C. The HR-TEM images show that the MgO NPs are cubic-spherically shaped and aggregated into clusters. At high synthesis temperatures such as 600˚C many neighbouring particles are prone to fuse together to form larger particles. The average calculated crystallite size from XRD data is 23.296 nm and the average particle size from the HR-TEM micrograph is 57.452 nm which is a multiple of the average crystallite size. The XRD and HR-TEM results are in good correlation to each other.

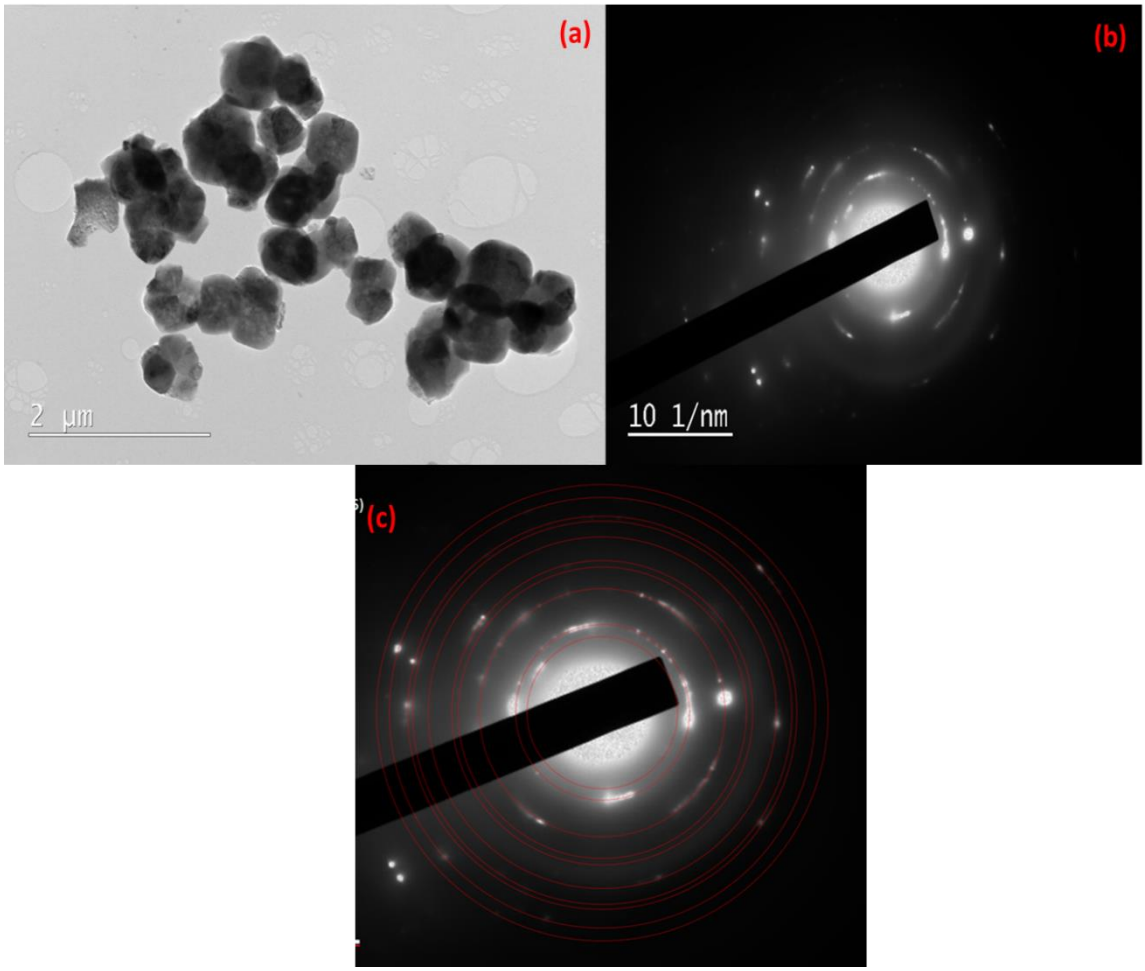

Figure 5.7 (a-c) : Illustration of HR-TEM micrograph and SAED pattern.

The d-spacing of lattice planes (d_{hkl}) can be determined based on Bragg's formula as follows:

$$d_{hkl} = \frac{n\lambda}{2\sin\theta} \quad (5.4)$$

For a cubic crystal structure MgO the interplaning spacings are given by the following equation:

$$d = \frac{a}{\sqrt{h^2+k^2+l^2}} \quad (5.5)$$

With regards to the data from the Table 5.2: a PDF (45-0945)) X-ray file for MgO was obatained and from it the expected d-spacings were calculated. Then the value 1/d (converted to nm first) was calculated as to obtain the expected ring radii. Using the scale bar on the SAED image, rings were plotted with diameters double these radii, centres and the rings. The match for MgO was good. From this it can be deduced that the XRD and SAED results for the MgO sample are in good correspondence.

Table 5.2: Calculation of R values between SAED and XRD data

MgO				
hkl	**d(A)**	**R(nm^{-1})**	**2R(nm^{-1})**	**(*1.13)**
111	2.4316	4.11	8.23	9.29
200	2.1056	4.75	9.50	10.73
220	1.4890	6.72	13.43	15.18
311	1.2698	7.88	15.75	17.80
222	1.2157	8.23	16.45	18.59
400	1.0528	9.50	19.00	21.47
331	0.9662	10.35	20.70	23.39
420	0.9417	10.62	21.24	24.00
422	0.8597	11.63	23.26	26.29
511	0.8105	12.34	24.68	27.88

5.4. Optical Studies:

5.4.1. UV-Vis Results:

The diffuse reflectance spectra were measured in the range of 200-600 nm at room temperature and shown in Figure 5.8 (a). The optical bandgap value for the as-prepared undoped MgO sample synthesized at 600˚C was determined from reflectance spectra using the Kubelka-Munk equation:

$$F(R) = (1–R)^2/2R = k/s \quad (5.6)$$

where, R = reflectance; k = absorption coefficient; s = scattering coefficient; It gives a correlation between the reflectance and the concentrations of absorbing species. The Tauc relation is given as:

$$(F(R)\cdot hv)^2 = A\,(hv - E_g) \quad (5.7)$$

where F(R) is the Kubelka-Munk function, hv is the incident photon energy, A is a constant depending on the transition probability and the diffuse reflectance (R). The Tauc plot method

was used to plot the values of $(F(R)\cdot hv)^2$ vs. hv as illustrated in Figure 5.8 (b). This was done in order to determine the optical band gap value of the MgO nanoparticles.

The highest reflectance observed with the as-prepared undoped MgO sample was at 62%, with an absorbance peak 499 nm, a curvature at 266 nm and an absorption edge at 222 nm. The presence of absorption peaks could be attributed to the possible introduction of more defects within the bandgap. The bandgap of this sample was calculated from the absorption edge at 222 nm and it was 5.22 eV. The theoretical bandgap of MgO is 7.7 eV. There is a significant difference between the theoretical and experimental bandgap values, the difference in bandgap can be attributed to the fact that this MgO sample was synthesized via solution combustion method and hence there is a possible introduction of more defects in this synthesis method. This fact will be explored further in the photoluminescence discussion when elaborating on the light properties of this sample.

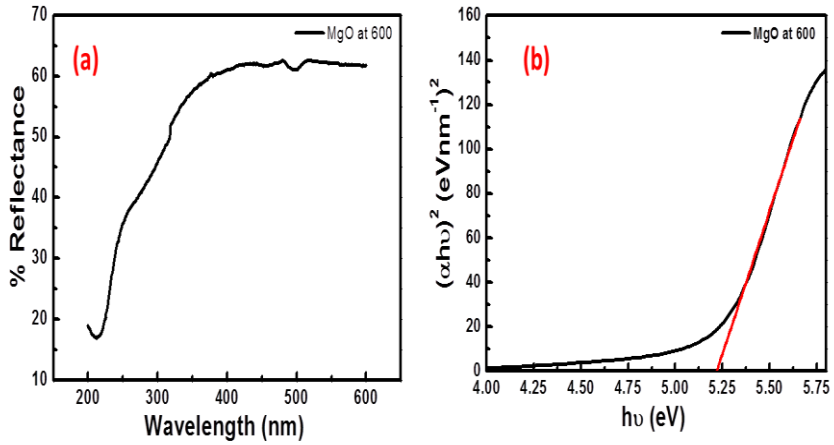

Figure 5.8. (a & b) : UV-Vis reflectance spectra and bandgap graphs for the as-prepared un-doped MgO sample synthesized at 600˚C.

5.4.1.2. Photoluminescence Results:

Figure 5.9 (a) is the photoluminescence spectrum of MgO sample synthesized at 600˚C, the excitation used was from the He-Cd laser source with wavelength of 325 nm. This MgO sample has three shoulder emission peaks at approximately 419, 432 and 465 nm and a minute emission peak in the visible region at 663 nm. Figure 5.9 (b) shows the deconvuluted peaks are at 413, 430 and 461 nm.

As a wide-band-gap insulator, MgO usually would not exhibit PL in the visible light region. However, it has been found that charge transfer on the surface states could result in UV-visible luminescence, although the surfaces states (that are usually attributed to specific low-

coordinated sites) are still ambiguous. For the present case, the MgO nanoparticles are in the nanometre scale, which inevitably results in large amounts of surface states. Structurally, MgO belongs to the rock salt structure where Mg^{2+} and O^{2-} ions are both six-coordinated in its bulk. On the rough surface, however, the coordination number of both cations and anions should decrease, which should generate various low coordinated oxygen sites. Therefore both the emissions centred at 405 nm and 470 nm are relevant to pristine and modified three-/four-coordinated (3C/4C) oxygen sites, respectively [19].

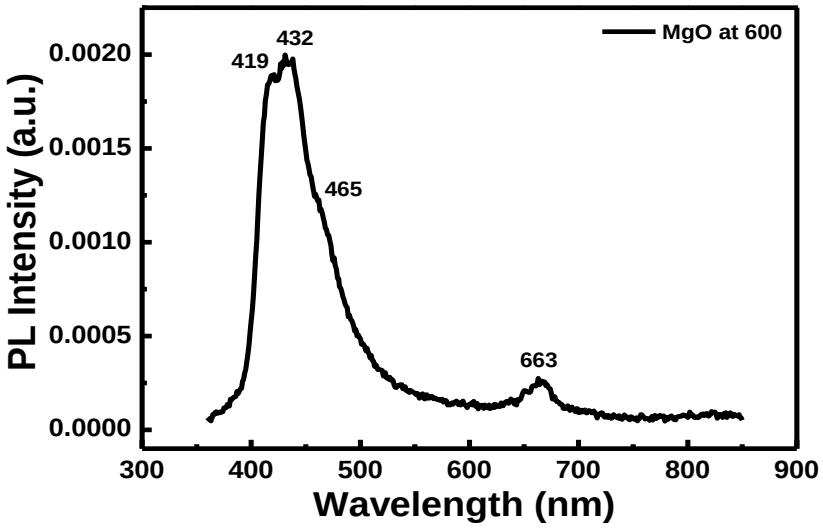

Figure 5.9 (a): Photoluminescence spectra of as-prepared un-doped MgO sample synthesized at 600˚C.

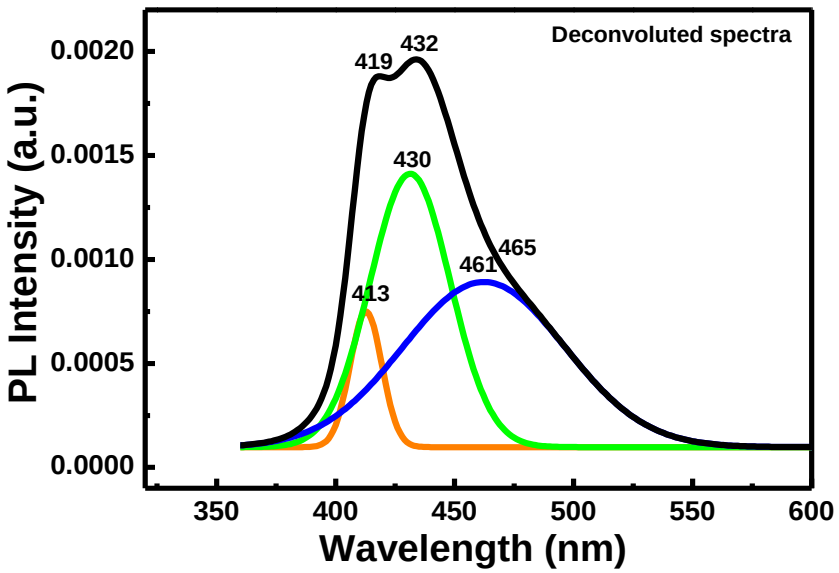

Figure 5.9 (b) Deconvoluted spectra of as-prepared un-doped MgO sample synthesized at 600˚C.

5.5. Conclusion:

The MgO phosphors were successfully synthesized via the solution combustion synthesis method and confirmed by XRD analysis which showed sharp and intense peaks indicating good crystallinity because of a higher than an average (500-550 °C) solution combustion synthesis temperature of 600 °C.

The SEM images show rounded cube-like morphology with the appearance of closely-packed or attached particles. The HR-TEM images show that the MgO NPs have the shape of rounded cubes and aggregated into clusters, which is in good agreement with the SEM results.

PL emission peaks occurred at approximately 419, 432 and 465 nm with a minute emission peak in the visible region at 663 nm. MgO usually would not exhibit PL in the visible light region, but it has been suggested that charge transfer on the surface states could also result in visible region luminescence.

References:

[1] Bai J., Fantao Meng, Wei C. , Zhao Y., Tan H., Liu J., Solution Combustion Synthesis And Characteristics Of Nanoscale MgO Powders. Ceramics – Silikáty, 55(1) ,(2011),20.

[2] Itoh H., Utamapanya S., Stark J.V., Klabunde K.J. , Schlup J.R., Chem. Mater.,5, (1993),71.

[3] Wu M.C., Corneille J.S.,. Estrada C.A, He J.W., Goodman D.W., Synthesis and Characterization of Ultra-Thin MgO Films on Mo (100), Chem. Phys. Lett., 182,(1991),472.

[4] Klabunde K.J., Stark J., Koper O., Mohs C., Park D.G., Decker S., Jiang Y., Lagadic I., Zhang D., J. Phys. Chem., 100 (1996), 12142.

[5] Spoto G., Gribov E.N., Ricchiardietal G., Carbon monoxide MgO from dispersed solids to single crystals are view and new advances, Progress in Surface Science ,76 ,(2004), 3-5,71–146.

[6] Chen L, Sun X., Liu Y., Li Y., Preparation and characterization of porous MgO and NiO/MgO nanocomposites , Appl. Catal. A: Gen.,265(1),(2004),123.

[7] Yang S.Y., Kim S.G., Powder Technol. 146, (2004), 185–192

[8] Wu M.C., Corneille J.S.,. Estrada C.A, He J.W., Goodman D.W., Synthesis and Characterization of Ultra-Thin MgO Films on Mo (100), Chem. Phys. Lett., 182, (1991) ,472.

[9] Jiahai Bai, FantaoMeng, Chuncheng Wei, Yunxia Zhao, Huihui Tan and Juncheng Liu., Solution Combustion Synthesis And Characteristics Of Nanoscale MgO Powders, Ceramics – Silikáty, 55(1), (2011),20.

[10] Hiromichi Hayashi and Yukiya Hakuta., Hydrothermal Synthesis of Metal Oxide Nanoparticles in Supercritical Water, Materials 3,(2010),3794.

[11] Tamilselvi P., Yelilarasi A., Hema M and Anbarasan R, Synthesis Of Hierarchical Structured MgO By Sol-Gel Method, Nano Bulletin, 2(130106),(2013),1.

[12] YanglongHou, Yu J., Gao S., Solvothermal Reduction Synthesis and Characterization of Superparamagnetic Magnetite Nanoparticles, J. Mater. Chem., 13,(2003), 1983.

[13] Mirzaei H., Davoodnia A., Microwave Assisted Sol-Gel Synthesis of MgO Nanoparticles and Their Catalytic Activity in the Synthesis of Hantzsch 1, 4Dihydropyridines, Chinese Journal of Catalysis, 33,(2012),1502.

[14] Vatsha B., Tetyana P., Shumbula P.M., Ngila J.C. , Sikhwivhil L.M., Moutloali R.M. ., Effects of Precipitation Temperature on Nanoparticle Surface Area and Antibacterial Behaviour of Mg(OH)2 and MgO Nanoparticles, Journal of Biomaterials and Nanobiotechnology, 4, (2013), 365.

[15] Patil A.B., Bhanage B.M., Novel And Green Approach For The Nano crystalline Magnesium Oxide synthesis And Its Catalytic Performance In Claisen– Schmidt Condensation, Catalysis Communications, 36, (2013),79.

[16] Devaraja P.B., Avadhani D.N., Prashantha S.C., Sharma, S.C., Nagabhushana B.M., MgO:Dy^{+3} nanophosphor: self- ignition route, characterization and its photoluminescence properties, Materials Characterization, 97,(2014), 27-36.

[17] Balamurugan S., Ashna L.,Parthiban P., Synthesis of Nanocrystalline MgO Particles by Combustion Followed by Annealing Method Using Hexamine as a Fuel, Journal of Nanotechnology, 841803,(2014), 1.

[18] Verma R, Naik K.K., Gangwar J, Srivastava A.K., Morphology, mechanism and optical properties of nanometer-sized MgO synthesized via facile wet chemical method, Materials Chemistry and Physics,148,(2014),1064.

[19] Xie S, Han X, Kuang Q, Zhao Y, Xie Z, Zheng L, Intense and wavelength-tunable photoluminescence from surface functionalized MgO nanocrystal clusters, Journal of Materials Chemistry,21(2), (2011),7263

Chapter 6: The solution combustion synthesis study of mixed phase SrO phosphor.

6.1. Introduction

The most extensive use of strontium oxide powder (SrO) was in the cathode ray tubes industry, where it was employed in the form of an aluminium alloy to help protect humans from X-ray emissions in the traditional colour televisions. However, this long lasting technology has now been replaced by the widespread use of flat displays (either liquid crystal or plasma displays). In recent years SrO powders have been essential in novel technological applications in the chemical and electronic industries, including the production of ferrite ceramic magnets and zinc refining [1].

SrO is electrically conductive and it has been used in fuel cells and oxygen generation systems as a cathode material in the solid state form. Due to its optical properties it has been employed to improve the quality of special glasses. Diverse strontium salts are currently consumed as pyrotechnic materials or paint additives or employed in fuel production catalysis [2,3].

SrO has the potential for use in medical appliances, such as tissue or body member replacements, restorative implant cement or filling compounds. Although the consumption demands fluctuate from year to year, the overall consumption of strontium compounds and metals appears to be increasing [4].

Therefore, diverse technologies for the synthesis of advanced ceramic materials, such as strontium oxide, have been investigated to discover new cost effective and efficient methods of production. Nanocrystalline SrO has been previously prepared using aerogel and conventional methods that have yielded small amounts of product, hence combustion synthesis has become a promising technique because it is a fast and straightforward process that produces homogeneous, very fine, and crystalline multi component oxide ceramic powders [5,6].

The chemical combustion synthesis is based on the principle of explosive decomposition of nitrate reagents and fuel mixtures using the instantaneous heat generated by the chemical reaction between the fuel and nitrates to convert the metal ions into the target ceramic material [7].

The classical solution combustion synthesis method consists of placing an aqueous solution that contains salts of the metal of interest (the nitrates of the metal due to their good water solubility are typically preferred) in contact with an appropriate organic fuel, such as urea, at temperatures of 400 to 1100 °C. When the mixture heats up, it generates instantaneous heat that initiates a very fast and abrupt exothermal reaction that yields a metallic oxide in the form of a fine powder. This powder is crystalline and ready for use as advanced ceramics with interesting magnetic, dielectric, electrical, mechanical, luminescent, catalytic, photocatalytic and optical properties [8-12].

The combustion process is characterized by high temperatures, fast heating and short reaction times. These characteristics make the chemical and solution combustion method an attractive synthesis technique for the manufacture of technologically useful materials at a lower cost compared to conventional ceramic processes where some require long heating times and equipment. The products of chemical and solution combustion synthesis are highly reactive, pure and contain minimum level of impurities. Currently, several researchers have employed the combustion method to synthesize a variety of oxide ceramic powders with good success [13,14].

The SrO samples were synthesized as to later incorporate them into the ZnO matrix to investigate their optical properties. The samples were synthesized using solution combustion synthesis and urea as a fuel. This chapter reports on the preparation, structure, chemical composition, electronic states, morphology, reflectance hence absorption behaviour, bandgap and photoluminescence properties of the SrO samples synthesised at 600˚C.

6.2. Experimental:

6.2.1 Preparation of SrO:

Strontium nitrate and urea were used as starting materials. The materials were mixed stoichiometrically according to the following chemical reaction equation:

$$3Sr(NO_3)_2 + 5CH_4N_2O \rightarrow 3SrO + 10H_2O + 5CO_2\uparrow + 8N_2\uparrow \qquad (6.1)$$

In a typical preparation 3.1 g urea, 6.554 g of strontium nitrate and 10 mL of deionized water were mixed together, and stirred for 60 minutes at approximately 80˚C to achieve a homogenous solution. The solution was then poured into a crucible and transferred to a furnace which was pre-set to a synthesis temperature of 600˚C ± 15, for 15 minutes. A white powder formed after the reaction was complete. A typical flame in combustion synthesis technique was not observed. Depicted in figure 6.1 is a graphical representation of this synthesis method.

6.2.2 Characterization:

The structural properties of the SrO powder were analysed using a Bruker D8 Advance powder diffractometer with a Cu-Kα radiation wavelength of 1.54 Å. The elemental composition and

electronic states were analysed using X-ray photoelectron spectroscopy (XPS) using a PHI 5000 Versa probe equipped with monochromatic Al-K radiation
(hv = 1253.6 eV) was conducted. For higher resolution spectra, the hemispherical analyzer pass energy was maintained at 11.3 eV. Measurements were performed using a 1 eV/step (or 45 min acquisition times) binding energies for survey scans from 0 to 1400 eV and 1 eV/step and 20–30 min times for the high-resolution scans. A low energy electron beam was used to achieve charge neutrality on the sample surface. All the absolute binding energies of the photoelectron spectra were corrected with C 1s signal at 284.6 eV.

The morphology and elemental composition of the materials was analysed using a Jeol JSM-7800F field emission scanning electron microscope (FE-SEM) coupled with Oxford Aztec 350 X-Max80 energy-dispersive X-ray spectroscopy (EDS). The particle size and morphology of the SrO sample was confirmed by JEOL ARM200F transmission electron microscope. The diffuse reflectance data was recorded using ultraviolet visible (UV–vis) spectrometer by a Perkin Elmer Lambda 950 UV–Vis. The photoluminescence data was recorded at room temperature using a He-Cd laser at an excitation wavelength of 325 nm.

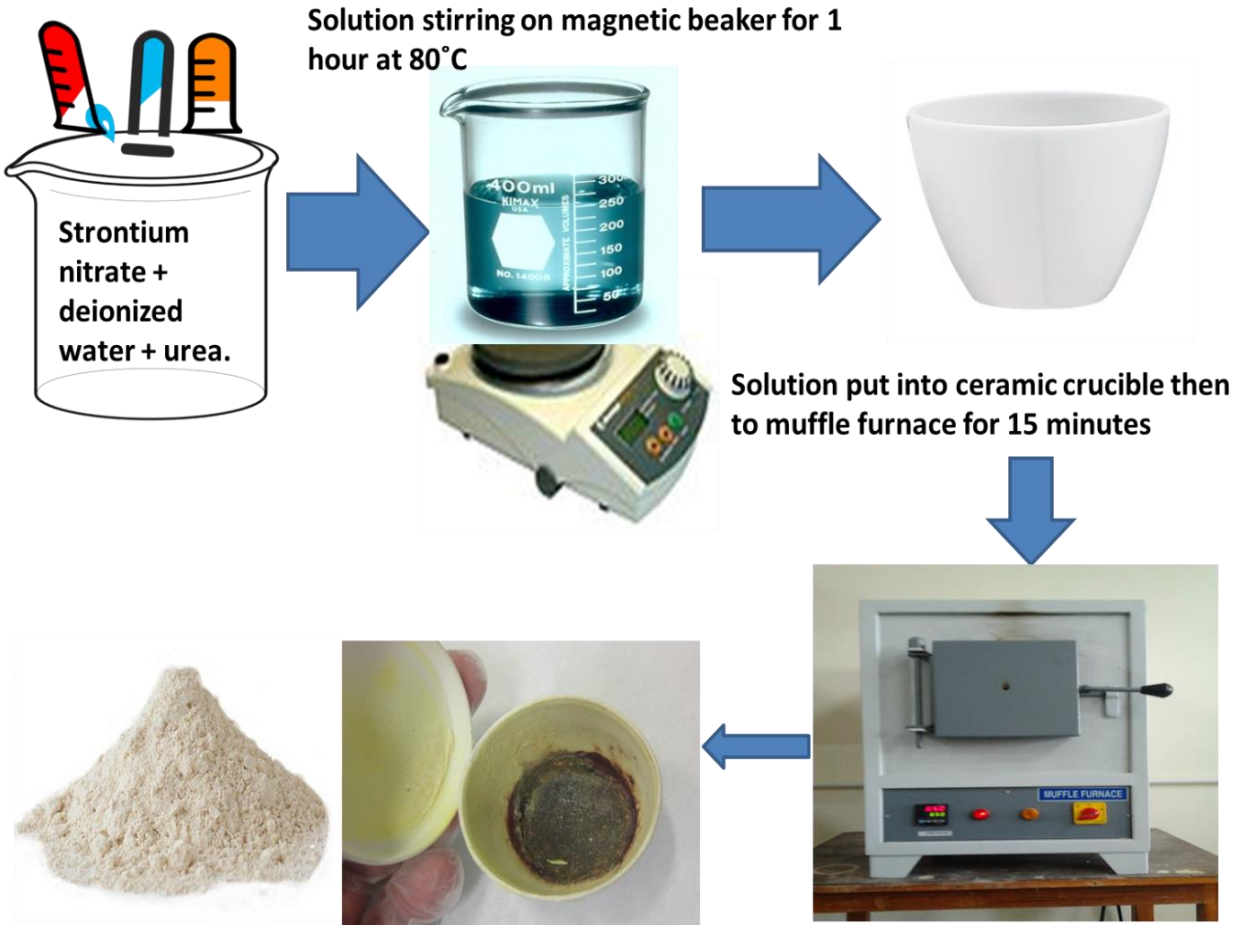

Figure 6.1: Graphical representation for preparation of SrO using solution combustion synthesis method.

6.3 Results and Discussion

6.3.1. Structural Studies

6.3.1.1. XRD Results

Figure 6.2 shows the X-ray diffraction pattern of the SrO mixed phased sample synthesized by solution combustion method at 600˚C. The pattern indicates the presence of three well-defined crystalline phases which are SrO, $Sr(OH)_2$ and $Sr(CO_3)_2$. It is clear that the material is not pure single phase SrO. The most prominent phase observed was $Sr(OH)_2$. The JCPDS reference XRD patterns of $Sr(OH)_2$ and $Sr(CO_3)_2$ were used to determine whether $Sr(OH)_2$ and $Sr(CO_3)_2$ formed instead of SrO since they could have arisen as products from the precusors.

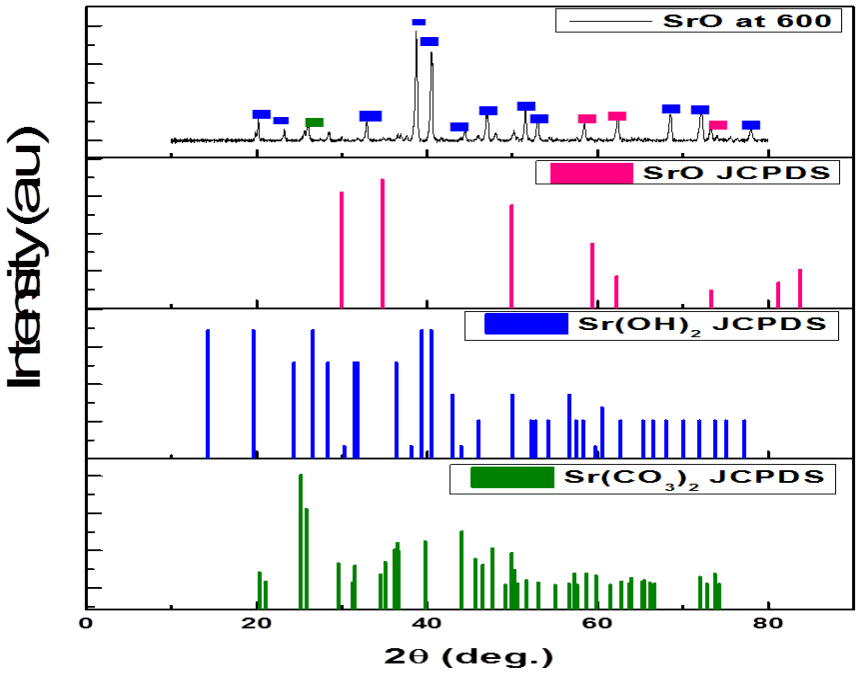

Figure 6.2 : XRD patterns of mixed phase SrO powders synthesized at 600˚C powders using solution combustion method.

6.4. Surface characterization

6.4.1. XPS Results

The elemental composition and the oxidation state of the cations were analysed with a powerful, analytical XPS technique. In fig. 6.3 the survey XPS scan of SrO indicates the presence of strontium, oxygen, fluorine, carbon and scandium corresponding to their energies. Moulder et al [15] reported that the Sr ($3d_{5/2}$) component has a lower binding energy (BE) and higher intensity than those of the Sr ($3d_{3/2}$). The deconvolution of XPS high-resolution scan for the O 1s core level lines show the presence of two different peaks in figure 6.4. The main peak at 536.5 eV is associated with the O 1s in the Sr-O species. The peak at 537.95 eV is believed to be related to the adsorbed oxygen such as carbonates and hydroxyl oxides [15]. Figure 6.5 shows the high-resolution scan for the Sr 3d core level. The Sr-O chemical bonds are commonly classified as very ionic with complete transfer of valence electrons from Sr to O atoms. Two peaks appeared in the Sr 3d spectra, one peak at 139.21 eV resembles the $Sr\text{-}(OH)_2$ bonding and the other peak at 140 eV is attributed to Sr-O bond [15].

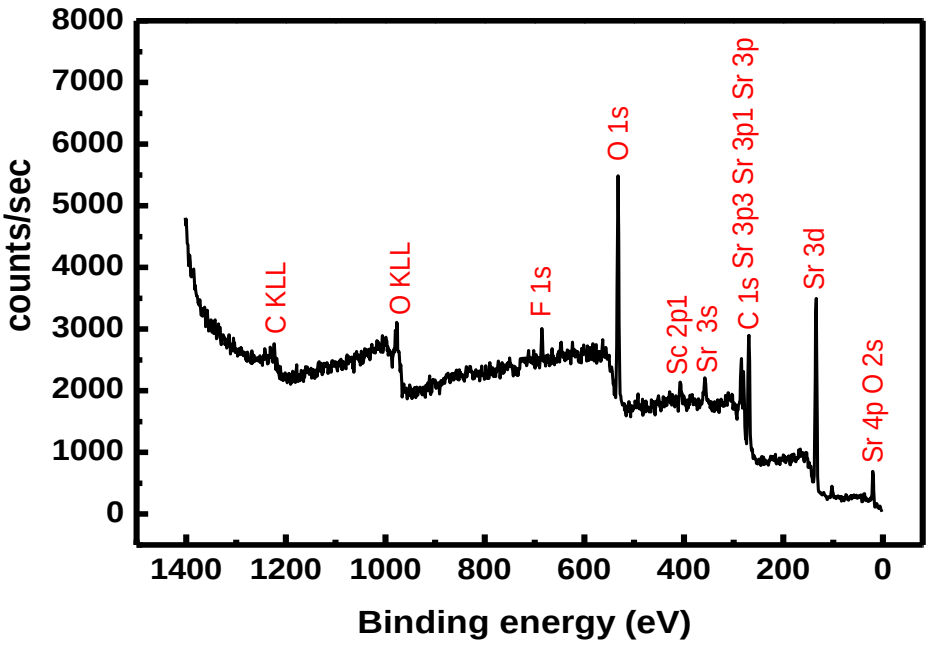

Figure 6.3: XPS wide scan spectrum of mixed phased SrO nanophosphors.

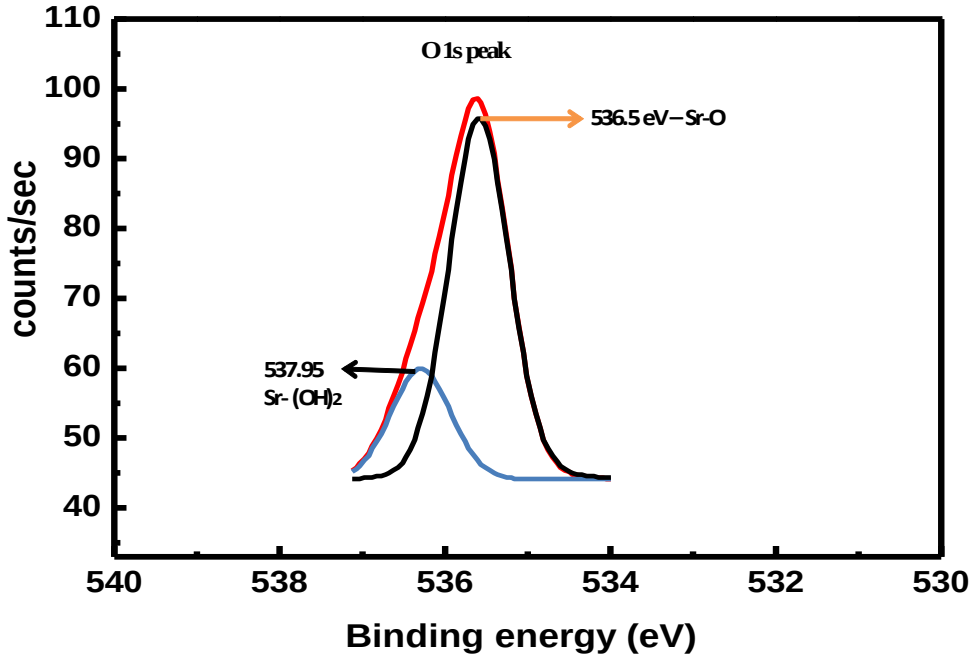

Figure 6.4: XPS high-resolution scan with the deconvolution for the O 1s core energy level.

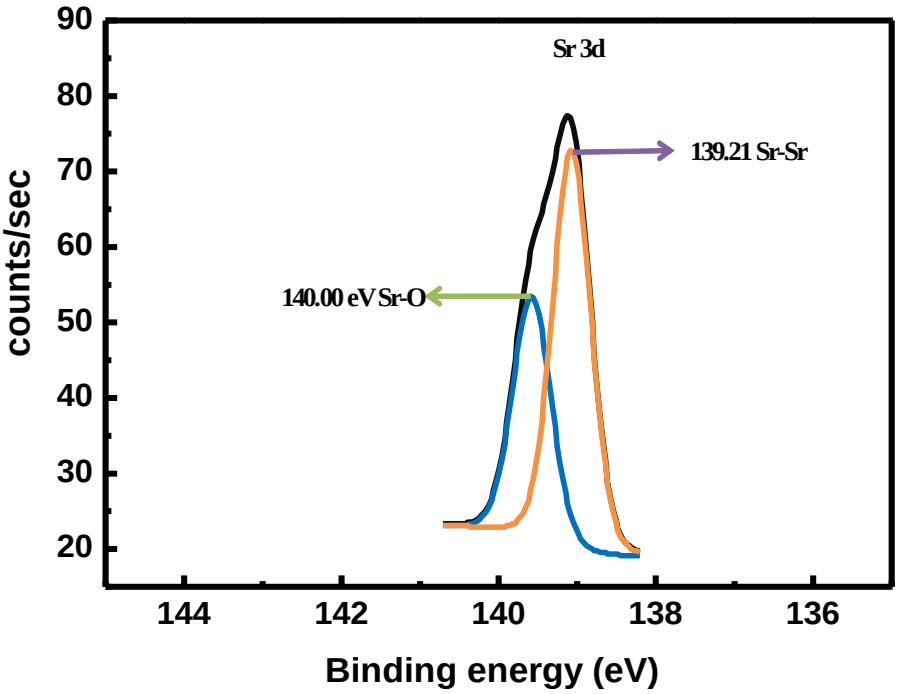

Figure 6.5: XPS high-resolution scan with the deconvolution for the Sr 3d core energy level.

6.4.2. SEM Results

The scanning electron microscopy (SEM) analysis was performed to evaluate the fine-scaled topological features of SrO powder sample. The SEM micrographs at different magnifications are depicted in figure 6.6 (a-d). In figure 6.6 (a & b) it is clear that the morphology results in small and coagulated particles of irregular shapes and different sizes. Pores of different sizes are also observed and are a result of solution combustion synthesis. This is due to the outgassing of the gaseous products of this synthesis method i.e N_2 and CO_2. With respect to figure 6.6 (c & d) the surface morphology of SrO results in large cubical-spherical shapes with a smooth and regular surface. The smooth surface of the phosphor can reduce non-radiation and scattering and is thus beneficial to the luminescent efficiency in application. The dense packed small particles can prevent the phosphor from aging.

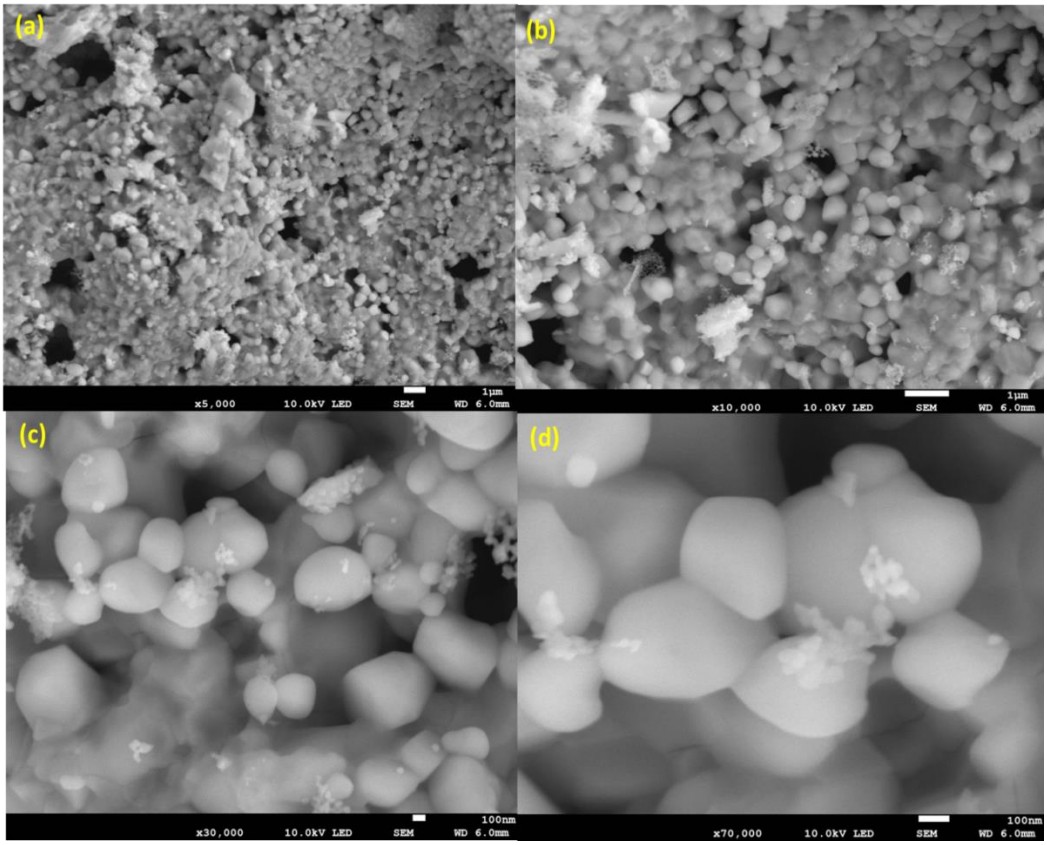

Figure 6.6: SEM images of the mixed phase SrO sample synthesized at 600˚C by solution combustion method.

6.4.3. HR-TEM Results

The HR-TEM micrograph and SAED pattern of SrO NPs are depicted in figure 6.7 (a & b). These were obtained from solution combustion synthesis of one SrO sample, at a synthesis temperature of 600˚C. The HR-TEM images show that the SrO NPs have no definite shape and are aggregated into clusters. At high synthesis temperatures such as 600˚C many neighbouring particles are prone to fuse together to form larger particles. The SAED pattern in figure 6.7 (b) confirms the observation of a large number of nanoparticles observed in figure 6.7 (a) and hence there were many spots within each ring observed due to a large number of particles in figure 6.7 (b).

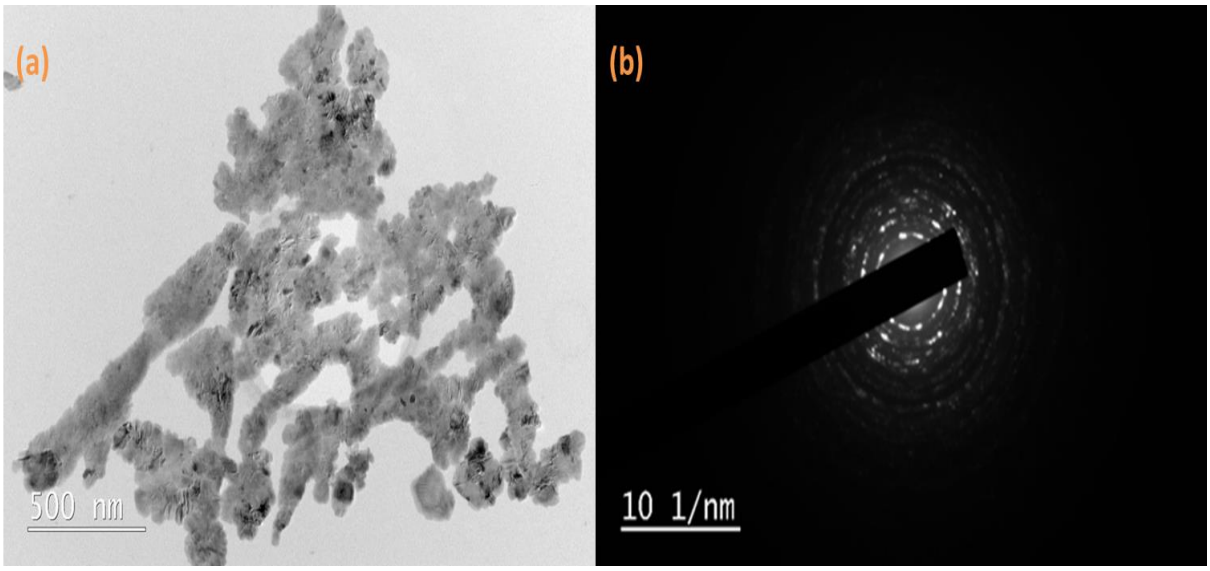

Figure 6.7: Illustration of HR-TEM micrograph and SAED pattern.

6.5. Optical studies:

6.5.1. UV-Vis Results

The diffuse reflectance spectra was measured in the range of 200-800 nm at room temperature and shown in Figure 6.8 (a). The optical bandgap value for the SrO sample synthesized at 600˚C was determined from reflectance spectra using the Kubelka-Munk equation:

$$F(R) = (1-R)^2/2R = k/s \quad (6.2)$$

where, R = reflectance; k = absorption coefficient; s = scattering coefficient; It gives a correlation between the reflectance and the concentrations of absorbing species. The Tauc relation is given as:

$$(F(R)\cdot hv)^2 = A\,(hv - E_g) \quad (6.3)$$

where F(R) is the Kubelka-Munk function, (hv) is the incident photon energy, A is a constant depending on the transition probability and the diffuse reflectance (R) . The Tauc plot method

was used to plot the values of $(F(R)\cdot hv)^2$ vs. (hv) as illustrated in Figure 6.8 (b). This was done in order to determine the optical band gap value of the SrO nanoparticles.

The highest reflectance observed with the SrO sample was at 67%, a significant decrease in reflectance percentage at 66% and 651 nm, an increase in reflectance percentage at 68% and 514 nm, an absorbance peak 493 nm, a curvature at 413 nm, an absorption edge at 356 nm and a reflectance peak at 298 nm. The bandgap of this sample was calculated from the absorption edge at 356 nm and it was 3.32 eV. The theoretical bandgap of SrO is 5.71 eV. There is a significant difference between the theoretical and experimental bandgap values, the difference in bandgap can be attributed to the extra phases present which can have different bandgaps within the material.

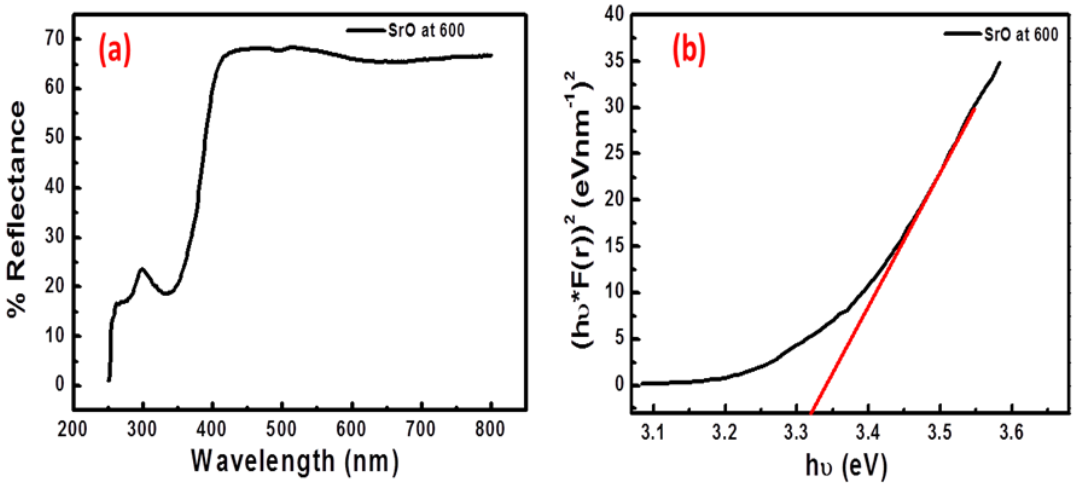

Figure 6.8: UV-Vis reflectance spectra and bandgap graph for the SrO sample synthesized at 600˚C.

6.5.2. Photoluminescence Results:

Figure 6.9 is the photoluminescence spectrum of the mixed phase SrO sample synthesized at 600˚C, the excitation used was from the He-Cd laser source with a wavelength of 325 nm. From the XRD results it was observed that the SrO sample has mixed crystalline phases and the prominent phase being $Sr(OH)_2$. From the XPS results of the high-resolution scan, the deconvolution for the O 1s core spectra revealed that the most prominent phase of the SrO mixed phase sample is in fact SrO at 536.5 eV. From that it can be deduced that the PL emission peaks are in fact from SrO and that $Sr(OH)_2$ because of its peak is significantly less than SrO, is not luminescent.

The PL spectrum possesses ultraviolet and deep level emission peaks. There is a narrow peak in the UV region at 397 nm and a broad peak in the visible region at 750 nm.

Figure 6.9 (b) are the deconvoluted peaks of the UV region emission peak at 397 nm. The deconvoluted peaks are approximately at 379, 404 and 438 nm. These deconvoluted emission peaks are attributed to electron mediated defect levels in the bandgap.

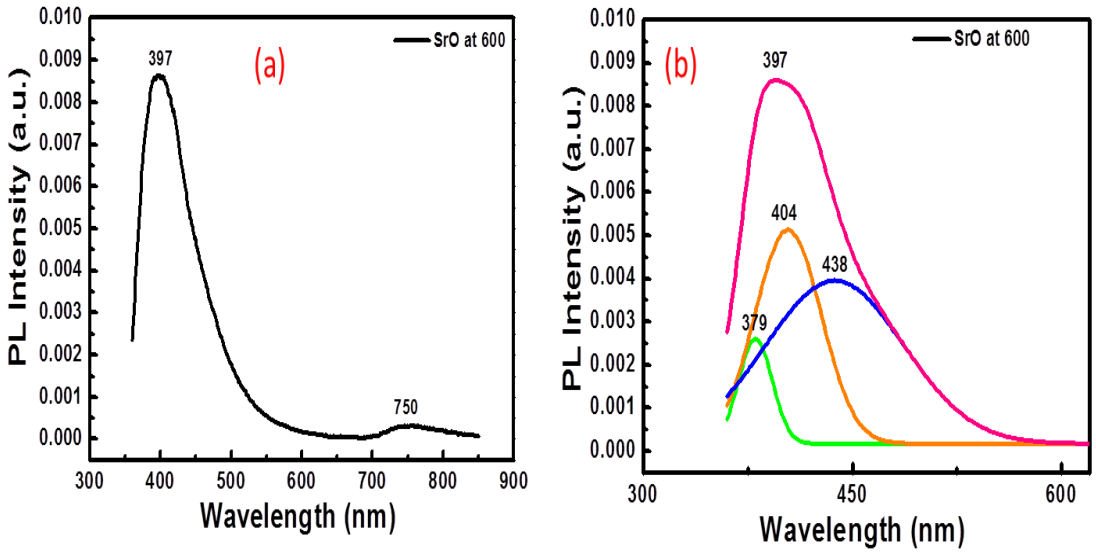

Figure 6.9 (a-b): Photoluminescence and the deconvuluted spectra of mixed phase SrO nanophosphor synthesized via solution combustion method.

6.6. Conclusion:

The XRD patterns of the SrO sample indicates the presence of three crystalline phases which are SrO, $Sr(OH)_2$ and $Sr(CO_3)_2$ depicted in figure 6.2. The prominent phase was $Sr(OH)_2$.

From the XPS results of the high-resolution scan, the deconvolution for the O 1s core spectra revealed that the most prominent phase of the SrO mixed phase sample is in fact SrO at 536.5 eV. From this, it can be suggested that the PL emission peaks are in fact from SrO and not $Sr(OH)_2$. The $Sr(OH)_2$ peak has significantly less intensity than SrO therefore it can possibly be suggested that $Sr(OH)_2$ it is not luminescent.

The bandgap of this sample was calculated from the absorption edge at 356 nm and it was 3.32 eV. The theoretical bandgap of SrO is 5.71 eV. There is a significant difference between the theoretical and experimental bandgap values. The difference in bandgap can be attributed to the fact that a pure phase of SrO was not obtained and a mixed phase material emerged so the bandgap possess many phases as well hence it differs from the expected theoretical value.

References:

[1] Vu J., Guo H., Cheng B., J. Solid State Chem., 179 (2006), 800.

[2] Li S., Zhang H., Xu J., Yang D., Mater. Lett., 59 (2005),420.

[3] Voosuk B., Krasae P., Puttasawat B., Udomsap P., Viriya-Empikul N., Faungnawakij K., Chem. Eng. J., 162 (2010), 58.

[4] Joyce A.O., Strontium, Minerals Yearbook. Volume 1. Metals and Minerals, U.S., Bureau of Mines, 1992, 11323.

[5] Ozuna O., Hirata G.A., Kittrick M.C., J. Phys. Condens. Mat., 16 (2004), 2585.

[6] Chandrappa K.G., Venkatesha T.V., Nayana K.O., Punithkumar M.K., Mater. Corros., 63 (2012), 445.

[7] Kingsley J.J., Pederson L.R., Mater. Lett., 18 (1993), 89.

[8] Chandran R.G., Patil K.C., Mater.Lett.,10(1990), 291.

[9] Manoharan S.S., Patil K.C., J. Am. Ceram. Soc., 75 (1992), 1012.

[10] Li F., Hu, J.L.l., Zhang L.D., Chen G., J. Nucl. Mater., 300 (2002), 82.

[11] Patil K.C., Aruna S.T., Mimami T., Curr. Opin. Solid State, Mat., 6 (6) (2002), 507.

[12] Biamino S., Badini C., J. Eur. Ceram. Soc., 24 (2004), 3021.

[13] Chick L.A., Pederson L.R., Maupin G.D., Bates J.L., Thomas L.E., Exarhos G.H., Mater. Lett., 10 (1990), 6.

[14] Sharma S.K., Pitale S.S., Malik P.M., Dubey R.N., Qureshi M.S., Ojha S.,Physica B,405(2010), 866.

[15] Moulder J.F.F, Stickle W.F., Sobol P.E., Bomben K.D. (1995) in: Chastain J, King RC JR (eds) Handbook of X-ray Photoelectron Spectroscopy. Physical Electronics Inc, Minnesota.

Chapter 7: The impact of varied concentrations on different structures, composites, morphologies and optical properties of Mg-doped ZnO samples.

7.1. Introduction

The synthesis of nanostructured oxide materials has attracted considerable attention, due to their thermal and chemical stability among other things. Oxide semiconductor nanostructures have been widely investigated in recent years because of their excellent optical properties [1–3]. The metal oxides are extremely important technological materials for use in electronic, chemical or mechanical industries, as well as in relevant technologies, including superconductors, catalysts, magnetic materials, structural, and engineering materials [4]. Due to their excellent nonlinear coefficient and low leakage current, they have been used in electrical and electronic systems such as surge protection devices for many years [5].

In recent years, researchers have focused more on the synthesis of ultra-fine particles of ZnO and MgO due to their application in advanced technologies. Magnesium oxide (MgO) is one of the most useful and promising materials in the field of nanoscience; the large surface area to volume ratio and the presence of reactive sites on the surface make MgO nanoparticles suitable for uses in a number of organic heterogeneous catalysts. Other possible fields of application are gas and humidity sensors and cryosurgery, due to low cost, electro-stability, nontoxic properties of MgO nanoparticles [6].

Mg-doped ZnO materials are found to be a single phase alloy in a wide range of Mg doping levels. By alloying with MgO, the band gap of the ternary alloy $Mg_xZn_{1-x}O$ could be tuned into extremely short wavelength regions [12–14].

ZnO phosphors exhibit tunable photoluminescence (PL) in a wide range from blue to green and orange through chemical doping [15]. ZnO at nanoscale exhibits some novel physical properties which are substantially different from their bulk counterparts. The doping of Mg in ZnO permits the band gap to be tailored and decrease the oxygen vacancies and electron density [16]. Therefore Mg doping will have considerable influence on the optical properties of ZnO and it paves the way to obtain tunable optical and electrical properties. Recently, many researchers have reported the formation of $Mg_xZn_{1-x}O$ nanostructures with different synthesis methods [17-19].

This chapter reports on the preparation, structure, morphology, and reflectance and hence absorption behaviour, bandgap and photoluminescence properties of the Mg doped ZnO, MgO and ZnO composite samples, which were synthesised at 600˚C via solution combustion method using urea as a fuel.

7.2 Experimental

7.2.1 Preparation of Mg doped ZnO samples

Magnesium nitrate, zinc nitrate and urea were used as starting materials. The materials were mixed stiochiometrically according to the following chemical reaction equation:

$$3Mg(NO_3)_2(H_2O)_6 + 3Zn(NO_3)_2(H2O)_6 + 11CH_4N_2O \rightarrow 3Mg_xZn_{1-x}O + 58H_2O + 11CO_2\uparrow + 17N_2\uparrow \quad (7.1)$$

The masses of the samples were calculated according to the following ratio $Mg_xZn_{1-x}O$,(x 0.2, 0.4, 0.5, 0.6, 0.7, 0.8 and 1). In a typical preparation where x = 0.2, 3.0 g of urea, 3.24167 g of zinc hexahydrate nitrate and 0.69857 g of magnesium hexahydrate nitrate were dissolved in 10 mL of deionized water by stirring for 60 minutes at approximately 80˚C, to achieve a homogenous solution. The solution in a crucible was then transferred to a furnace which was pre-set to a synthesis temperature of 600˚C ± 15, for 15 minutes. A white powder was formed after the reaction was complete. A typical flame in combustion synthesis technique was not observed. Depicted in figure 7.1 is a graphical representation of this synthesis method.

7.2.2 Characterization

The structural properties of the powder samples were analysed using a Bruker D8 Advance powder diffractometer with a Cu-Kα radiation wavelength of 1.54 Å. The elemental composition and electronic states were analysed using a X-ray photoelectron spectroscopy (XPS) using a PHI 5000 Versa probe equipped with monochromatic Al-K radiation (hv = 1253.6 eV) was conducted. For higher resolution spectra, the hemispherical analyzer pass energy was maintained at 11.3 eV. Measurements were performed using a 1 eV/step (or 45 min acquisition times) binding energies for survey scans from 0 to 1400 eV and 1 eV/step and 20–

30 min times for the high-resolution scans. A low energy electron beam was used to achieve charge neutrality on the sample surface. All the absolute binding energies of the photoelectron spectra were corrected with C 1s signal at 284.6 eV.

The morphology and elemental composition of the materials was analysed using Jeol JSM-7800F field emission scanning electron microscope (FE-SEM) coupled with Oxford Aztec 350 X-Max80 energy-dispersive X-ray spectroscopy (EDS). The particle morphology and crystalline structure of the samples was further confirmed by JEOL ARM200F transmission electron microscope. The diffuse reflectance data was recorded using ultraviolet visible (UV–vis) spectrometer by a Perkin Elmer Lambda 950 UV–Vis. The photoluminescence data was recorded at room temperature using a 325 nm He-Cd laser as excitation source.

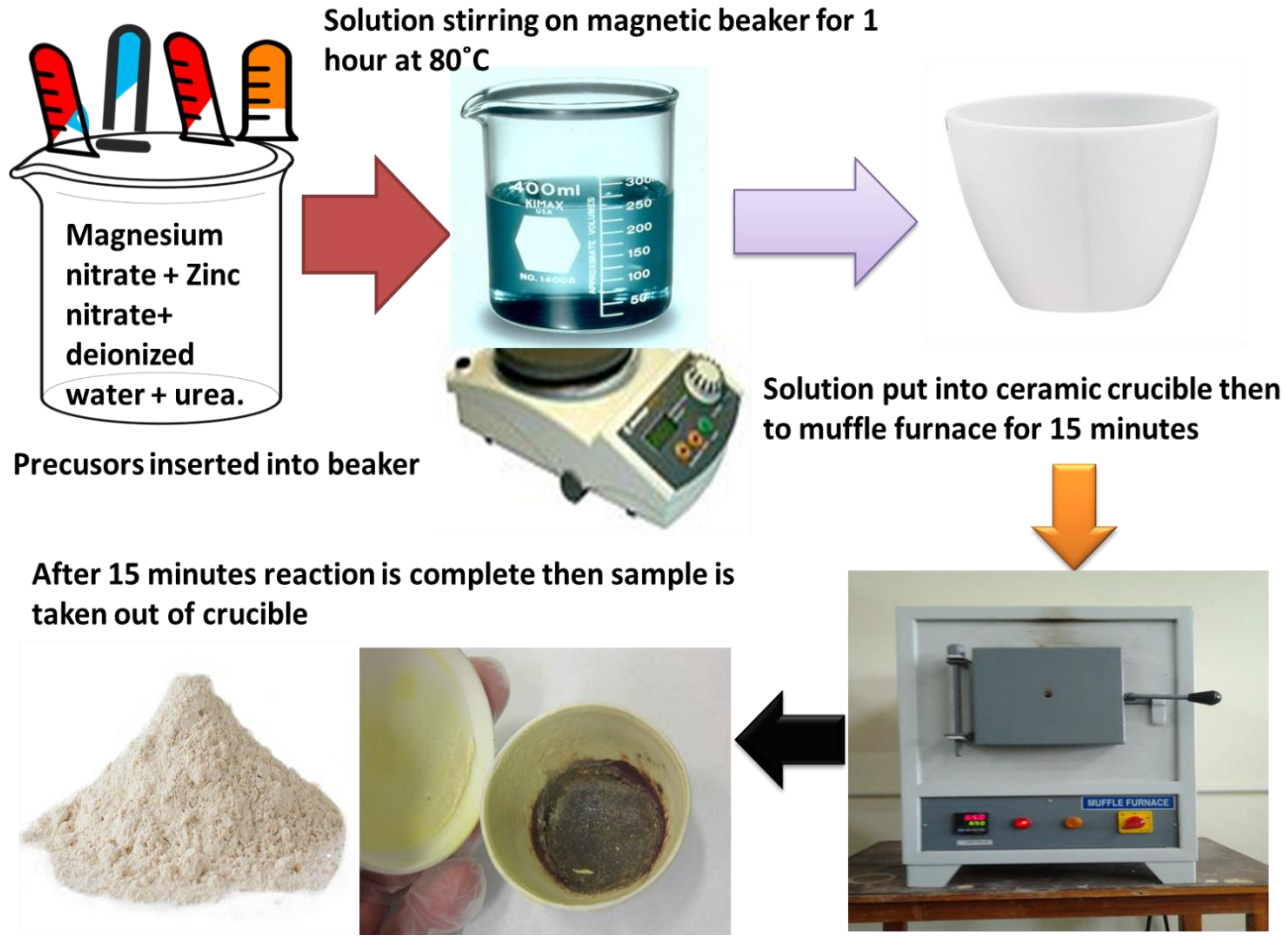

Figure 7.1: Graphical representation for the preparation of Mg doped ZnO samples and composites using solution combustion synthesis method.

7.3. Results and Discussion

7.3.1. Structural Studies

Figure 7.2. is the structure of the combination of the proposed system when ZnO and MgO are brought together and synthesized via solution combustion synthesis method to obtain the following relation $Mg_xZn_{1-x}O$.

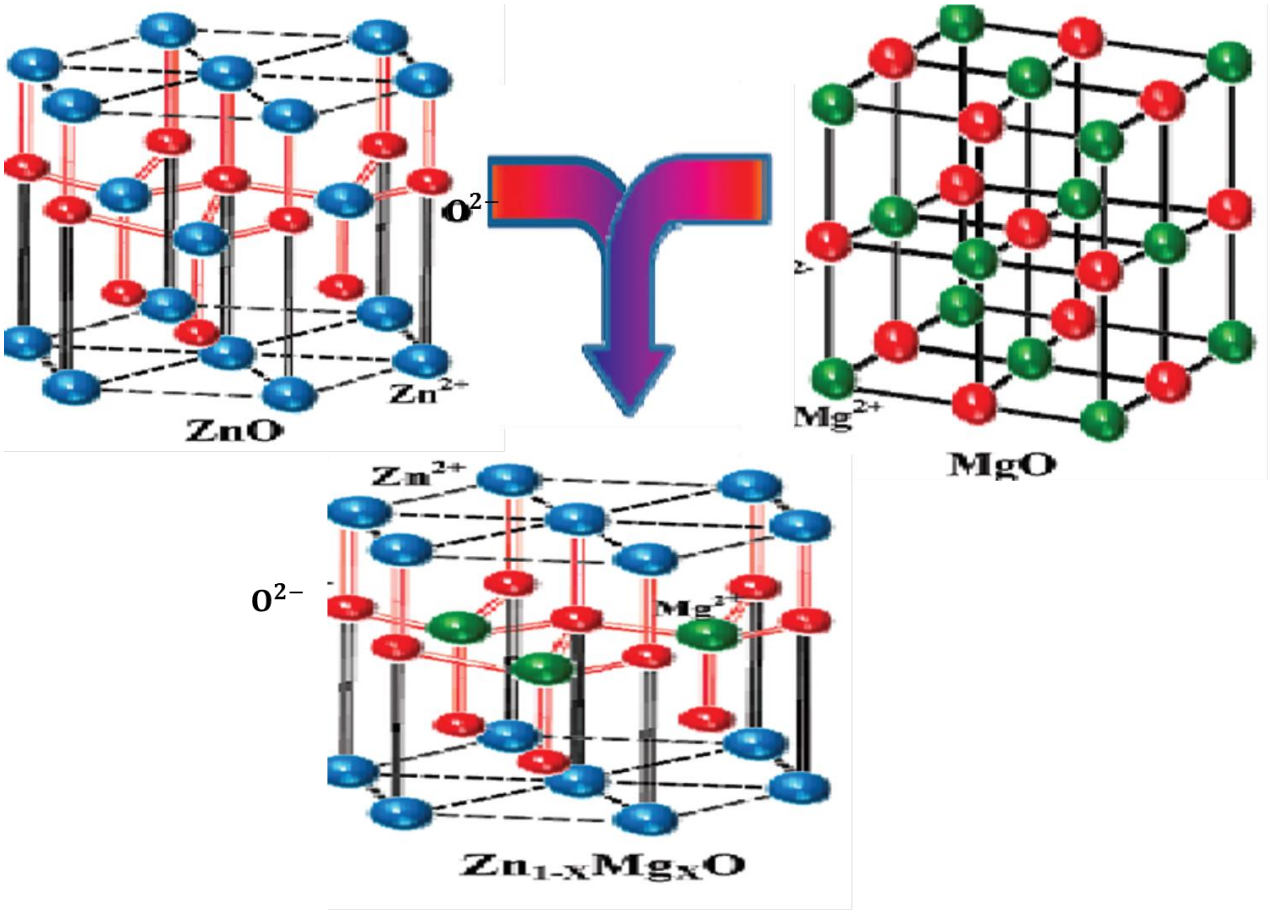

Figure 7.2: Illustration of the combination of MgO and ZnO in this relation $Mg_xZn_{1-x}O$ by solution combustion synthesis method.

7.3.1.1. XRD Results

The XRD patterns depicted below are only for x = 0.2, 0.7 and the composite of MgO-ZnO. These XRD patterns reveal the presence of two well-defined crystalline phases which are MgO and ZnO. From these XRD patterns it can be deduced that Mg doped ZnO phosphor powders were successfully synthesized with the exception that both phases of MgO and ZnO being observed.

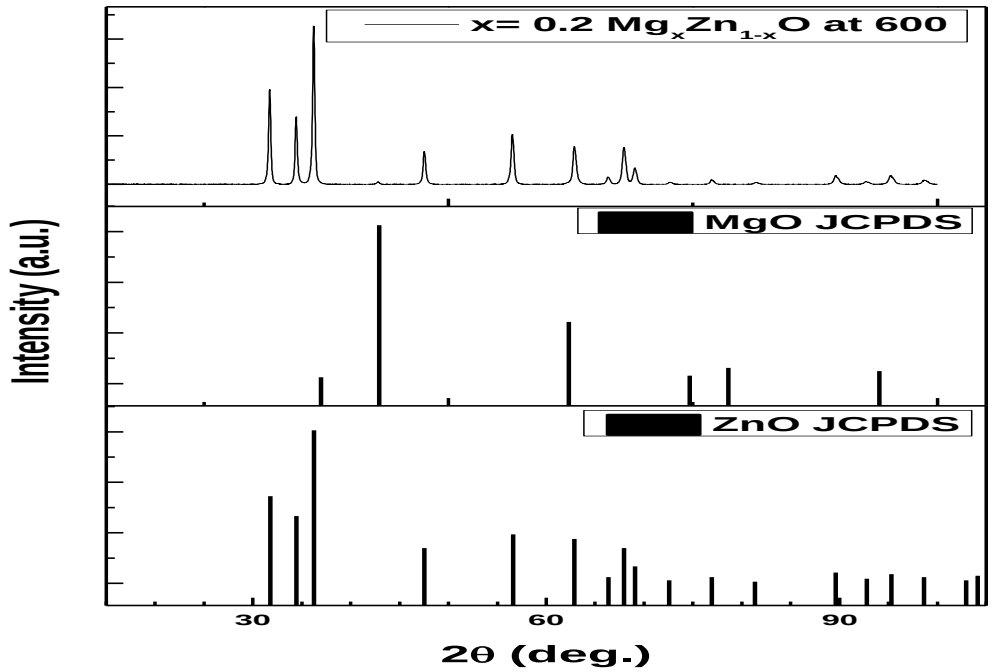

Figure 7.3 (a): XRD patterns of mixed phase $Mg_{0.2}$ $Zn_{0.8}O$ powders synthesized at 600˚C powders using solution combustion method.

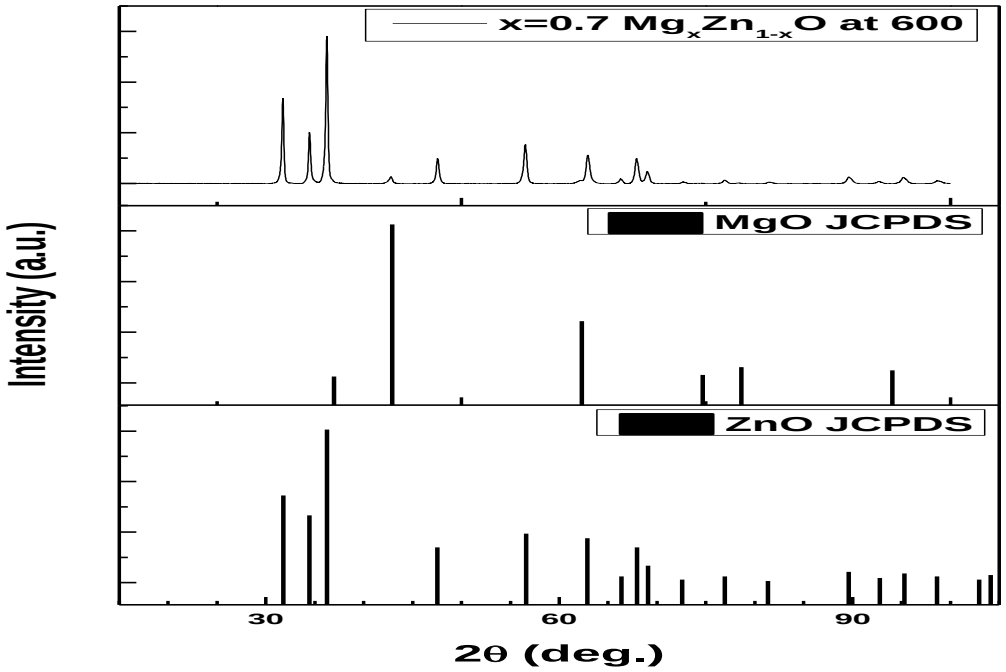

Figure 7.3 (b): XRD patterns of mixed phase $Mg_{0.7}$ $Zn_{0.3}O$ powders synthesized at 600˚C powders using solution combustion method.

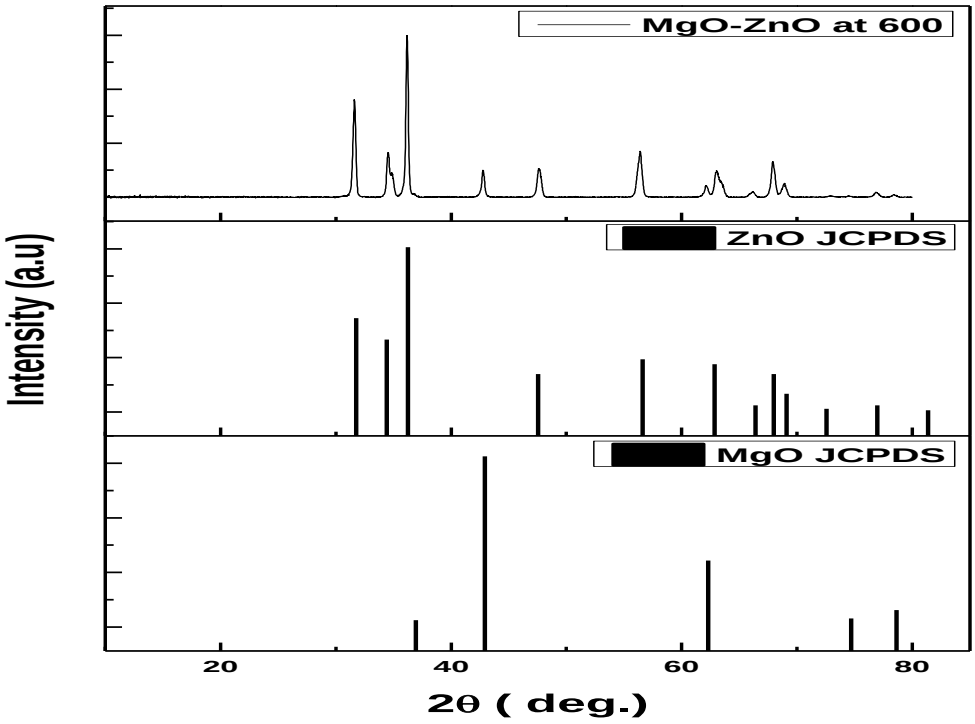

Figure 7.3 (c): XRD pattern of composite of MgO-ZnO powder synthesized at 600˚C powders using solution combustion method.

7.3.1.2. FTIR Results:

Figure 7.4 (a) and (b) are the FTIR spectra of MgO and ZnO. Figure 7.4 (c) is the FTIR spectra of samples $Mg_{0.2}Zn_{0.8}O$ and composite MgO-ZnO. In figure 7.4 (c) the Zn-O peaks for Mg doped ZnO samples such as $Mg_{0.2}Zn_{0.8}O$ appeared at 565 cm^{-1} which is a higher wavenumber in contrast to pure ZnO which was observed at 462 cm^{-1}. Although we observed a material forming two phases with regards to the XRD results there could also be doping where there's an incorporation of Mg^{2+} into the ZnO matrix. The intensities of the Zn-O peaks at 488 and 565 cm^{-1} gradually decrease with the increase in the concentration of the Mg ion. There is a narrow band at 1381 cm^{-1} and is attributed to the bending vibration of absorbed water molecule and surface hydroxyl group (-OH). A broad band located at 2366 cm^{-1} is due to O-H stretching vibration of absorbed water molecule and surface hydroxyl group. This is due to the aerial adsorptions of water molecules onto the MgO surface coming from the atmospheric moisture [20].

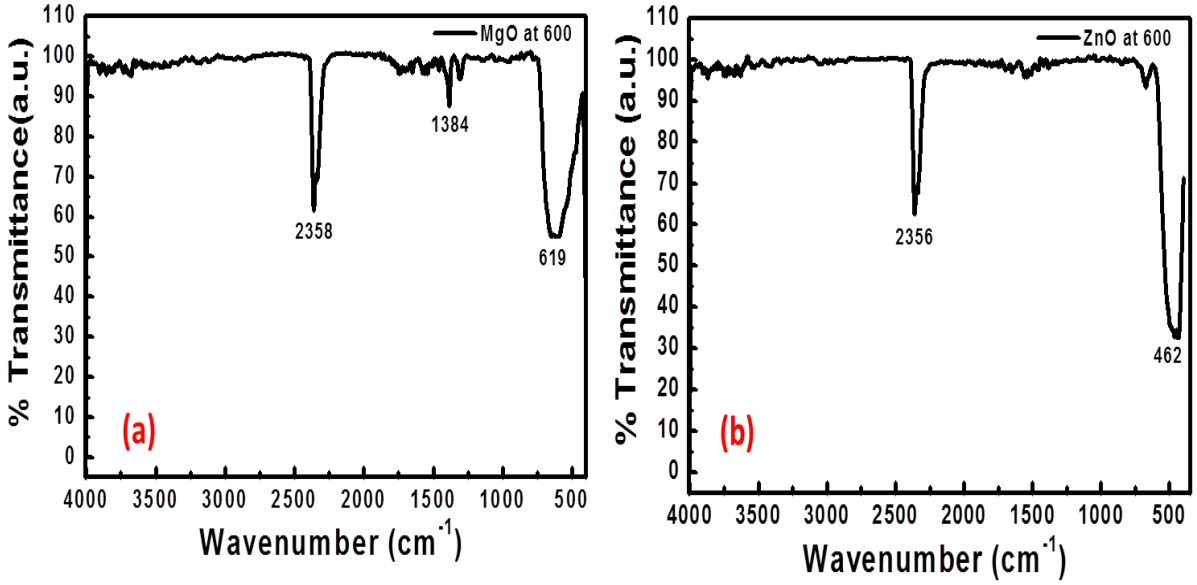

Figure 7.4 (a-b): The FTIR spectra of MgO and ZnO synthesized at 600˚C by solution combustion method.

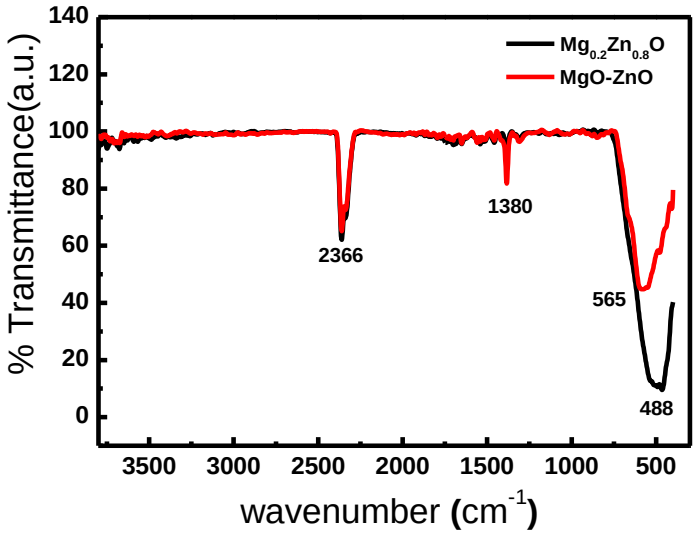

Figure 7.4 (c): The FTIR spectra of Mg doped ZnO where x=0.2 and MgO-ZnO composite synthesized at 600˚C by solution combustion method.

7.3.1.3. XPS Results:

The elemental composition and the oxidation state of the cations were analysed with a powerful, analytical XPS technique. In figure 7.5 the survey scan of the MgO-ZnO composite indicated the presence of magnesium, zinc, oxygen, mercury and calcium corresponding to their energies. To understand the chemical bonding in the composite MgO-ZnO nanopowders, the core levels of Zn 2p, Mg 2p and O 1s states were examined and are shown in figure 7.6 (a-c) respectively. In figure 7.6 (a) the O 1s peak is deconvoluted into three peaks located at 531, 531.94 and 532.1 eV. The 531 eV peak corresponds to the O-Zn bond, the 531.94 eV peak is associated with O^{2-} ions in oxygen deficient regions within the matrix of ZnO and MgO, while the 532.1 eV peak is correlated to H/H_2O species [21-23].

In figure 7.6 (b) the peaks at 1021 and 1023 eV binding energies are attributed to the $2p_{3/2}$ and $2p_{1/2}$ core levels of Zn ions confirming the divalent Zn ions [24]. The Mg 2p spectrum as shown in fig. 7.6 (c) indicates the coexistence of Mg^{2+} in the MgO-ZnO composite at binding energy of 50 eV major peak [25].

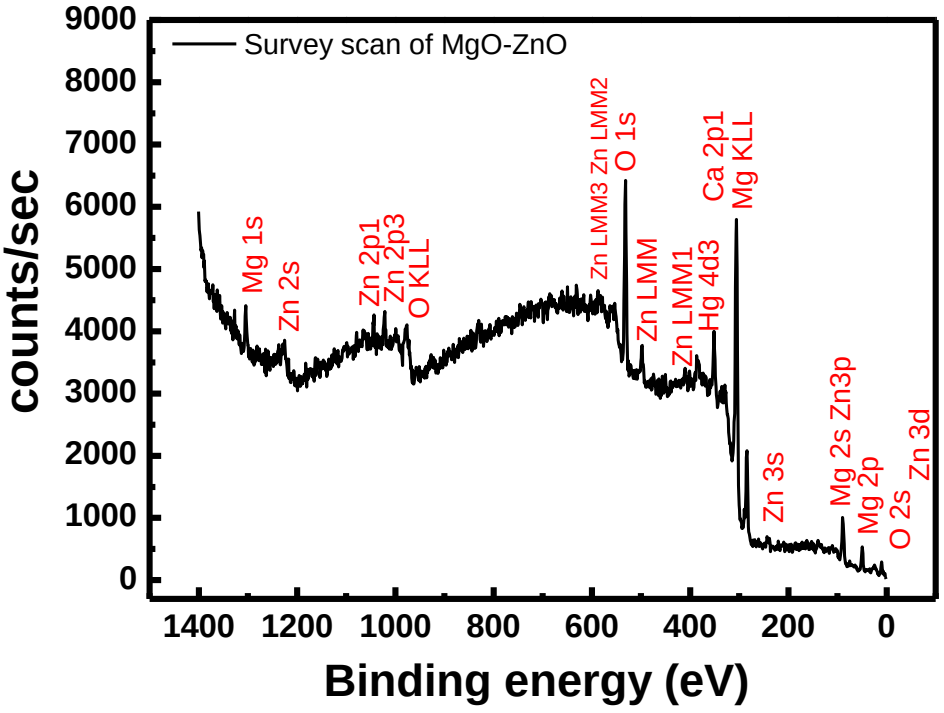

Figure 7.5: XPS wide scan spectrum of MgO-ZnO composite nanophosphors.

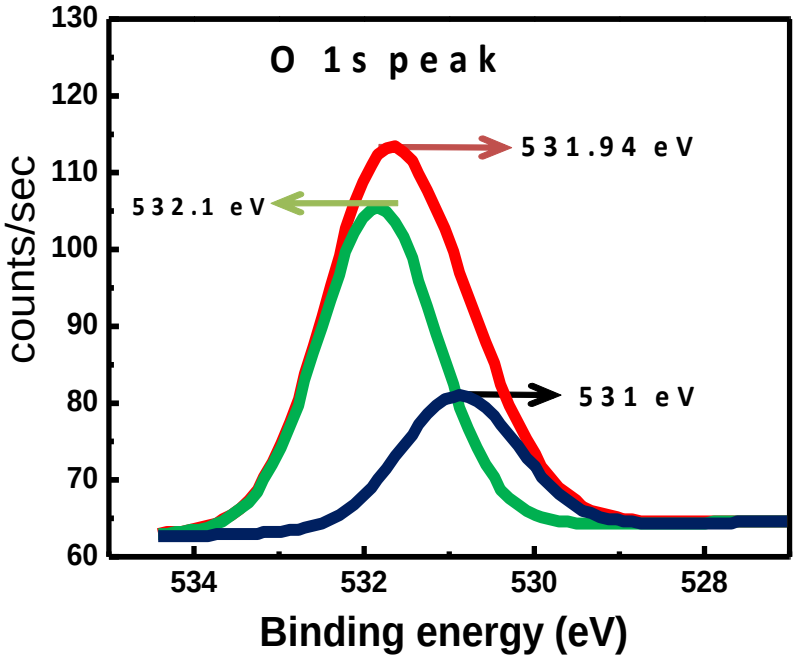

Figure 7.6 (a) : XPS high-resolution scan with the deconvolution for the O 1s core level.

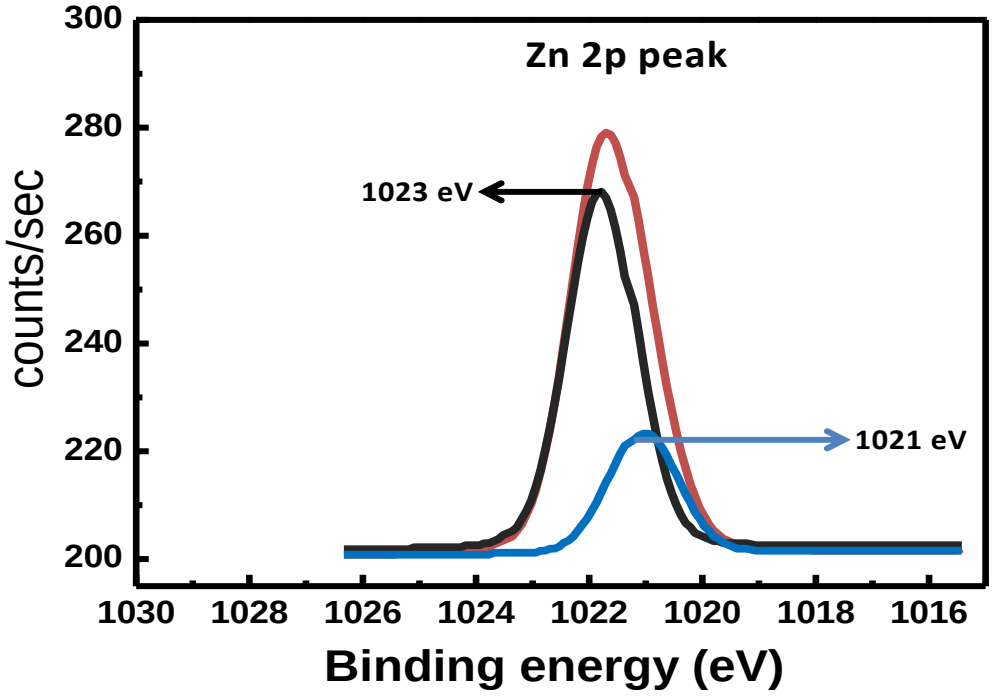

Figure 7.6 (b): XPS high-resolution scan with the deconvolution for the Zn 2p core level.

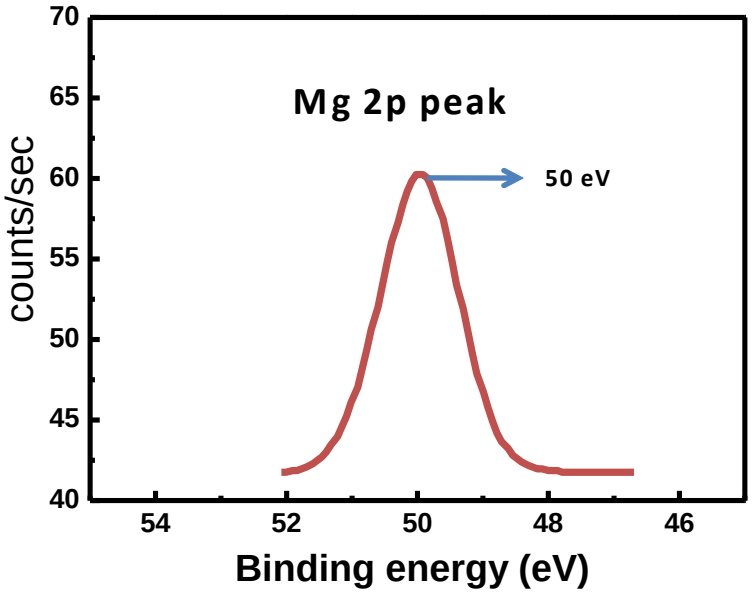

Figure 7.6 (c): XPS high-resolution scan for the Mg 2p core level.

7.3.2. SEM and EDS Results:

7.3.2.1 Particle Morphological and Chemical Composition characteristics

The scanning electron microscopy (SEM) and energy dispersive X-ray spectroscopy (EDS) analysis were performed to evaluate respectively, the fine-scaled topological features and chemical composition of Mg doped ZnO powder samples. The SEM micrographs at different magnifications and corresponding EDS spectra are depicted in figure 7.7 (a-k). It was observed in all the SEM images that the microstructures possess well-defined shapes with different particle sizes, without any significant change in homogeneity. In figure 7.7 (a-d) for $Mg_{0.2}Zn_{0.8}O$ the particle's morphology is different sizes of pyramids clustered together to form flowers with spherical balls grouped together on the sides.

In figure 7.7 (e-h) the SEM images depicted are of the composite of MgO-ZnO. The particle's morphology in these images is particles of different sizes of triangles grouped together in the shape of a cauliflower.

In the EDS spectra shown in figure 7.7 (a and e) all the expected elements present in the samples were observed these include magnesium, zinc and oxygen. The carbon peak can be attributed to the carbon tape on which the sample was mounted. The weight percentages observed of the elements on the surface of the samples are as follows for the sample

$Mg_{0.2}Zn_{0.8}O$, zinc it's 72%, oxygen it's 20% and lastly for magnesium it's 8%. For the MgO-ZnO composite sample magnesium it's 37.68%, oxygen 29.47% and lastly for zinc 29.47%. With regards to the $Mg_{0.2}Zn_{0.8}O$ sample the theoretical value for the elements present in the sample are as follows: zinc 64.27%, oxygen 19.65% and magnesium 4.60%. Lastly for the MgO-ZnO composite sample: zinc 53.73 %, oxygen 13.15% and magnesium 19.97%. These results are in good correlation to the obtained experimental ones.

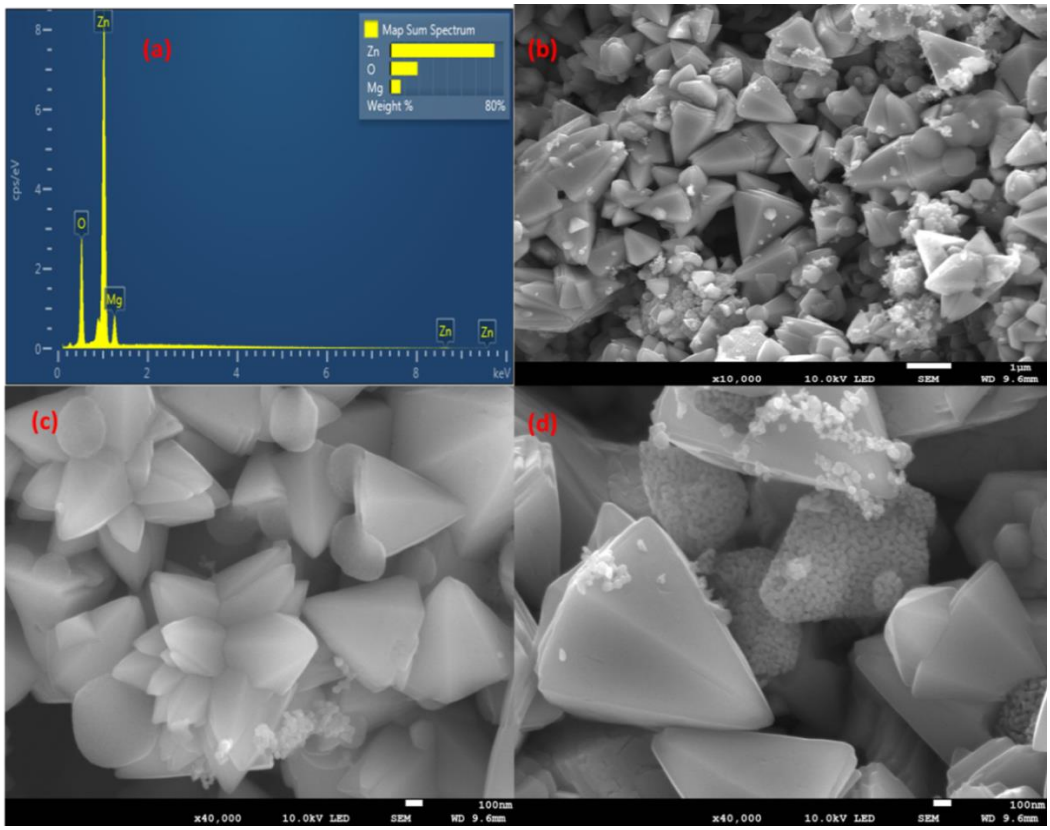

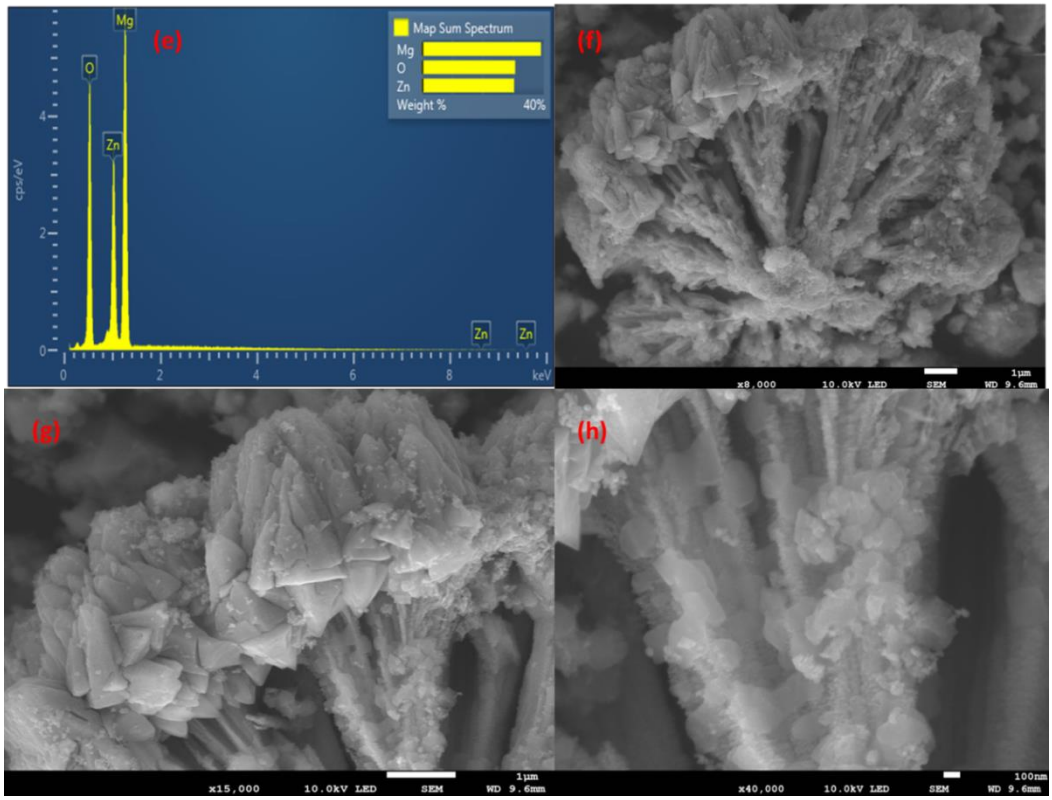

Figure 7.7: SEM images and EDS spectra of samples $Mg_{0.2}Zn_{0.8}O$ (a-d) and MgO-ZnO (e-h) composite.

In the SEM image discussions above, it was observed that the different ratios of Mg ion and ZnO in the system of $Mg_xZn_{1-x}O$ yield different particle shapes and morphology. Figure 7.8 depicts a schematic illustration of the formation of $Zn_{1-x}Mg_xO$ nanomaterials. Starting from the product when it leaves the combustion furnace to the morphology that is later observed.

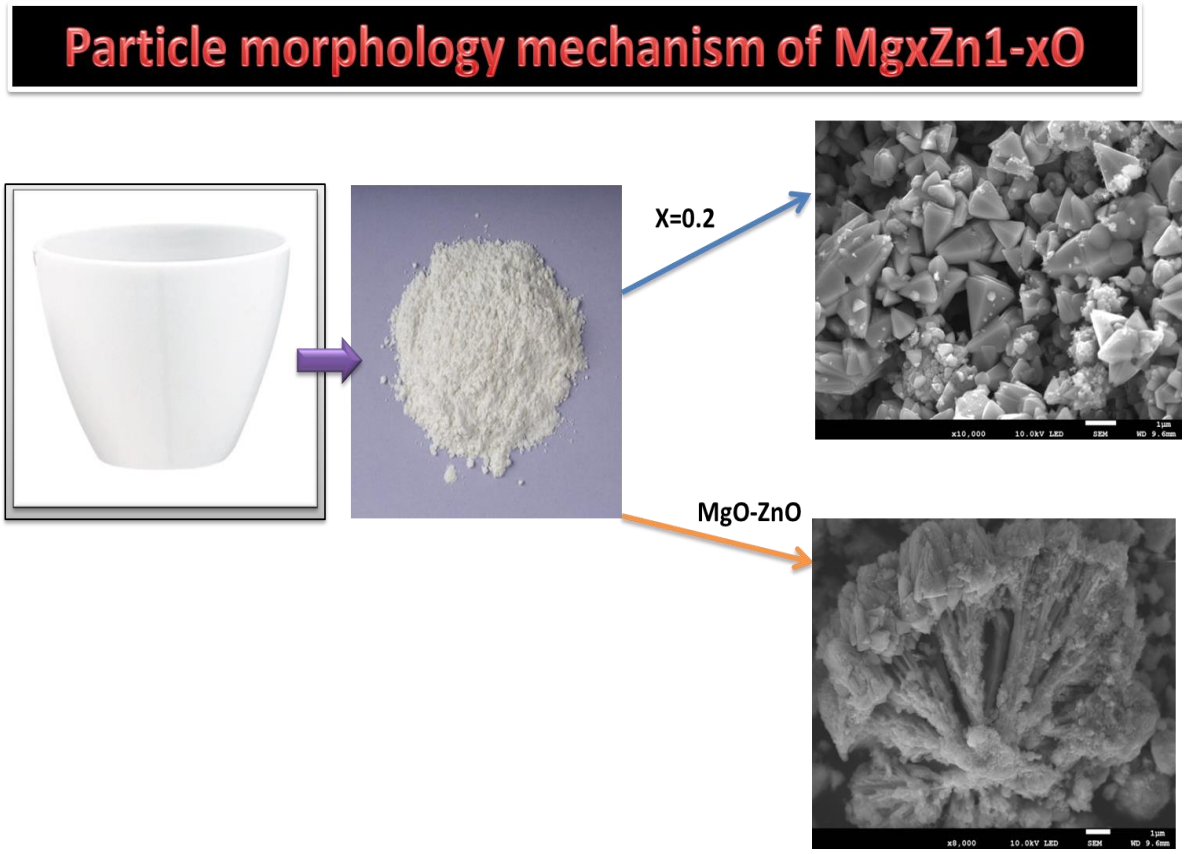

Figure 7.8: Schematic illustration of the formation of $Zn_{1-x}Mg_xO$ nanomaterials.

7.3.3. HR-TEM Results

The HR-TEM micrograph and SAED pattern are of $Mg_{0.4}Zn_{0.6}O$. The NPs are depicted in figure 7.9 (a). The HR-TEM micrograph and SAED pattern were obtained from solution combustion synthesis of the x= 0.4 $Mg_{0.4}Zn_{0.6}O$ sample, at a synthesis temperature of 600˚C. The HR-TEM images show that the NPs are spherically shaped and aggregated into clusters. At high synthesis temperatures such as 600˚C many neighbouring particles are prone to fuse together to form larger particles.

The SAED pattern in figure 7.9 (b) confirms the observation of a large number of nanoparticles observed in figure 7.9 (a) and hence there were many spots within each ring observed due to a large number of particles in figure 7.9(b). For the $Mg_{0.4}Zn_{0.6}O$ sample the ZnO and MgO ring patterns were superimposed at identical scale and this matched well with almost all the rings, suggesting there are a mixture of ZnO and MgO particles in the sample. Some spots are slightly off - this could be due to strain or dopants affecting the interplanar spacings or the use of the small angle approximation when analysing these ring patterns.

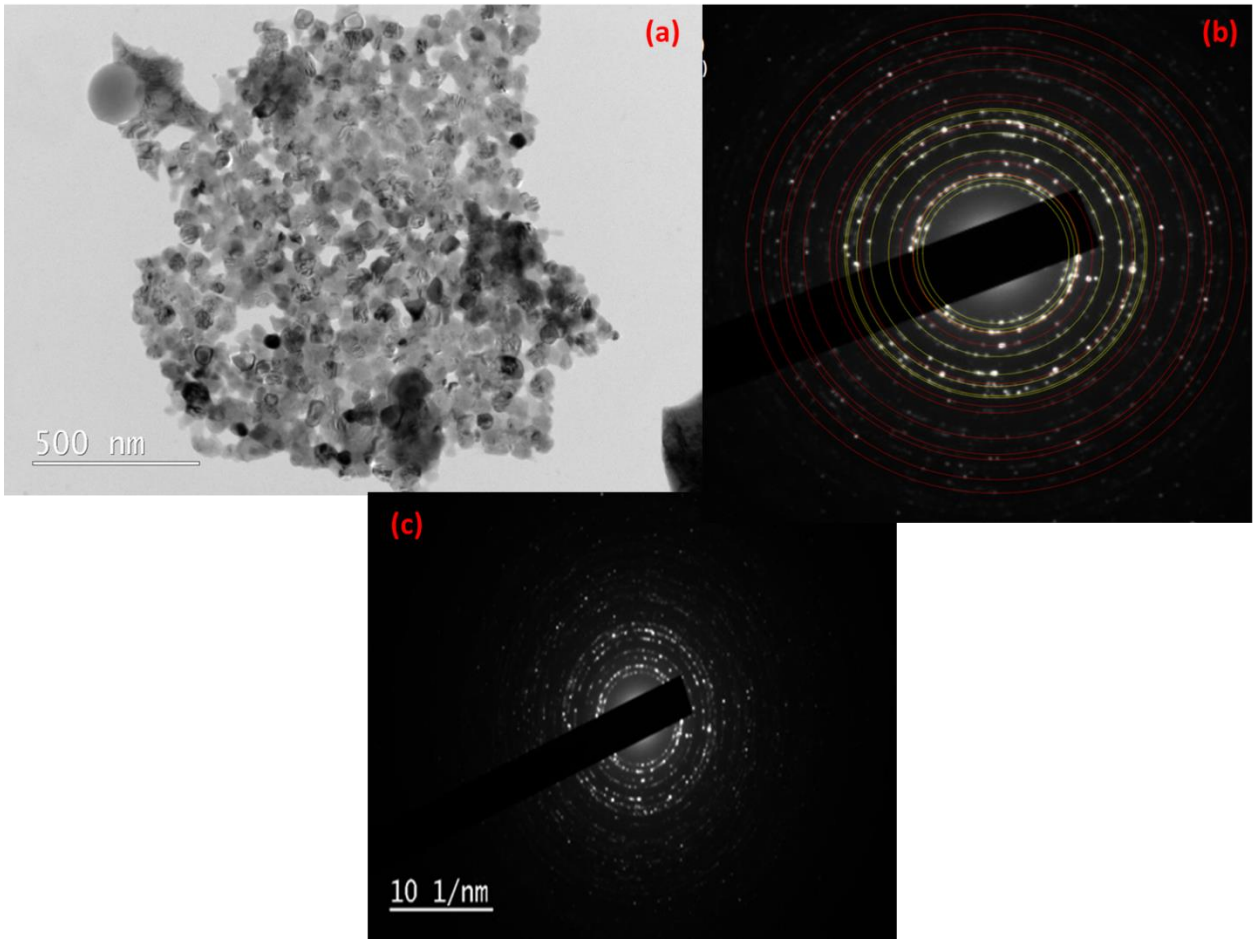

Figure 7.9: Illustration of (a) HR-TEM micrograph and (b) SAED pattern.

7.4. Optical studies

7.4.1. UV-Vis Results:

The diffuse reflectance spectra were measured in the range of 200-800 nm at room temperature and are shown in figure 7.10 (a). The optical bandgap values for the as-prepared Mg doped ZnO and MgO-ZnO composite samples synthesized at 600˚C were determined from reflectance spectra data using the Kubelka-Munk equation:

$$F(R) = (1–R)^2/2R = k/s \quad (7.2)$$

where, R = reflectance; k = absorption coefficient; s = scattering coefficient; It gives a correlation between the reflectance and the concentrations of absorbing species. The Tauc relation:

$$(F(R)\cdot hv)^2 = A\,(hv - E_g) \qquad (7.3)$$

where F(R) is the Kubelka-Munk function, hv is the incident photon energy, A is a constant depending on the transition probability and the diffuse reflectance (R) . The Tauc plot method was used to plot the values of $(F(R)\cdot hv)^2$ vs. hv as illustrated in Figure 7.10 (b). This was done in order to determine the optical band gap values of the samples.

With reference to figure 7.10 (b) and the material $Mg_xZn_{1-x}O$ when the molar concentration is 0.2 the highest reflectance observed was at 35.68%, there is a reflectance peak at 499.92 nm, an absorption peak at 477 nm, a curvature at 402 nm and the absorption edge at 380 nm. When the molar concentration is 0.4 the highest reflectance was observed at 52.21 %, the reflectance peak at 499.92 nm, an absorption peak at 478.73 nm, a curvature at 407.26 nm and an absorption edge at 372.13 nm.

When the molar concentration 0.5 the highest reflectance was observed at 66.28%, an absorption peak at 579.76 nm, a reflectance peak at 499.92 nm, a curvature at 388.63 nm and an absorption edge at 330.49 nm. When the molar concentration is 0.6 the highest reflectance was observed at 59.66%, an absorption peak at 522.49 nm, a reflectance peak at 502.65 nm, a curvature at 380.76 nm and an absorption edge at 327 nm. When the molar concentration is 0.7 the highest reflectance was observed at 54.51 %, an absorption peak at 494.62 nm, a curvature at 383.33 nm, an absorption edge at 314.43 nm and a reflectance peak at 237.67 nm. With respect to the above discussed reflectance and absorption peaks observed in the diffuse reflectance spectra, these can be attributed to defect levels that lie within the bandgap of the materials.

By increasing the concentration of Mg-content in the samples, the absorption edge of ZnO clearly shifts to the blue region, which results in the band gap widening. For molar concentration 0.2 to 0.7, the absorption edge shifts from 380 nm to 314.43 nm and hence the bandgap increases from 3.09 to 3.57 eV. The MgO-ZnO composite sample has an optical bandgap of 3.32 eV. The bandgaps of ZnO and MgO are 3.37 eV and 7.7 eV respectively and can be tuned and hence increased by doping of Mg^{2+}.

A systematic blue shift is observed as Mg^{2+} doping increases which in turn increased the optical bandgap of the samples as observed in figure 7.10 (b) and also presented in table 7.1. One of the possible explanations of this blue shift is an increase of the bandgap which may be expected since MgO has a much larger bandgap than ZnO or the Burstein-Moss effect where the Fermi level of n type ZnO is inside the conduction band. Consequently with Mg doping the conduction bands are filled. This in turn shifts the absorption edge to the higher energy [29].

The substitution of Zn^{2+} by Mg^{2+} results in an increase in oxygen vacancies and electron concentration due to the electronegativity and ionic radius difference between Zn and Mg ions. This increase in carrier density results in the lifting of the Fermi-level into the conduction band

of the degenerate semiconductor and a consequent band gap widening. The band gap widening due to the Moss−Burstein effect was also observed for other semiconductors such as Al-doped ZnO, Sn-doped In_2O_3, an Cd-doped In_2O_4 [26].

Table 7.1: Calculation of bandgap for the $Mg_xZn_{1-x}O$ samples

Composition	**Bandgap (eV)**
$Mg_{0.2}Zn_{0.8}O$	3.09 eV
$Mg_{0.4}Zn_{0.6}O$	3.21 eV
$Mg_{0.5}Zn_{0.5}O$	3.51 eV
$Mg_{0.6}Zn_{0.4}O$	3.57 eV
$Mg_{0.7}Zn_{0.3}$	3.65 eV
MgO-ZnO	3.32 eV

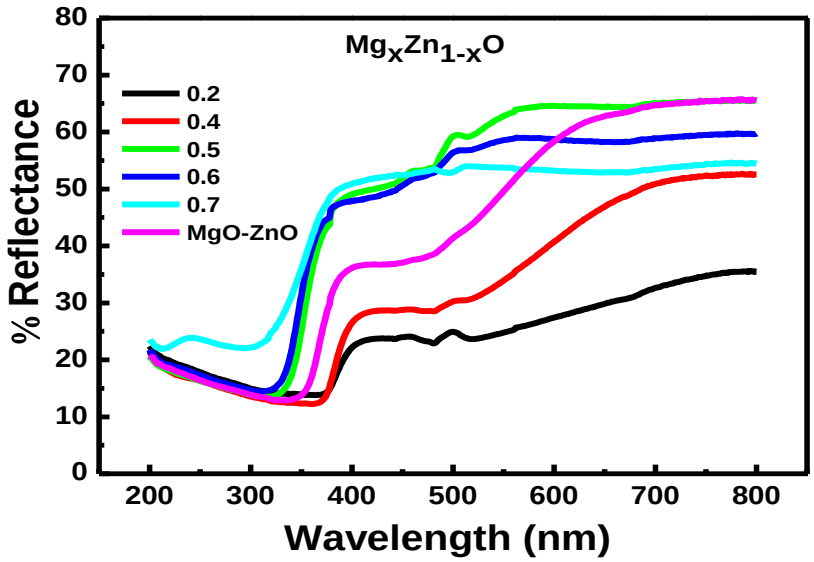

Figure 7.10 (a): UV-Vis reflectance spectra for the Mg doped ZnO samples synthesized at 600˚C.

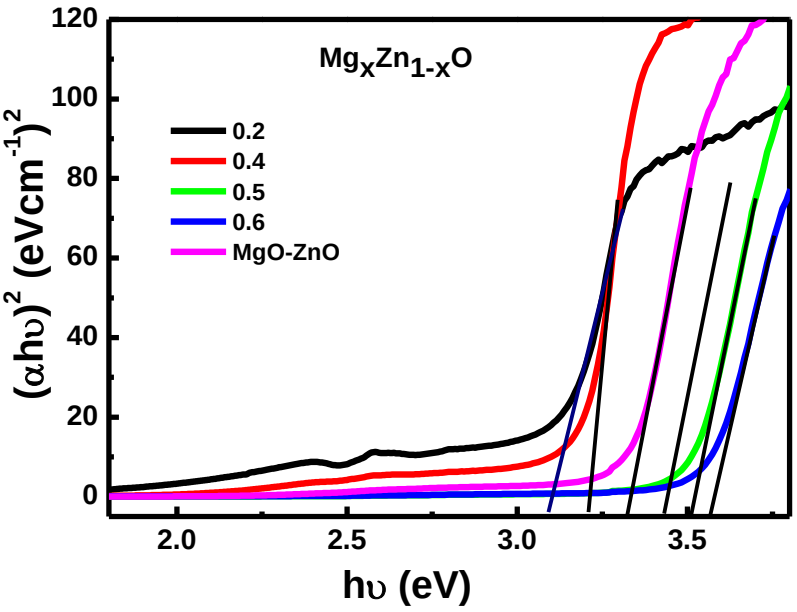

Figure 7.10 (b): Tauc plots used to determine the bandgap values for the Mg doped ZnO samples.

7.4.2. Photoluminescence Results:

Figure 7.11 (a) shows the photoluminescence spectra of the material $Mg_xZn_{1-x}O$ with the molar ratios ranging from 0.2, 0.4, 0.5, 0.6 and 0.7. When the molar concentrations are 0.2 to 0.4 and there is a red shift in emission peaks from 602 to 610 nm and the luminescence intensity decreases. When the molar concentration is 0.5, there is a blue shift in the emission peak and a drastic luminescence quenching from 610 to 551 nm. For molar concentration 0.5 to 0.6 there is a blue shift in the emission peaks from 551 to 539 nm and luminescence enhancement but on the contrary, when the molar concentration is 0.7 there is slight red shift in the emission peak from 539 to 549 nm and a luminescence enhancement.

Figure 7.11 (b) shows the photoluminescence spectra of MgZnO and the composite of MgO-ZnO. With respect to the MgZnO sample there is a UV emission peak at 412 nm and a broad visible emission at 567 nm. Meanwhile with the MgO-ZnO composite sample, the luminescence intensity increases significantly and there is only one broad emission peak at 559 nm in the visible region. This broad light emission peak originates from an inhomogeneous distribution of the various types defects of ZnO, such as interstitial zinc ions, zinc vacancies, oxygen vacancies, oxygen interstitials, substituted magnesium ions and interstitial magnesium ions. The red emission in ZnO particles was assigned to zinc interstitials [26-27].

The deep-level emission (DLE) peak of ZnO NPs has been ascribed to various types of impurities and structural defects such as zinc interstitials (Zn_i), zinc vacancies (V_{Zn}), oxygen interstitials (O_i), antisite oxygen (O_{Zn}), zinc antisite (Zn_O) and donor-acceptor pair (DAP).

Trunk et al. [32] suggested that the green emission peak of $Mg_xZn_{1-x}O$ thin films was ascribed to the free-to-bound type transitions between Zn_i/V_{Zn}, respectively. Talaat et al. [31] reported that the green emission peak of Mg-doped ZnO hollow spheres were attributed to the transition between the oxygen vacancies or the antisite oxygen and donor-acceptor pair. Li et al. [30] suggested that the visible emission peak at 520 nm for $Mg_xZn_{1-x}O$ thin films was assigned to the oxygen vacancies or impurity.

Therefore it can be deduced in this work, the green emission peak is attributed to the oxygen vacancies or donor-acceptor pair generated by Mg substituted of Zn sites, and the red shift of green emission peak is probably related to the Mg-related defect levels.

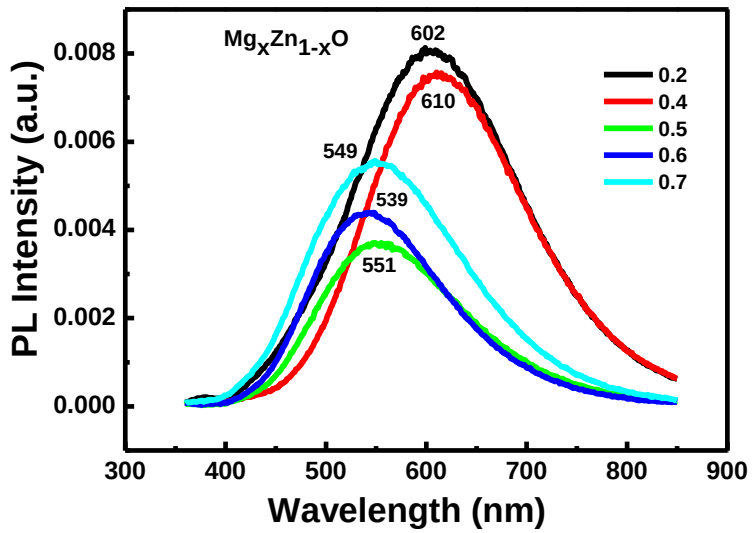

Figure 7.11(a): Photoluminescence spectra of Mg doped ZnO nanophosphor samples synthesized via solution combustion method.

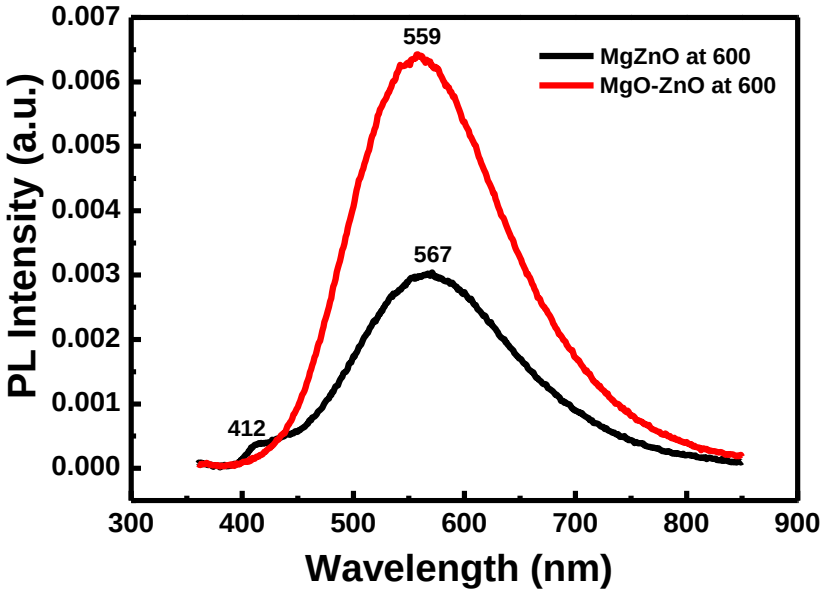

Figure 7.11(b): Photoluminescence spectra of composite MgO-ZnO and MgZnO nanophosphors synthesized via solution combustion method.

7.5 Conclusion

The XRD patterns reveal the presence of two well-defined crystalline phases, which are MgO and ZnO. The most prominent phase being ZnO since Mg was incorporated into the ZnO matrix. Therefore, the alloy illustrated in figure 7.2 was the ideal case of synthesis but that alloy was not obtained in this study but rather a combination of two crystalline materials ZnO and MgO.

FTIR spectra of samples $Mg_{0.2}Zn_{0.8}O$, MgZnO and composite MgO-ZnO show the Zn-O peaks for Mg doped ZnO samples such as $Mg_{0.2}Zn_{0.8}O$ which appeared at 566 cm^{-1} at higher wavenumbers in contrast to pure ZnO at 466 cm^{-1}. This is due to the incorporation of Mg^{2+} into the ZnO crystal structure, which was confirmed by the XRD results.

There is a definite correlation between the XRD, FTIR and SAED results, which is that the alloy illustrated in figure 7.2 does not in fact form but rather a mixed phase material.

In conclusion an incorporation and increase in concentration of the Mg^{+2} ion in the zinc matrix yields an increase in optical bandgap which is attributed to the Moss-Burstein effect or the generation of more oxygen vacancies and electrons. Therefore, it can be deduced in this work, the green luminescence emission peak is attributed to the oxygen vacancies or donor-acceptor pair generated by Mg substituted of Zn sites, and the red shift of green emission peak is probably related to the Mg-related defect levels.

References:

[1] Zieliński, P. A., Schulz, R., Kaliaguine, S. and Van Neste, A., "Structural transformations of alumina by high energy ball milling", J. Mater. Res.8 (11) 2985-2992 (1993).

[2] Travitzky, N., Kumar, P., Sandhage, K. H., Janssen, R. and Claussen, N., "Rapid synthesis of Al2O3 reinforced Fe-Cr-Ni composites", Mater. Sci. Eng. A, 344 (1-2) 245-252 (2003).

[3] Martínez E., Flores N., Negrete, J. and Torres V., G., "Structure and properties of Zn-Al-Cu alloy reinforced with alumina particles', Mater. Des. 24 (3) 281-286 (2003).

[4] Fierro J. L. G. , Metal Oxides: Chemistry & Applications. CRC Press, (2006).

[5] Kanade K.G., Kale B.B.,Aiyer R. C. and Das B,K., "Effect of solvents on the synthesis of nano-size zinc oxide and its properties', Materials Research Bulletin 41 590-600 (2006).

[6] Ganguly A., Trinh Ph., Ramanujachary K.V., Ahmad T. and Mugweru A.,"Reverse micellar based synthesis of ultrafine MgO nanoparticles (8–10 nm): Characterization and catalytic properties", Journal of colloid and interface science. 353: 137-142 (2011).

[7] Klingshirn C, Phys. Status Solidi B 71 (1975) 547.

[8] Djurisic A.B., Leung Y.H., Small 2 (2006) 945.

[9] Weissenrieder K.S., J. Muller J., Thin Solid Films 300 (1997) 30.

[10] Zhang J., Pan F., Hao W., Wang T., Mater. Sci. Eng. B 129 (2006) 93.

[11] Lin F.C., Takao Y., Shimizu Y., Egashira M., Sens. Actuators B 25 (1995) 843.

[12] Jana S., Vuk A.S., Mallick A., Orel B., Biswas P.K., Mater. Res. Bull. 46 (2011) 2392.

[13] Bhattacharya P., Das R.R., Katiyar R.S., Thin Solid Films 447–448 (2004) 564.

[14] Fujihara S., Ogawa Y., Kasai A., Chem. Mater. 16 (2004) 2965.

[15] Chen N.B., Sui C.H., Mater. Sci. Eng. B 126 (2006) 16.

[16] Li G., Lan S., Li L., Li M., Bao W., Zou H., Xu X., Gan S., J. Alloys Comp. 513 (2012) 145.

[17] Sun J., Zhang X, Xia Z., Du H., J. Appl. Phys. 111 (2012) 013101.

[18] Bandi V.R., Grandhe B.K., Woo H-J., Jang K, Shin D-S, Yi S-S., Jeong J-H., J. Alloys Comp. 538 (2012) 85.

[19] Zhu G., Wang Y., Ci Z., Liu B., Shi Y., Xin S., J. Lumin. 132 (2012) 531.

[20] Arshad M, Ansari M.M., Ahmed A.S., Tripathi P, Ashraf S.S.Z., Naqvi A.H., Azam A, Journal of Luminescence, 161(2015) 275-280.

[21] Lu Y-F., Ni H.Q., Mai Z-H. and Ren Z.M., J. Appl. Phys., 2000, 88, 498.

[22] Lin C.C., Chen H.P., Liao H.C. and Chen S.Y., Appl. Phys. Lett., 2005, 86, 183103.

[23] Valtiner M., Borodin S. and Grundmeier G, Phys. Chem.Chem. Phys., 2007, 9, 2406.

[24] Singh V.P., Rath C, RSC Advances, 2015, 5, 44390-44397.
[25] Huang H., Shih W., Lai C., Applied Physics Letters, 2010, 193505, 96.
[26] Etacheri V., Roshan R, Kumar V., ACS Applied Materials and Interfaces,2012,4, 2717-2725.
[27] Liu X., Wu X., Cao H., Chang R.P.H., J. Appl. Phys. 95 (2004) 3141.
[28] Gomi M., Oohira N., Ozaki K., Koyano M., Jpn. J. Appl. Phys. 42 (2003) 481.
[29] Hsu H-C.,Wu C-Y,Cheng H-M.,andW.-F.Hsieh,"Bandgap engineering and stimulated emission of ZnMgO nanowires," AppliedPhysicsLetters,vol.89,ArticleID013101,2006.
[30] Li H., Zhang Y., Pan X., Wang T., and Xie E., J. Alloy. Compd. 472, 208 (2009).
[31] Hammad T.M. and Salem J.K., J. Nanopart. Res. 13, 2205 (2010).
[32] Trunk M., Venkatachalapathy V., Galeckas A., and Kuznetsov A.Y., Appl. Phys. Lett. 97, 211901 (2010).

Chapter 8: The impact of different molar concentrations of Sr in Sr doped ZnO samples on the structure, morphology and luminescent properties.

8.1 Introduction:

Inorganic luminescent materials have practical applications in many devices such as light emitting diodes (LEDs), cathode ray tubes, flat panel screens and field emission displays that involve the artificial production of light [1,2]. Recently, considerable efforts have been devoted to research on new materials to be used for LEDs and optical storage.

Further, the interest in luminescent materials showing reversible photo-induced spectral changes at room temperature has grown significantly because the combination of such phenomena with near-field optical microscopy is very promising when applied to high density optical storage with nanometer resolution [4]. Kubota et al. [5] reported a new luminescent material, $SrZnO_2$:Ba^{2+}, Mn^{2+}, which suggested that $SrZnO_2$ could be a promising candidate to act as a luminescent host lattice. Schnering and Hoppe reported the crystal structure of $SrZnO_2$ [6]. In $SrZnO_2$ the ZnO_4 tetrahedral share edges with each other and form waved layers. The Sr atoms are located in the cavities between the layers. Eu^{3+}-doped fluorescence have been investigated extensively in various compounds because of their importance for applications in lighting and display phosphors [7–11], and also due to a basic interest in probing the local structure around the dopant [12–14].

Crystal structure of $SrZnO_2$ was reported as early as in 1960 [15]. There were not many luminescence studies made until recently. Kubota et al. [16] reported luminescence of Mn^{2+}.

In the following years, luminescence of various activators Pb^{2+} [17], Ce^{3+} [18], Pr^{3+} [19], Sm^{3+} [20,21], Tb^{3+} [22,23], Eu^{3+} [24–26], etc. in this host was studied. Use of these phosphors in applications like solid state lighting was also suggested [20]. Most of the investigators used the conventional solid state reaction route, but some novel methods like sol–gel [19] and gel-combustion [20] have been used recently.

The crystal structure of $SrZnO_2$ was reported by Schnering and Hoppe [27]. $SrZnO_2$ belongs to the orthorhombic system with the space group Pnma. In $SrZnO_2$, the ZnO_4 tetrahedrons share edges with each other and form waved layer. The Sr atoms are surrounded by seven oxygen atoms and are located at the cavity between the layers. To this structure, there is one site for the Sr atom, one for the Zn atom, and two for the O atoms [28].

This chapter reports on the preparation, structure, morphology, reflectance hence absorption behaviour, bandgap and photoluminescence properties of the Sr doped ZnO samples and SrO-ZnO composite samples. These samples were synthesised at 600˚C, 700°C and annealed at 1000°C. This was done to obtain high purity and crystalline phases of these samples which was not previously obtained from this work. The synthesis method used was solution combustion synthesis and urea as a fuel.

8.2 Experimental

8.2.1 Preparation of Sr doped ZnO and SrO-ZnO composite samples

Strontium nitrate, zinc nitrate and urea were used as starting materials. The materials were mixed stiochiometrically according to the following chemical reaction equation:

$$3Sr(NO_3)_2 + 3Zn(NO_3)_2(H_2O)_6 + 11CH_4N_2O \rightarrow 3SrZnO_2 + 40H_2O + 11CO_2\uparrow + 17N_2\uparrow \quad (8.1)$$

The masses of the samples were calculated according to the following ratio $Sr_xZn_{1-x}O$, x having the following values 0.2, 0.4, 0.5, 0.6, 0.7, 0.8 and 1. In a typical preparation for x = 0.5 3.0 g of urea, 2.2291 g of zinc hexahydrate nitrate and 1.5856 g of strontium nitrate and 10 mL of deionized water were added, and stirred for 60 minutes at approximately 80˚C to achieve a homogenous solution. The solution was then transferred to a furnace which was pre-set to a synthesis temperature of 600˚C ± 15, for 15 minutes. A white powder was formed after the reaction was complete. A typical flame in combustion synthesis technique was not observed. Depicted in figure 8.1 is the schematic representation of the synthesis procedure.

Additionally to the above mentioned synthesized samples, SrO-ZnO composite samples were synthesized at 600˚C and 700˚C. The SrO-ZnO composite samples synthesized at 600 and 700˚C and were annealed at 1000˚C. This was done to obtain high purity and crystalline phases of these samples which was not previously obtained from the previous chapters.

8.2.2 Characterization

The structural properties of the powder samples were analysed using a Bruker D8 Advance powder diffractometer with a Cu-Kα radiation wavelength of 1.54 Å. The elemental composition and electronic states were analysed using X-ray photoelectron spectroscopy (XPS) using a PHI 5000 Versa probe equipped with monochromatic Al-K radiation (hv = 1253.6 eV). For higher resolution spectra, the hemispherical analyzer pass energy was maintained at 11.3 eV. Measurements were performed using a 1 eV/step (or 45 min acquisition times) binding energies for survey scans from 0 to 1400 eV and 1 eV/step and 20–30 min times for the high-resolution scans. A low energy electron beam was used to achieve charge neutrality on the sample surface. All the absolute binding energies of the photoelectron spectra were corrected with C 1s signal at 284.6 eV.

Particle morphology and elemental composition of the materials were analysed using Jeol JSM-7800F field emission scanning electron microscope (FE-SEM) coupled with Oxford Aztec 350 X-Max80 energy-dispersive X-ray spectroscopy (EDS). The particle sizes and shapes of the samples were also examined using JEOL ARM200F transmission electron microscope. The diffuse reflectance data was recorded using ultraviolet visible (UV–vis) spectrometer by a Perkin Elmer Lambda 950 UV–Vis. The photoluminescence data was recorded at room temperature using a He-Cd laser at an excitation wavelength of 325 nm.

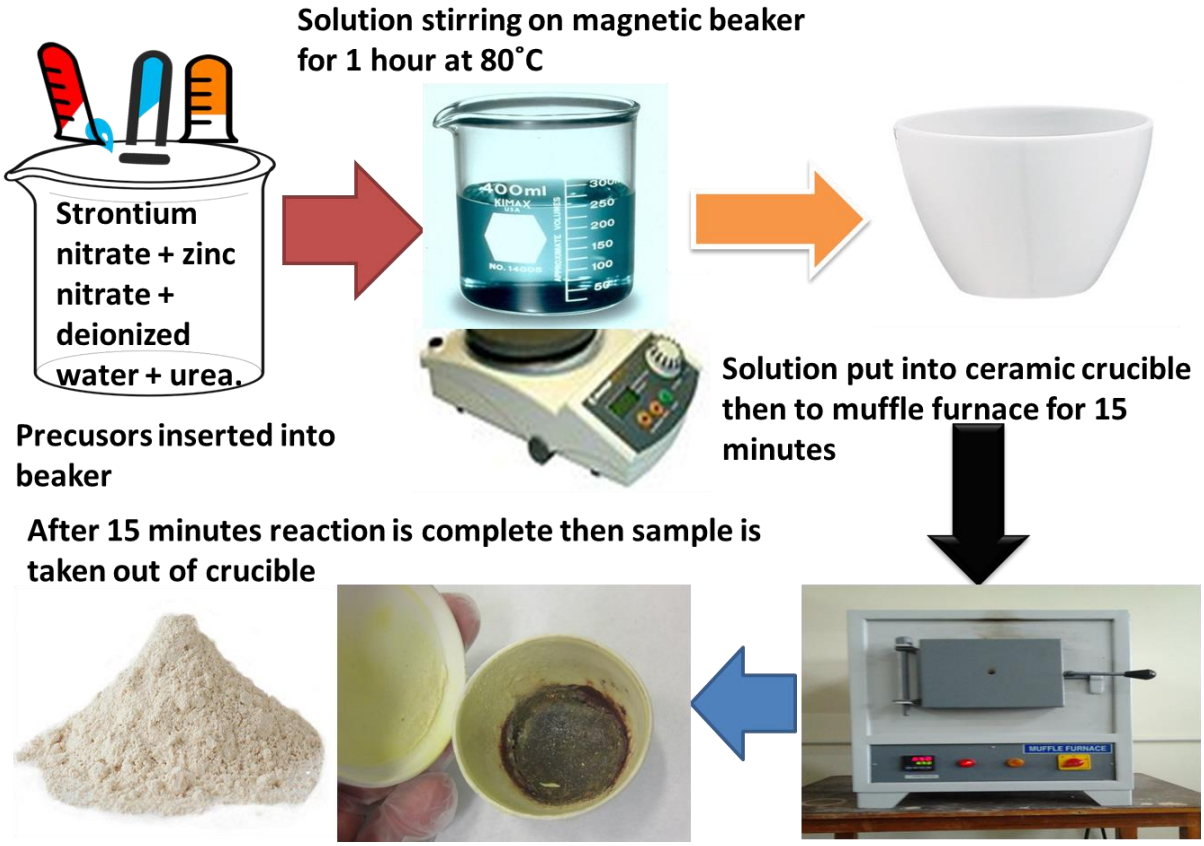

Figure 8.1: Graphical representation for preparation of the Sr doped ZnO and SrO-ZnO composite samples using solution combustion synthesis method.

8.3 Results and Discussion

8.3.1. Structural Studies

8.3.1.1. XRD Results

Figure 8.2 (a) – (c) illustrate the XRD patterns of the $Sr_xZn_{1-x}O$ samples where x = 0.2, 0.6 and 0.8. The samples were synthesized by solution combustion method at a synthesis temperature of 600˚C. These XRD spectra do not match that of SrO this was an already established fact from chapter 6, the most prominent phase in the materials being ZnO.

Figure 8.2 (d) and figure 8.2 (e) are the patterns of the Sr doped ZnO, SrO-ZnO composite samples synthesized at 600˚C and SrO-ZnO composite samples synthesized at 600˚C and 700˚C. The SrO-ZnO composite samples synthesized at 600 and 700˚C and were annealed at 1000˚C. The effect of annealing was done to alter the following conditions phase change, crystallite growth in a preferred direction. This was observed in the decrease of intensity of the XRD peaks from the as-prepared samples up to the samples which were synthesized at 700˚C and annealed at 1000˚C sample.

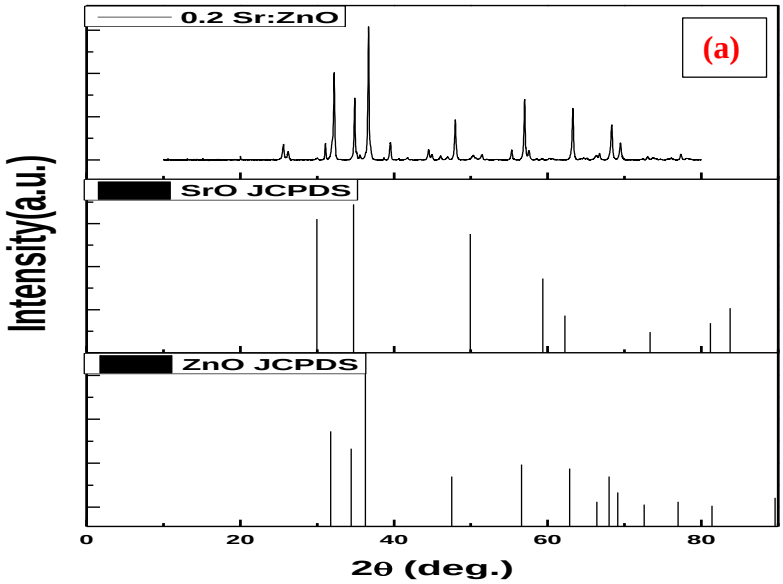

Figure 8.2 (a): XRD patterns of the Sr doped ZnO sample $Sr_{0.2}Zn_{0.8}O$ synthesized at 600˚C using solution combustion method.

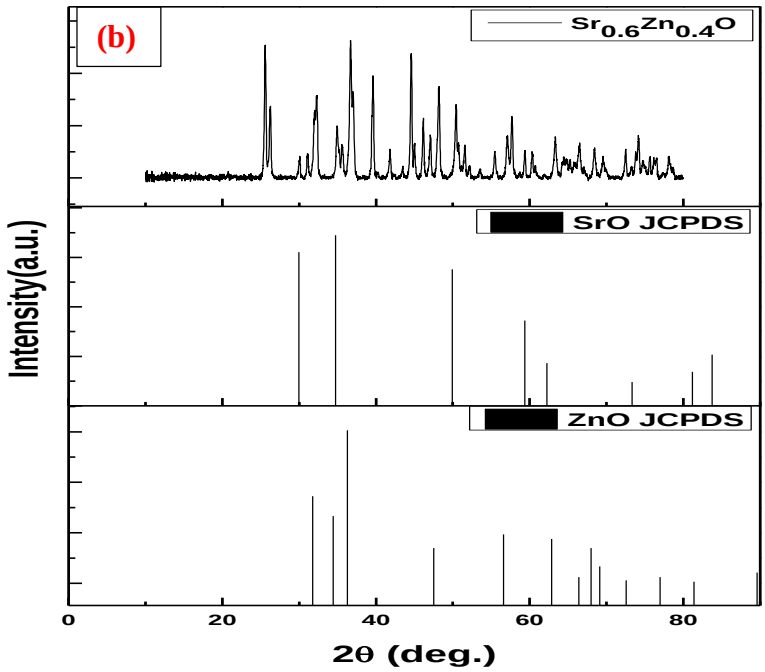

Figure 8.2 (b): XRD pattern of the Sr doped ZnO sample $Sr_{0.6}Zn_{0.4}O$ synthesized at 600˚C using solution combustion method.

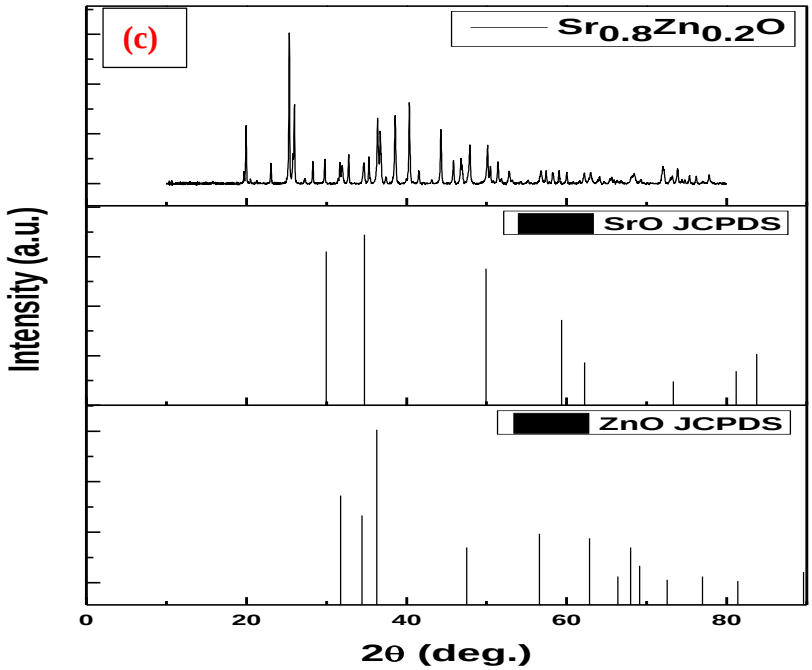

Figure 8.2 (c): XRD pattern of the Sr doped ZnO sample $Sr_{0.8}Zn_{0.2}O$ synthesized at 600˚C using solution combustion method.

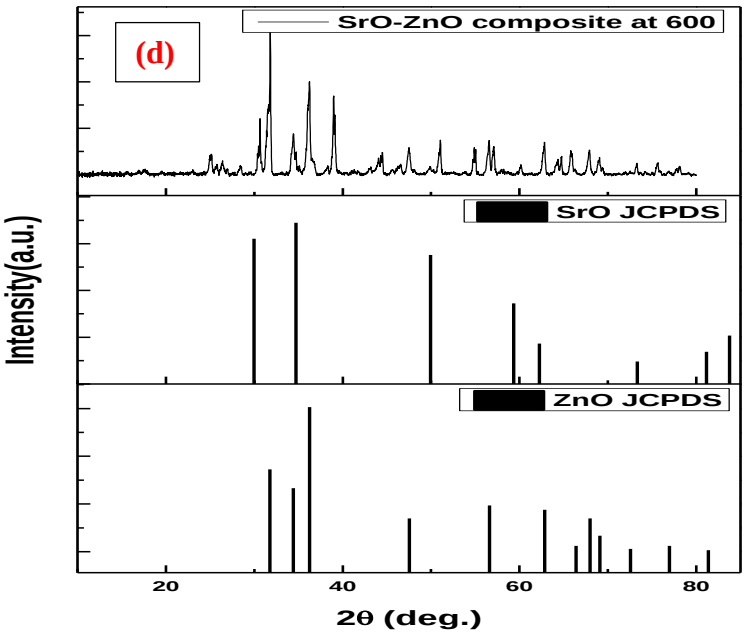

Figure 8.2 (d): XRD pattern of the SrO-ZnO composite sample synthesized at 600˚C using solution combustion method.

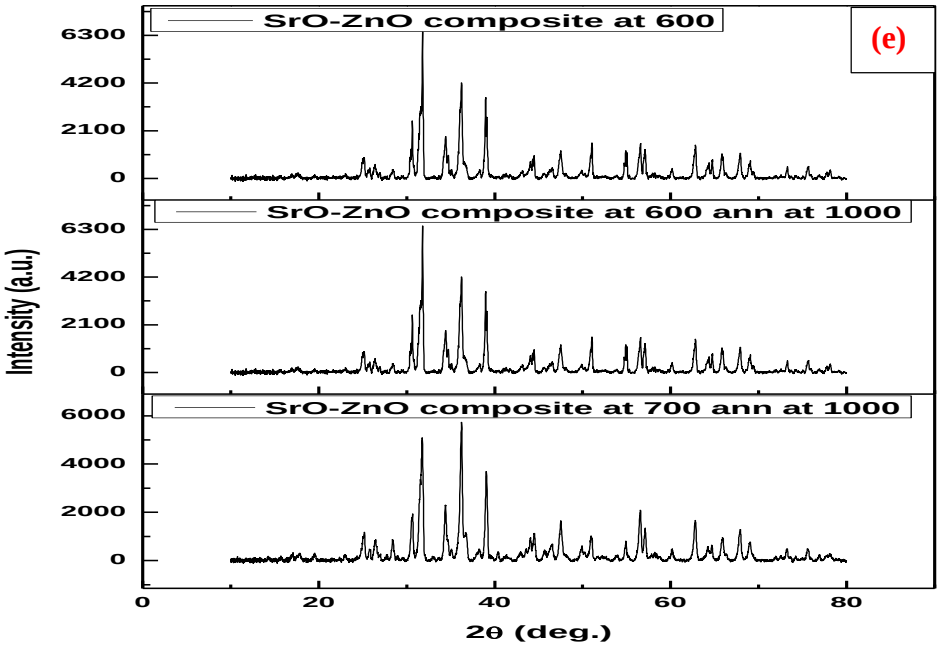

Figure 8.2 (e): XRD patterns comparing the SrO-ZnO composite, SrO-ZnO composite synthesized at 600˚C annealed at 1000˚C and SrO-ZnO composite synthesized at 700˚C annealed at 1000˚C crystalline structures and phases.

8.3.1.2. SEM and EDS Results

The SEM micrographs at different magnifications are depicted in figure 8.3 (a,b,d,e,g,h,j,k,l). In figure 8.3 (a & b) it is clear that $Sr_{0.2}Zn_{0.8}O$ consists of small and coagulated particles of irregular shapes and different sizes forming flower-like structures. With respect to figure 8.3 (d & e) the surface morphology of $Sr_{0.5}Zn_{0.5}O$ results in large oval-shaped structures. In figure 8.3 (g & h), the surface morphology of $Sr_{0.8}Zn_{0.2}O$ sample displays elongated rod like structures with spherical flakes on top of the rods. Figure 8.3 (j, k and l) are the SEM images of SrO-ZnO composite synthesized at 600˚C, the particle morphology results in particles that are shaped as agglomerated structures of cubes, pyramids and cylinders.

The EDS spectra of the above discussed samples are shown in figure 8.4 (c,f, i and m). The carbon shown in the EDS spectra is attributed to the carbon tape on which the samples were mounted. Figure 8.4 (c) is the spectra of the $Sr_{0.2}Zn_{0.8}O$ sample, the weight percentages for zinc, oxygen and strontium are 75.6%, 19.6% and 4.8% respectively. Figure 8.4 (f) is the EDS spectrum of the $Sr_{0.5}Zn_{0.5}O$ sample the weight percentages for zinc, oxygen and strontium are 67.6%, 18.1% and 14.3% respectively. Figure 8.4 (i) is the spectrum of the $Sr_{0.8}Zn_{0.2}O$ sample and the weight percentages of strontium, oxygen and zinc are 67.6%, 18.1% and 14.3% respectively. Figure 8.4 (m) is the spectrum of the SrO-ZnO sample and the weight percentages of zinc, oxygen and strontium are 77.9%, 17.1% and 5.1% respectively.

The morphology on the SEM results yielded interesting results. The small deposits of Sr nanostructures incorporated on the big ZnO crystals at various dopant concentrations, which were diffused at higher concentrations. As previously observed from the SEM results namely figure 4.5(c) and (d), figure 6.6 (c) and (d) and now figure 8.3 (b), when comparing SEM images of the same magnifications. Initially the nanostructures for ZnO appeared small, the SrO nanostructures appeared much larger so in SEM images of the Sr doped ZnO nanostructures the particles appear smaller than anticipated because as the doping concentration of Sr increases the structures become smaller.

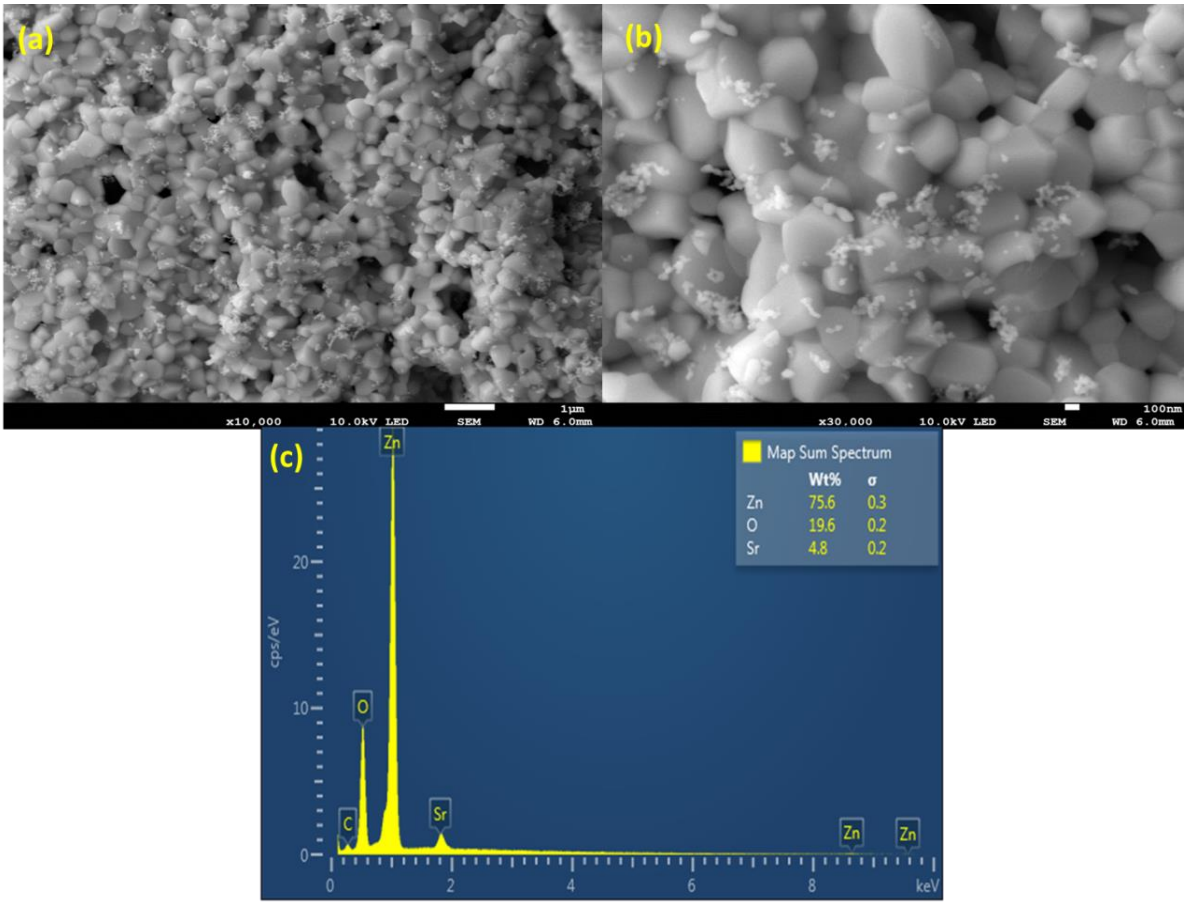

Figure 8.3 (a-c): The SEM images and EDS spectra of the Sr doped ZnO sample $Sr_{0.2}Zn_{0.8}O$ synthesized at 600˚C by solution combustion method.

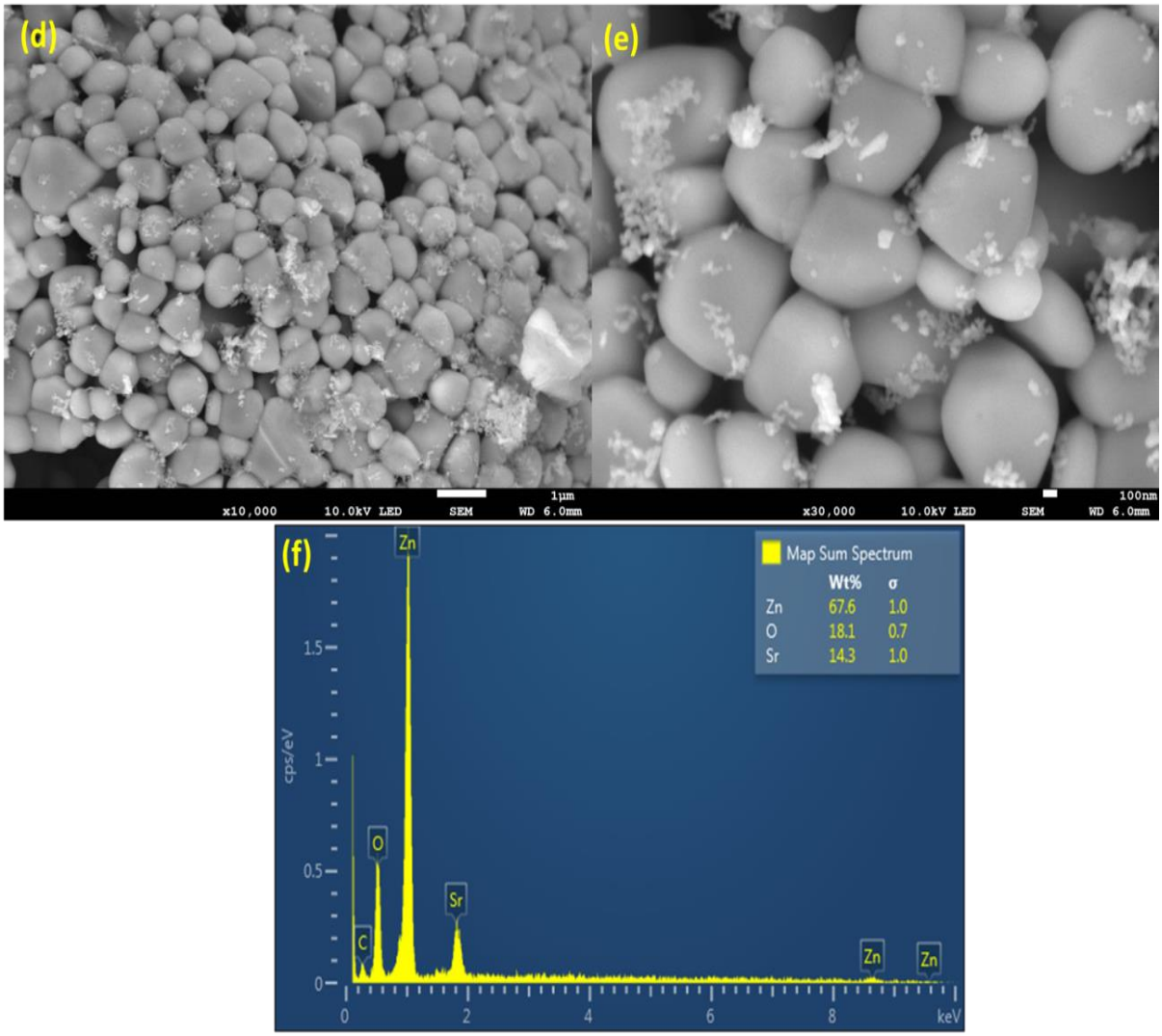

Figure 8.3 (d-f): The SEM images and EDS spectra of the Sr doped ZnO sample $Sr_{0.5}Zn_{0.5}O$ synthesized at 600˚C by solution combustion method.

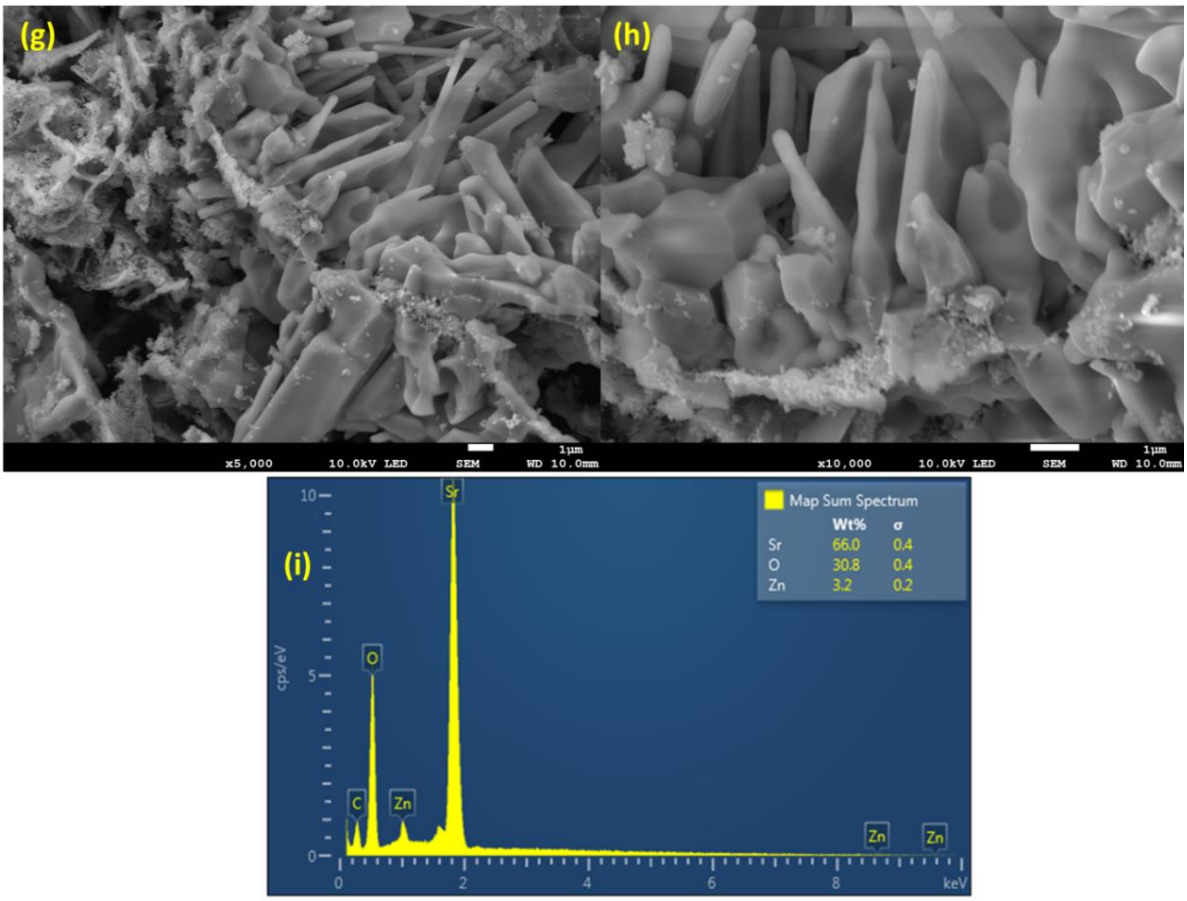

Figure 8.3 (g-i): The SEM images and EDS spectra of the Sr doped ZnO sample $Sr_{0.8}Zn_{0.2}O$ synthesized at 600˚C by solution combustion method. .

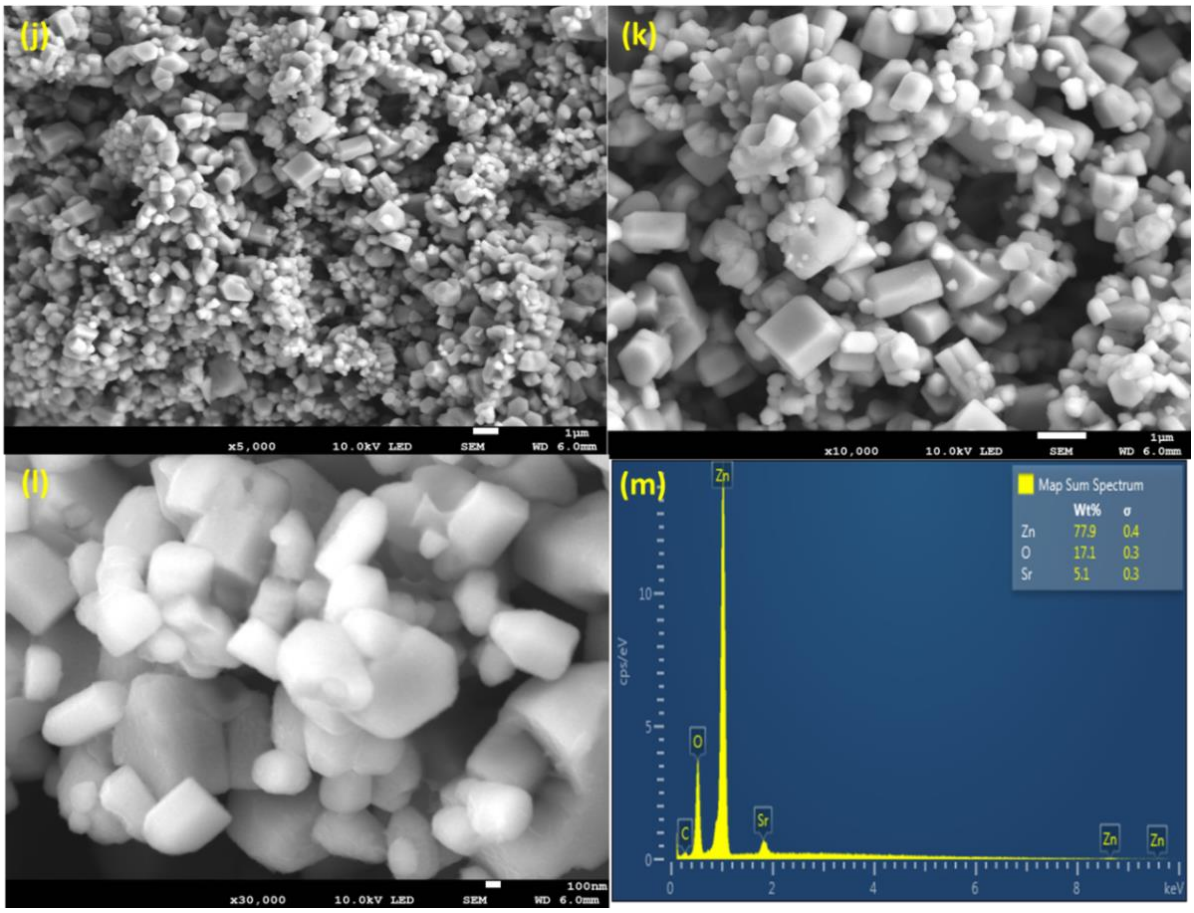

Figure 8.3 (j-m): The SEM images and EDS of the SrO-ZnO composite sample synthesized at 600˚C by solution combustion method.

8.4. Optical studies

8.4.1 UV-Vis Results

The diffuse reflectance spectra were measured in the range of 250-800 nm at room temperature and are shown in Figure 8.5 (a). The optical bandgap values for the Sr doped ZnO and SrO-ZnO composite samples synthesized at 600˚C and 700˚C were determined from the reflectance spectra using the Kubelka-Munk equation:

$$F(R) = (1–R)^2/2R = k/s \quad (8.2)$$

where, R = reflectance; k = absorption coefficient; s = scattering coefficient; It gives a correlation between the reflectance and the concentrations of absorbing species. The Tauc relation:

$$(F(R)\cdot hv)^2 = A\,(hv - Eg) \quad (8.3)$$

where F(R) is the Kubelka-Munk function, (hv) is the incident photon energy, A is a constant depending on the transition probability and the diffuse reflectance (R) . The Tauc plot method

was used to plot the values of $(F(R)\cdot hv)^2$ vs. (hv) as illustrated in Figure 8.5 (b). This was done in order to determine the optical band gap values of all of the above mentioned samples.

With regards to the diffuse reflectance spectra the following system $Sr_xZn_{1-x}O$ when the molar concentration is 0.2 the highest observed reflectance was at 58%, there's an absorption peak at 520 nm, reflectance peaks at 479 and 500 nm and an absorption edge at 378 nm.

When the molar concentration is 0.4, the highest reflectance observed was at 55% and the absorption edge was at 378 nm. When the molar concentration is 0.5 the highest reflectance observed was at 68% and the absorption edge was at 378 nm. When the molar concentration is 0.6 the highest reflectance observed was at 29%, there's an absorption peak at 500 nm, reflectance peaks at 459 and 479 nm and an absorption edge at 378 nm. When the molar concentration is 0.7 the highest reflectance observed was at 37%, there's an absorption peak at 500 nm, reflectance peak at 459 and 479 nm and an absorption edge at 378 nm. When the molar concentration is 0.8 the highest reflectance observed was at 62%, there's an absorption peak at 500 nm, reflectance peak at 459 and 479 nm and an absorption edge at 378 nm. The reflectance and absorption peaks are attributed to the defects levels within the bandgap of the samples.

The optical bandgaps of these samples were calculated from the absorption edges. The theoretical bandgaps of SrO and ZnO are 5.71 and 3.37 eV respectively. The bandgap values of the Sr doped ZnO samples from molar concentrations 0.2, 0.4, 0.5, 0.6, 0.7 to 0.8 are as follows 3.17, 3.17, 3.22, 3.12, 3.15 and 3.17 eV. As the doping concentration of Sr increases, the bandgap fluctuates around the average value of 3.17 eV.

There is a significant difference between the theoretical and experimental bandgap values, the difference in bandgap can be attributed to the fact that these samples were synthesized via solution combustion method and hence there is a possible introduction of more defects especially oxygen vacancies in this synthesis method. This fact will be explored further in the photoluminescence discussion when elaborating on the optical transitions of these samples.

Figure 8.5 (c) is the diffuse reflectance spectra of the SrO-ZnO composite synthesized at 600˚C, the same SrO-ZnO composite annealed at 1000˚C and the SrO-ZnO synthesized at 700˚C and annealed at 1000˚C. Figure 8.5 (d) is the Tauc plot of the bandgap determination graphs of the above mentioned samples.

With regards to the diffuse reflectance spectra the highest reflectance observed for the SrO-ZnO composite synthesized at 600°C was at 88%, there's a reflectance peak at 482 nm, a curvature at 428 nm and an absorption edge at 380 nm. The SrO-ZnO composite synthesized at 600˚C annealed at 1000˚C sample has the highest observed reflectance at 67%, there are reflectance peaks at 461 and 500 nm, absorption peak at 482 nm and an absorption edge at 380 nm. For the SrO-ZnO composite synthesized at 700˚C annealed at 1000˚C sample the highest observed reflectance was at 68% and the absorption edge was at 380 nm.

The optical bandgap of these samples was calculated from the absorption edges. The optical bandgap of the SrO-ZnO composite synthesized at 600˚C, the same composite synthesized at 600˚C annealed at 1000˚C and SrO-ZnO composite synthesized at 700˚C annealed at 1000˚C

are as follows 3.20, 3.18 and 3.20 eV. These bandgap values are significantly smaller than the theoretical values of both SrO and ZnO. The difference in bandgap can be attributed to the fact that this sample was synthesized via solution combustion method and hence there is a possible introduction of more defects more especially oxygen vacancies in this synthesis method.

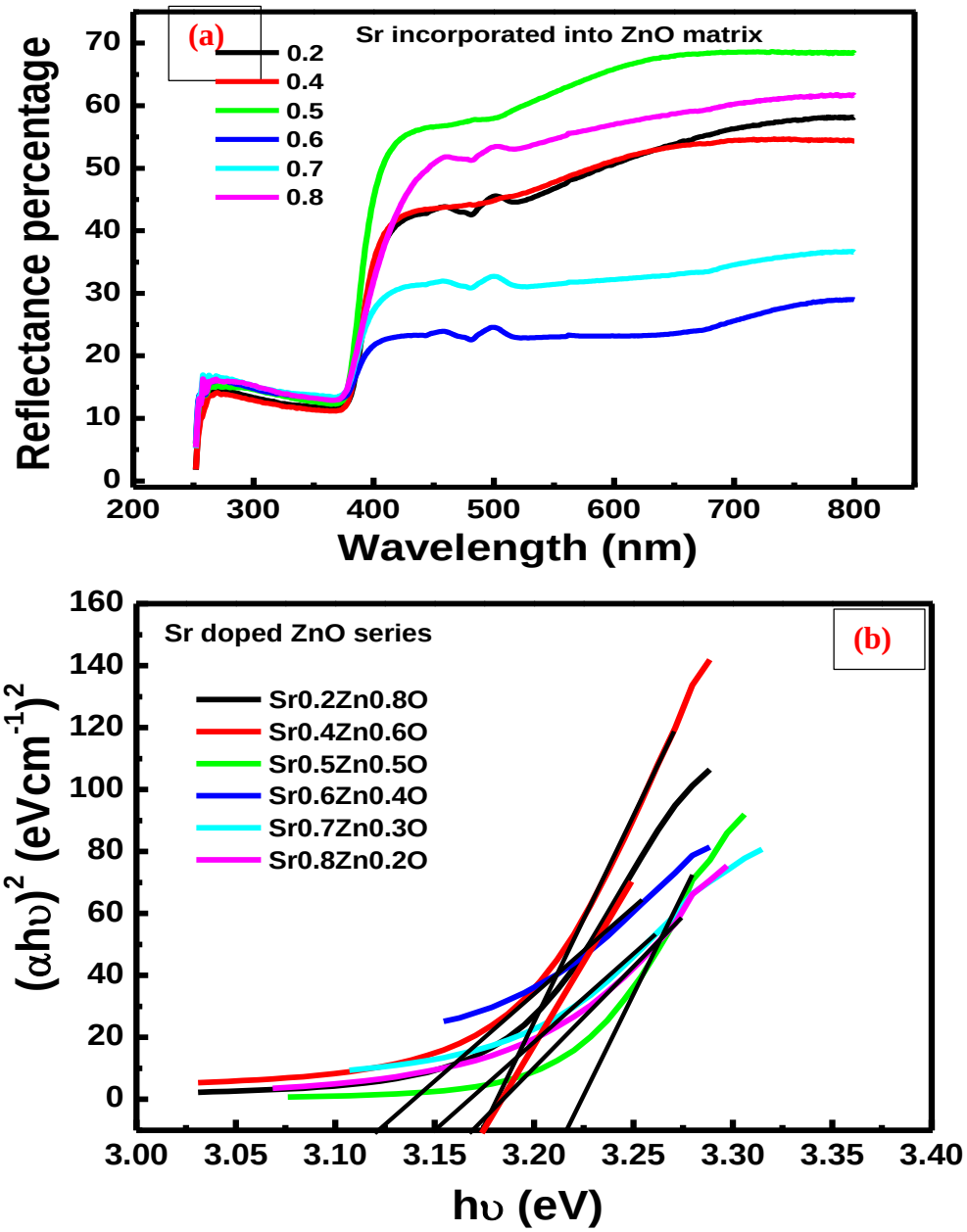

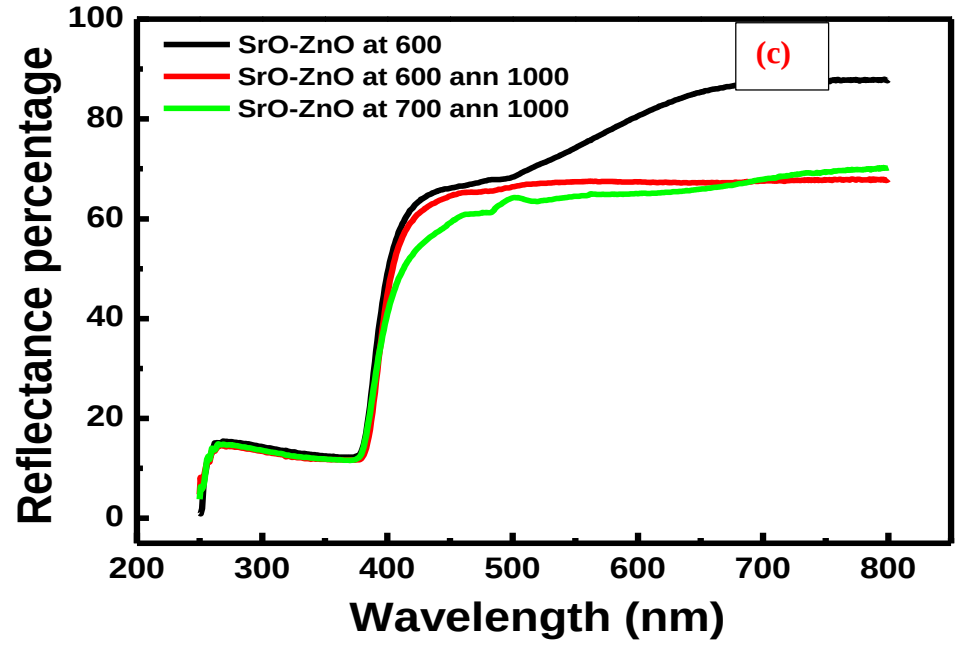

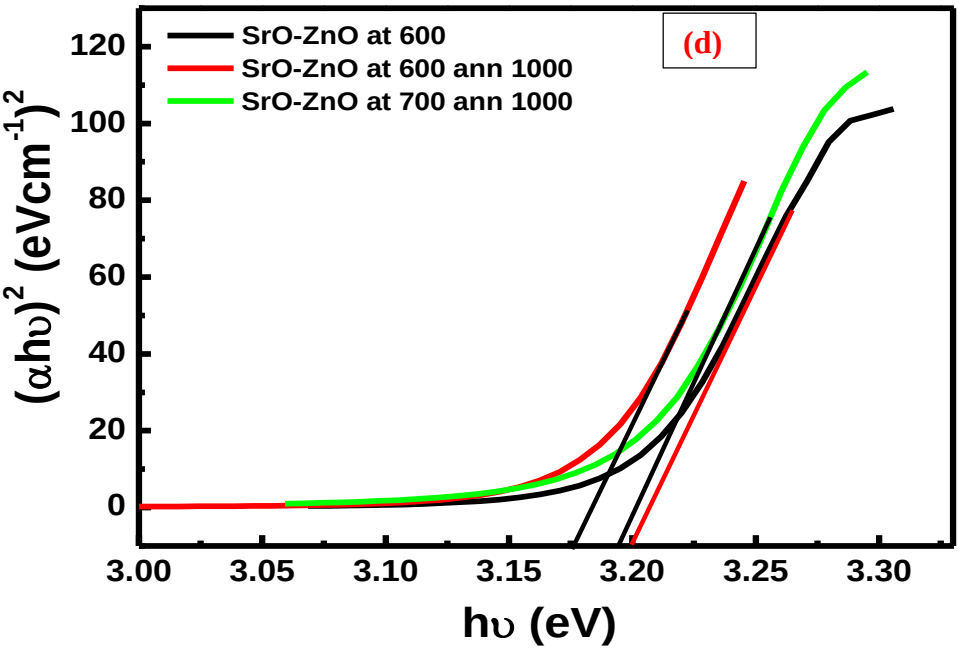

Figure 8.4 (a-d): Diffuse reflectance spectra and Tauc plots for bandgap determination purposes.

8.4.2. Photoluminescence Results

Figure 8.5 (a) are the photoluminescence spectra of the Sr doped ZnO samples that are synthesized at 600˚C. The excitation used was from the He-Cd laser with a wavelength of 325 nm. When the molar concentration is 0.2 and 0.4 there are emission peaks at 383, 540 and 760 nm. For molar concentration 0.5 there are emission peaks at 383, 514 and 760 nm. When the molar concentration is 0.6 there are emission peaks at 383 nm, minor humps at 413, 435 and 760 nm and a broad peak at 514 nm. When the molar concentration is 0.7 there are emission peaks at 383, 514 and 760 nm and when the molar concentration is 0.8 there are emission peaks at 383, 514 and 760 nm. The emission peak in the UV region is narrow and can be associated with recombination of free excitons, while the broad emission peaks at 514 and 540 nm can be attributed to defect levels in the bandgap.

There is an increase in intensity in the emission peaks in the visible region with increasing molar concentration of Sr. As the molar concentration of Sr is increasing within the ZnO matrix, there is an introduction of defects possibly oxygen vacancies leading to an enhanced green emission. The more defects (oxygen vacancies) are introduced, the emission peaks become more intense up to molar concentration 0.5, which is the most luminescent sample. Then a drastic quench in luminescence was observed from molar concentration 0.6, 0.7 and 0.8. This occurred because the saturation point was reached between the strontium and zinc ions in the ZnO matrix.

Figure 8.5 (b) is the PL spectra of the SrO-ZnO composite samples synthesized at 600˚C and 700˚C. With regards to both of the SrO-ZnO composite samples there are emission peaks in the UV region, visible and infrared region. For the SrO-ZnO sample synthesized at 600˚C there is a narrow UV peak at 385, a broad visible peak at 611 nm and a minor hump in the infrared region at 760 nm. For the SrO-ZnO sample synthesized at 700˚C there is a narrow UV peak at 383 nm, a broad visible peak at 583 nm and a minor hump at 760 nm. There is a shift in the visible region peak from 611 to 583 nm as the synthesis temperature was increased. The PL peak intensity of the SrO-ZnO synthesized at 700˚C is more intense than that of the sample prepared at 600^{o}C. As the synthesis temperature was increased from 600°C to 700°C a few phenomena arose. There was an increase in peak intensity in the UV region and visible region. This was previously observed with regards to the increase in peak intensity in the UV region with the ZnO sample synthesized at 700°C. Also in this chapter it was discovered that there is a luminescence maximum point where molar concentration 0.5 meaning when equal amounts of strontium and zinc are added in the synthesis mixture they yield a high luminescence in the green region.

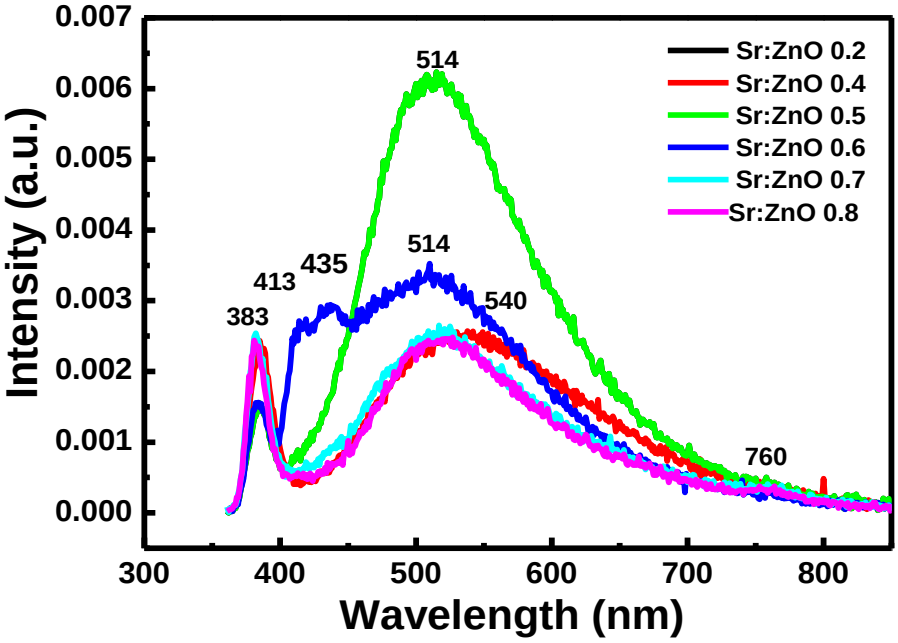

Figure 8.5 (a) Photoluminescence spectra of the Sr doped ZnO samples synthesized at 600˚C by solution combustion synthesis.

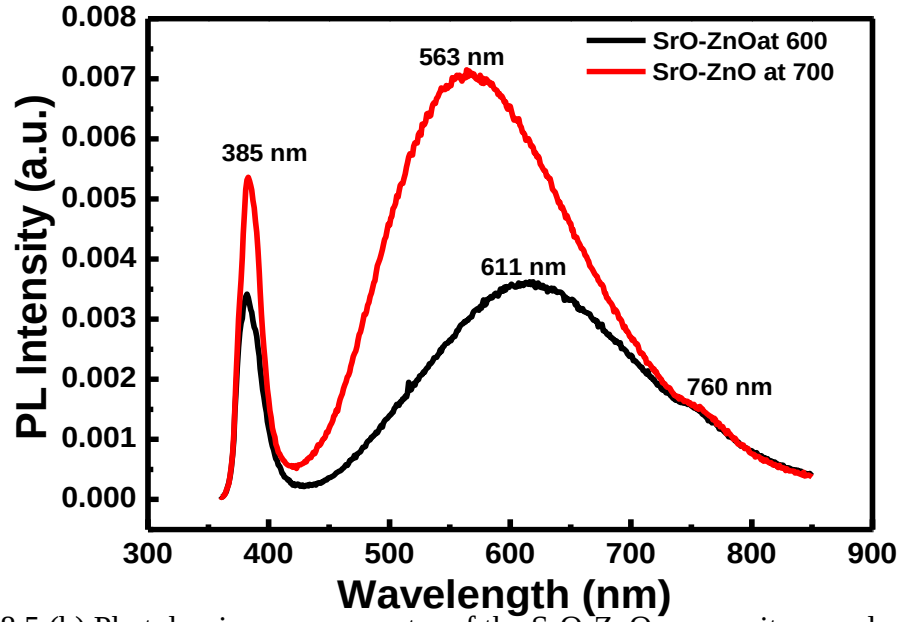

Figure 8.5 (b) Photoluminescence spectra of the SrO-ZnO composite samples at different synthesis temperatures.

8.5 Conclusion

In conclusion the XRD spectra do not match that of SrO. This was an already established from chapter 6. The most prominent phase in the materials is ZnO. The SEM studies yielded different kinds of particle morphologies when the molar ratio was varied, such as flower-like structures, oval-shaped particles and elongated rod-like structures.

With regards to the optical studies, diffuse reflectance spectra were recorded and from the absorption edges Tauc plots were obtained in order to calculate the optical bandgaps for the series of samples and their composites. The bandgap values of the Sr doped ZnO from molar concentrations 0.2, 0.4, 0.5, 0.6, 0.7 and 0.8 were as follows 3.17, 3.17, 3.22, 3.12, 3.15 and 3.17 eV. As the doping concentration of Sr increases the bandgap fluctuates around the average value of 3.17 eV.

The bandgap of the SrO-ZnO composite synthesized at 600˚C, the same composite annealed at 1000˚C and the SrO-ZnO composite synthesized at 700˚C and annealed at 1000˚C were 3.20, 3.18 and 3.20 eV respectively. These values were comparable to the optical bandgap values of the Sr doped ZnO series. The PL results of the Sr doped ZnO series and the SrO-ZnO composite samples yielded emission peaks in the UV, visible and infrared regions due to the many defects that lie within the bandgap of these samples.

References:

[1] Jüstel T., Nikol H., Ronda C., Angew. Chem. Int. Ed. 37 (1998) 3084.

[2] Blasse G, Grabmaier B.C., Luminescent Materials, Springer-Verlag, Berlin, 1994.

[3] Müller C.D., Falcou A., Reckefuss N., Rojahn M., Wiederhirn V., P. Rudati P., Frohne H., Nuyken O., Becker H., Meerholz K., Nature 421 (2003) 829.

[4] Betzig E., Trautman J.K., Science 257 (1992) 189.

[5] Kubota S., Oyama T., Yamane H., Shimada M., Chem. Mater. 15 (2003) 3403–3405.

[6] Schnering V.H.G, Hoppe R.Z., Allg. Chem. 141 (1960) 87–98.

[7] Yang S.J., Yuan L.J., Sun J.T., Rare Met. 22 (2003) 95.

[8] Jagannathan R, J. Lumin. 68 (1996) 211–216.

[9] Kharsika V.F., Komissarova L.N.,Kirichenko A.N., Murav'ev E.N., Orlovskii V.P., Chernyaev A.P., Inorg. Mater. 37 (2001) 963–967.

[10] Honma T., Toda K., Ye Z.N., Sato M., J. Phys. Chem. Solids 59 (1998) 1187–1193.

[11] Kodaira C.A., Brito H.F., Malta O.L., Serra O.A., J. Lumin. 101 (2003) 11–21.

[12] Zych E., Karbowiak M., Domagala K., Hubert S., J. Alloys Compd. 341 (2002) 381–384.

[13] Pires A.M., Davolos M.R., Stucchi E.B., Int. J. Inorg. Mater. 3 (2001) 785–790.

[14] Yang Z., Lin J.H., Su M.Z., You L.P. , Mater. Res. Bull. 35 (2000) 2173–2182.

[15] von Schnering H.G. , Hoppe R., Die Naturwissenschaften 47 (1960) 467.

[16] Kubota S., Oyama T., Yamane H., Shimada M., Chem.Mater.15 (2003) 3403.

[17] Manavbasi A., La Combe J.C. , J. Lumin.128 (2008) 129.

[18] Manavbasi A., La Combe J.C., Mater., Res.Soc.Symp. Proc.916 (2006) 41.

[19] He X.H. ,Zhou J., Bi C.L., Li W.H. , Rengong J. X., J.Synthetic Cryst.36 (2007) 1408.

[20] Yang L. , Yu X., Yang S., Zhou C., Zhou P, Gao W., Ye P.,Mater.Lett. 62 (2008) 907.

[21] He X. , Xiyou Jinshu ,CailiaoYu , Gongcheng /Rare Metal Mater.Eng.36 (2007) 1574.

[22] Yu, Xu X. ,Zhou P. ,Peng X. ,Yang S. ,Mater.Lett.59 (2005) 1178.

[23] Khatkar S.P. ,Taxak V.B. , Kumar D. ,Han H.D. , Han C.H. ,Sharma G.,J. Korean Phys. Soc.48(2006)1355.

[24] Wang Y, Gao H., J.Solid State Chem.179 (2006) 1870.

[25] Yu X., .Xu x., Zhou C., Tang J., Peng X., Yang S., Mater.Res.Bull. 41 (2006)1578.

[26] He X.H., Zhou J., Li W.H., .Zhou Q.F., Chin.J. Inorg. Chem. 22 (2006) 1706.

[27] Schnering V.H.G., Hoppe R.Z., Anorg. Allg. Chem. Einzeldarst. 141 (1960) 87.

[28] Kubota S., Oyama T., Yamane H., Shimada H., Chem. Mater. Commun. 15 (2003) 3403.

Chapter 9: Summary and conclusion

This chapter presents the summary and conclusion, and possible future work that can be done to improve the properties of the metal oxide phosphors.

ZnO phosphors were successfully synthesized via solution combustion synthesis method and their crystallization was confirmed by XRD analysis. The ZnO powder crystallized in the hexagonal phase. The diffraction patterns became sharper and more intense with increasing synthesis temperature from 600˚C to 700˚C indicating improvement of crystallinity and an increase in crystallite sizes from 23.338 nm to 30.0575 nm of the as-prepared ZnO phosphor powder. The average size of the synthesized ZnO nanoparticles obtained from the Scherrer's formula is 23.338 nm and from HR-TEM micrographs is 28.846 nm. The XRD and HR-TEM particle are in good correlation with each other.

With respect to the photoluminescence results, the ZnO nanoparticles exhibited two characteristic peaks one narrow in the UV region at 380 nm which was ascribed to recombination of free excitons, and one broad in the visible region at 639 for ZnO synthesized at 600˚C and 626 nm for ZnO synthesized at 700˚C, which were attributed to electron mediated defect levels in the bandgap.

The MgO phosphors were successfully synthesized via solution combustion synthesis method and it's crystal structure was confirmed by XRD analysis. The MgO powder was found to have cubic crystal structure with Fm-3m space group and crystallized in a rocksalt/sodium chloride (NaCl) type cubic structure. The average calculated crystallite size from the XRD data was 23.296 nm and the average particle size from the HR-TEM micrograph was 57.452 nm. The bandgap of this sample was calculated from the absorption edge at 222 nm and it was 5.22 eV. The theoretical bandgap of MgO is 7.7 eV. This MgO sample has three shoulder PL emission

peaks at approximately 419, 432 and 465 nm and a minute emission peak in the visible region at 663 nm. MgO usually would not exhibit PL in the visible light region. However, it has been found that charge transfer on the surface states could also result in UV-visible luminescence. In conclusion the MgO sample didn't exhibit ultraviolet to visible PL emission just visible PL emission hence charge transfer didn't occur efficiently onto the surface states.

The crystalline structure of the SrO product synthesized by solution combustion synthesis at 600˚C was analysed by XRD. The XRD pattern indicated the presence of three well-defined crystalline phases which are SrO, $Sr(OH)_2$ and $Sr(CO_3)_2$. The most prominent phase was $Sr(OH)_2$. SEM data showed that the SrO powder consisted of small and coagulated particles of irregular shapes and different sizes. Pores of different sizes were observed and were attributed to solution combustion synthesis. This was the result of the outgassing of the gaseous products of this synthesis method, namely N_2 and CO_2.. The bandgap of this sample was calculated from the absorption edge at 356 nm and it was 3.32 eV. The theoretical bandgap of SrO is 5.71 eV. The PL spectrum exhibited ultra violet and deep level emission peaks. There was a narrow peak in the UV region at 397 nm and a broad peak in the visible region at 750 nm. Figure 6.9 (b) are the deconvoluted peaks of the UV region emission peak at 397 nm, the deconvoluted peaks were at 379, 404 and 438 nm. These deconvoluted emission peaks were attributed to electron mediated defect levels in the bandgap.

With respect to the Mg-doped ZnO and MgO-ZnO composite study, the XRD patterns reveal the presence of two well-defined crystalline phases of MgO and ZnO. The most prominent phase being ZnO since Mg was incorporated into the ZnO matrix. FTIR spectra of samples $Mg_{0.2}Zn_{0.8}O$, MgZnO and composite MgO-ZnO showed the Zn-O peaks for Mg doped ZnO samples such as (MgZnO and $Mg_{0.2}Zn_{0.8}O$) which appeared at 566 cm^{-1} at higher wavenumbers in contrast to pure ZnO at 466 cm^{-1}. This is due to the incorporation of Mg^{+2} into the ZnO crystal structure, which was confirmed by the XRD results. In conclusion an incorporation and increase in concentration of the Mg^{+2} ion in the zinc matrix yielded an increase in optical bandgap which was attributed to the Moss-Burstein effect, and was explained by generation of more oxygen vacancies and electrons.

These XRD spectra do not match that of SrO this was an already established fact from chapter 6, the most prominent phase in the materials being ZnO. The optical bandgap of these samples were calculated from the absorption edges. The bandgap values of the Sr doped ZnO for x= 0.2, 0.4, 0.5, 0.6, 0.7 and 0.8 were 3.17, 3.17, 3.22, 3.12, 3.15 and 3.17 eV respectively. As the doping concentration of Sr increases the bandgap fluctuates around the average value of 3.17 eV.

The bandgap of the SrO-ZnO composite synthesized at 600˚C, the same composite synthesized at 600˚C annealed at 1000˚C and SrO-ZnO composite synthesized at 700˚C annealed at 1000˚C were 3.20, 3.18 and 3.20 eV respectively. These values are comparable to the Sr doped ZnO series optical bandgap values. Lastly with regards to the PL results the Sr doped ZnO series and the SrO-ZnO composite samples yielded emission peaks in the UV, visible and infrared regions due to the many defects that lie within the bandgap of these samples, which is a very interesting end result.

In conclusion, it is widely accepted that the surface area and lattice defects play important roles in photocatalytic activities of metal oxide semiconductors. Researchers also found that doping is an effective and facile method to improve the photocatalytic properties because the variation of the surface area and incorporation of dopant ions are able to generate lattice defects and variation of band gap energy. With regard to the photocatalytic activity the incidental impurities (dopant ions) molecules need to be adsorbed on to the photocatalytic surface for the redox reactions to occur. The higher the effective surface area, the higher will be the adsorption of target molecules leading to better photocatalytic activity. Photocatalytic activity of ZnO depends on various factors such as phase purity, surface area, crystallite size, nature of dopants, and method of preparation. These factors which were investigated in this study and it was deduced that solution combustion method favours the fabrication of highly crystalline and pure nanophosphors with high surface area without dopants and it also varied the bandgap energy of the pure ZnO, MgO and SrO samples with their composites, which was attributed to the production of oxygen and hence oxygen vacancies in the material.

Future work

Further research will be done is to test the phosphors developed in this study in photocatalytic behaviour. They may also have applications in solar cells. More focus will be on the development of ZnO as it will be used as a main host incorporated with other metal oxides and rare earth metals as dopants for the solar cell devices. The overriding objective will be to improve the luminescent intensity and chemical stability of the phosphors in order to prolong the life span and the general performance of the solar cell devices.